

# **Understanding the Dynamics of Vapor Intrusion Processes**

By

Jonathan Gustaf Viking Ström

A Dissertation Submitted in Partial Fulfillment of the Requirements for the Degree

of

Doctor of Philosophy in the School of Engineering at Brown University

Providence, Rhode Island

May 2020

© Copyright 2020 by Jonathan G. V. Ström

This dissertation by Jonathan G. V. Ström is accepted in its present form by the School of Engineering as satisfying the dissertation requirement for the degree of Doctor of Philosophy

Date \_\_\_\_\_

Eric M. Suuberg, Advisor

Recommended to the Graduate Council

Date \_\_\_\_\_

C. Franklin Goldsmith, Reader

Date \_\_\_\_\_

Brenda M. Rubenstein, Reader

Approved by the Graduate Council

Date \_\_\_\_\_

Andrew G. Campbell, Dean of the Graduate School

## Curriculum Vitae

### Education

- Brown University, PhD in Chemical and Biochemical Engineering (2020)
- Brown University, Master of Science in Chemical and Biochemical Engineering (2019)
- Royal Institute of Technology (KTH), Bachelor of Science in Chemical Engineering (2015)

### Teaching

- Water Supply and Wastewater Treatment (2017-2019)
- Fuels, Energy, Power, and the Environment (2016-2019)
- Reaction Kinetics and Reactor Design (2018)

### Publications

Jonathan G. V. Ström, Yuanming Guo, Yijun Yao, and Eric M. Suuberg.

"Factors Affecting Temporal Variations in Vapor Intrusion-Induced Indoor Air Contaminant Concentrations."

Building and Environment 161 (August 15, 2019): 106196.

Genfu Wang, Shuaishuai Ma, Jonathan G. V. Ström, Eric Suuberg, Yijun Yao, and Lingzao Zeng.

"Investigating Two-Dimensional Soil Gas Transport of Trichloroethylene in Vapor Intrusion Scenarios Involving Surface Pavements Using a Pilot-Scale Tank."

Journal of Hazardous Materials 371 (June 5, 2019): 138–45.

Yijun Yao, Yuting Xiao, Jian Luo, Genfu Wang, Jonathan G. V. Ström, and Eric M. Suuberg.

"High-Frequency Fluctuations of Indoor Pressure: A Potential Driving Force for Vapor Intrusion in Urban Areas."

Science of The Total Environment 710 (March 25, 2020): 136309.

Yijun Yao, Jianping Zuo, Jian Luo, Qiang Chen, Jonathan G. V. Ström, and Eric M. Suuberg.

"An Examination of the Building Pressure Cycling Technique as a Tool in Vapor Intrusion Investigations with Analytical Simulations."

Journal of Hazardous Materials 389 (May 5, 2020): 121915.

Papers in progress:

Jonathan G. V. Ström, Shuai Xie, and Eric M. Suuberg

"Sorption Phenomena In Transient Vapor Intrusion Scenarios"

Building & Environment

## Acknowledgements

My time at Brown has been some of the most rewarding years of my life, both professionally and personally. This thesis presents the culmination of my work here, but the lessons I have learnt go beyond this. I am deeply thankful for being given this opportunity, and I have many people to thank for making this time so special.

First, I would like to thank my advisor Professor Eric Suuberg. He was the first to interest me in vapor intrusion research, and without his support I would not have been able to pursue this research at such a fine institution. Throughout my years at Brown, Eric has always been available to guide and mentor me, and his encouragement has been instrumental for my development. It has been a privilege to have worked with him.

Secondly, I would like to thank the other two committee members - Professors Brenda Rubenstein and Franklin Goldsmith. I have greatly benefited from their commitment to teaching excellence and I have thoroughly enjoyed attending their classes. I am deeply grateful for their service on this committee.

I also want to offer my thanks to the many professors I have met at Brown and whose classes I have attended - it truly has been a wonderful experience. I would especially like to thank Indrek Külaots and Andrew Peterson for giving me the opportunity to assist them in teaching their classes. Through them I have discovered a passion for teaching that I did not think that I had.

To all of my friends and colleagues at Brown: Thank you for your support and for being in my life. Your companionship has contributed to my enjoyment and well-being in ways I cannot express. I would especially like to thank Zachary Saleeba, Jordan Noble, Aaron North, and Adam Gavarkovs for being such wonderful friends.

Lastly, I would like to thank my parents and my family. Moving and living in another country has not easy, and your tireless support has been instrumental for my success. I am especially thankful that my father, Martin Ström, has been able to visit me so regularly - I have many fond memories of our times together. I love you all with all of my heart.

# Contents

<b>1</b>	<b>Introduction</b>	<b>1</b>
1.1	Indoor Air Quality and Vapor Intrusion . . . . .	1
1.2	Issues In Vapor Intrusion Investigations . . . . .	4
1.3	Innovations In Vapor Intrusion Investigations . . . . .	8
1.3.1	Controlled Pressure Method . . . . .	8
1.3.2	Indicators, Tracers, and Surrogates . . . . .	10
1.4	Issues With Applying CPM and Using ITS . . . . .	10
1.5	Mathematical Modeling of Vapor Intrusion . . . . .	11
1.6	Outline . . . . .	12
<b>2</b>	<b>Numerical Modeling of Vapor Intrusion</b>	<b>15</b>
2.1	Summary . . . . .	15
2.2	Introduction . . . . .	15
2.3	Finite Element Method . . . . .	19
2.4	Geometry Generation . . . . .	22
2.5	Vapor Intrusion Physics and Governing Equations . . . . .	24
2.5.1	The Indoor Environment . . . . .	25
2.5.2	The Importance Of Soil Moisture Content . . . . .	28
2.5.3	Airflow In The Vadose Zone . . . . .	32
2.5.4	Mass Transport In The Vadose Zone . . . . .	34

2.6 Meshing . . . . .	41
2.6.1 Meshing The VI Model . . . . .	43
2.6.2 Boundary Layer Mesh . . . . .	44
2.7 Solver Configuration . . . . .	45
2.7.1 Adaptive Mesh Refinement . . . . .	47
2.8 Post-processing & Results . . . . .	51
2.9 Review of Vapor Intrusion Models . . . . .	54
2.9.1 Analytical Models . . . . .	55
2.9.2 Numerical Modeling . . . . .	57
<b>3 Preferential Pathways: Drivers of Temporal and Spatial Variability in Vapor Intrusion</b>	<b>61</b>
3.1 Summary . . . . .	61
3.2 Introduction . . . . .	62
3.2.1 The ASU House . . . . .	64
3.2.2 EPA Duplex . . . . .	69
3.3 Modeling A Preferential Pathway . . . . .	74
3.3.1 Geometry And Mesh . . . . .	75
3.3.2 Physics And Boundary Conditions . . . . .	76
3.4 Temporal Variability And Preferential Pathways . . . . .	80
3.4.1 Role Of Air Exchange Rate . . . . .	86
3.5 Soil-Gas Spatial Variability And Preferential Pathways . . . . .	90
3.5.1 ASU House . . . . .	90
3.5.2 EPA Duplex . . . . .	93
<b>4 The Significance of Foundation Entry Mechanism on Vapor Intrusion</b>	<b>97</b>
4.1 Summary . . . . .	97
4.2 Advection Entry: Role of Soil and Foundation . . . . .	98

4.3 Applying Transport Classification Concept . . . . .	104
4.3.1 The Controlled Pressure Method . . . . .	104
4.3.2 Indicators, Tracers, And Surrogates . . . . .	107
4.4 Predicting the Extent of Building Pressurization . . . . .	111
4.4.1 Wind Effects . . . . .	112
4.4.2 Temperature Effects . . . . .	114
4.4.3 Air Exchange Rate . . . . .	115
4.4.4 Predicting Pressurization At The EPA Duplex . . . . .	116
<b>5 Sorption Phenomena in Transient Vapor Intrusion Scenarios</b>	<b>121</b>
5.1 Summary . . . . .	121
5.2 Introduction . . . . .	122
5.3 Methods . . . . .	124
5.3.1 Experimental Setup . . . . .	124
5.3.2 Numerical Model . . . . .	125
5.4 Results & Discussion . . . . .	133
5.4.1 Fitting Sorption Parameters . . . . .	133
5.4.2 Soil Sorption's Retarding Effect . . . . .	135
5.4.3 Effects of Indoor Material Sorption . . . . .	139
5.4.4 Indoor Material Sorption And Mitigation . . . . .	143
5.5 Conclusions . . . . .	145
<b>6 Conclusions and Future Work</b>	<b>147</b>
6.1 Summary of Results . . . . .	147
6.2 Suggestions for Future Research . . . . .	151
6.2.1 Advection Transport and Specific Site Characteristics . . . . .	151
6.2.2 Preferential Pathways . . . . .	152
6.2.3 Sorption and Vapor Intrusion . . . . .	152

6.2.4 Modeling and Design of Mitigation Systems . . . . .	152
6.2.5 Model Effects of Weather and Seasons on Vapor Intrusion . . . . .	152
<b>Bibliography</b>	<b>153</b>
<b>A Geometry Generation</b>	<b>165</b>
<b>B Soil Properties</b>	<b>167</b>

# List of Figures

1.1	Overview of vapor intrusion . . . . .	3
1.2	Overview of the controlled pressure method concept . . . . .	9
2.1	The considered VI scenario. . . . .	17
2.2	Coupling between the physics used to model VI. . . . .	18
2.3	Basis functions are used to approximate the FEM solution to a PDE. . . . .	21
2.4	Birds-eye view of the VI scenario, showing the foundation and the breach, building wall, as well as the plane of symmetry that allows only a quarter of the total domain to be generated. . . . .	23
2.5	VI model geometry in COMSOL . . . . .	24
2.6	Schematic of soil-gas contaminant entry into a building through a breach in the foundation. . . . .	26
2.7	van Genuchten soil moisture retention curve and relative permeability . . .	31
2.8	Effective diffusivity of TCE in the vadose zone. . . . .	40
2.9	Some common mesh elements. Figure from COMSOL[40]. . . . .	42
2.10	Example of how physical mesh design can reduce the number of elements. .	43
2.11	Initial finite element mesh of the modeled vapor intrusion scenario. . . . .	46
2.12	Original and adaptatively refined mesh. . . . .	49
2.13	Convergence of indoor air contaminant concentration as the mesh is refined.	50
2.14	Modeled Darcy's pressure field in soil . . . . .	51

2.15 Modeled contaminant concentration in soil . . . . .	52
2.16 Airflow velocity $\vec{u}_g$ [mm h <sup>-1</sup> ] near the foundation crack with associated its streamlines. . . . .	53
2.17 Analysis of horizontal diffusion flux. . . . .	53
2.18 Volume plot showing where the cell Péclet number exceeds 1 and its actual value. I.e. it suggests where the mesh may be improved. . . . .	54
3.1 Visual summary of some of the different ways that contaminant can transport into a VI affected building via preferential pathways. Figure from McHugh et al.[22]. . . . .	64
3.2 The "ASU house" VI site in Layton, Utah. . . . .	65
3.3 Analysis of the indoor contaminant concentration at the ASU house. . . . .	67
3.4 Regression plot showing the indoor/outdoor pressure difference dependence on indoor air concentration. . . . .	68
3.5 The "EPA" duplex VI site in Indianapolis, Indiana. . . . .	70
3.6 . . . . .	71
3.7 Relationship between indoor/outdoor pressure difference and indoor contaminant concentration of three contaminants - TCE, PCE, and chloroform at the EPA duplex. . . . .	72
3.8 The modeled preferential pathway VI scenario. . . . .	75
3.9 Meshed geometry of the preferential pathway model. Notice the gravel sub-base layer and the preferential pathway exit near the left hand foundation crack. . . . .	76
3.10 Predicted indoor air concentration compared to the ASU house. . . . .	81
3.11 How different cases affect the predicted impact of the preferential pathway. .	83
3.12 Péclet number for transport through the modeled foundation crack. . . . .	84
3.13 Effect of different air exchange rate on predicted indoor contaminant concentration. . . . .	87

3.14 Predicted indoor contaminant concentration using diurnal building pressurization and air exchange rates as inputs. . . . .	89
3.15 Distribution of TCE contaminant vapors in the subsurface underneath the ASU house. . . . .	91
3.16 Boxplot showing the distribution of $\alpha_{\text{subslab}}$ considering the effects of CPM and the ASU house land drain preferential pathway. . . . .	92
3.17 Interpolated soil-gas contaminant concentrations for select contaminant underneath the EPA duplex. . . . .	96
4.1 Predicted effect of soil and foundation type on the Péclet number of transport through the foundation crack. . . . .	100
4.2 Building pressurization and indoor contaminant concentration were highly correlated at the North Island Naval Air Station (NAS) VI site. . . . .	103
4.3 Boxplot showing the log-10 transformed TCE concentrations measured at the ASU house as a function of whether the preferential pathway was open or closed. . . . .	105
4.4 Boxplot showing the distribution of air exchange rate values at the ASU house, considering the effect of CPM. . . . .	107
4.5 Seasonal distribution of indoor contaminant concentration at the ASU house and EPA duplex. . . . .	108
4.6 Seasonal distribution of indoor contaminant concentration at the ASU house. .	109
4.7 Temperature and wind contribution to building pressurization. . . . .	118
4.8 Boxplot comparing the predicted $p_{in}$ to the recorded values, and how the temperature and wind components contributes to the distribution of values. .	119
5.1 Schematic of experimental setup. . . . .	125
5.2 Schematic of the modeled vapor intrusion scenario. . . . .	127

5.3 Experimental data of sorption of TCE onto three select materials as well as fitted sorption rates based on the kinetic model (5.31). . . . .	134
5.4 The influence of contaminant sorption in soil. . . . .	136
5.5 The influence of contaminant sorption in soil. . . . .	139
5.6 Comparison of how sorption onto/from various indoor materials affect the indoor air contaminant concentration of a building that undergoes a certain pressurization cycle. . . . .	141
5.7 Contaminant desorption from indoor materials delay the decrease in indoor contaminant concentration after a mitigation system has been implemented.	145

# List of Tables

2.1	Inputs to COMSOLs meshing algorithm. . . . .	44
3.1	Air exchange rate values [ $\text{h}^{-1}$ ] . . . . .	87
4.1	Division of wind direction into discrete cardinal directions with associated pressurization or depressurization of the heated "right hand side" of the EPA duplex. . . . .	114
4.2	Mean and standard deviation of recorded and weather predicted building pressurization. . . . .	117
5.1	Fitted kinetic sorption parameters based on sorption experiment data. Six different types of materials are considered. $k_1$ and $k_2$ are the sorption and desorption constants respectively, and $K$ is the sorption equilibrium constant. . . . .	134
5.2	The assumed contaminant penetration depth and subsequent volume of the sorbing indoor materials. . . . .	140
B.1	Properties and van Genuchten parameters of select soil types[92]. . . . .	168

*Abstract of Understanding the Dynamics of Vapor Intrusion Processes, by Jonathan G. V. Ström, Ph.D., Brown University, May 2020.*

Vapor intrusion (VI) investigations, the effort to determine the exposure and associated human health-risk at a VI impacted building, are often complicated by significant spatial and temporal variability in concentrations of contaminants of concern. Over the years there have been efforts to develop new techniques and methodologies that aim to reduce the uncertainties associated with these variabilities. The goal is to simplify and improve the robustness of VI site investigations. The development of the controlled pressure method (CPM), where the pressurization of a building is controlled in an effort to increase or decrease contaminant entry into the building, is one such example. Another approach is to use indicators, tracers, and surrogates (ITS) to help guide when to conduct site investigations, ideally increasing the likelihood of determining the maximum indoor contaminant concentrations.

Both of these approaches rely on a quasi-deterministic relationship between some external variable, such as building pressurization, and indoor contaminant concentration. However, site-specific conditions can give rise to very different responses to such an external variable. To effectively use CPM or ITS, a better mechanistic understanding of contaminant transport and exposure is needed.

In this thesis, we develop three-dimensional finite element models of VI impacted buildings from a first principles perspective. These models combined with analysis of field data from VI sites, allows us to explore the physical mechanisms that drive VI. By considering the dominant contaminant transport mechanism at a site, e.g. if advective or diffusive transport dominates, we can explain why a change in building pressurization can lead to differences in contaminant concentration variability at different sites. We can also better understand how the various factors governing VI contribute to the overall variability.

By classifying the dominant contaminant transport mechanism at a site, we can more effectively anticipate how a particular site will respond to some external stimuli. This will in turn reduce the effort required to, and increase the robustness of the techniques used

determine the relevant human exposure at a VI site.

We also applied the model to investigate the role of contaminant sorption to and from soils and common materials. Sorptive capacities of these materials were determined experimentally at relevant conditions, and found that some materials, such as cinderblock, can hold up to 41,000 times more contaminant than a comparable contaminated air volume. Sorption and desorption of contaminant can significantly delay changes in contaminant concentration with respect to time, both in the soil-gas and in the indoor environment. This phenomena is particularly relevant after successful implementation of VI mitigation scheme, where contaminant desorption from certain materials may maintain indoor contaminant concentrations for months longer than if there were no sorbed contaminants.



# Chapter 1

## Introduction

### 1.1 Indoor Air Quality and Vapor Intrusion

Concerns about air quality are as old as civilization itself, ranging from beliefs that disease is caused by bad air - a *miasma*, to more recent concerns about exposure to combustion particulates, radon gas, or other air-borne pollutants. Since industrialization the number of potential hazardous pollutants has increased significantly, followed by increased concerns about air quality. At the same time, people now spend more time indoors now than ever before, with Americans spending up to 90% of their waking time indoors[1]. This change in human habitation has put a special emphasis on indoor air quality.

Some early scientific inquiries into indoor air quality focused on pollutant sources that were generated in the home, e.g. by heating and cooking systems, and these types of pollutants are still relevant today, but of particular concern in developing countries[2, 3]. Many buildings materials can also cause indoor air quality issues, with exposure to asbestos fibers being perhaps one of the more famous examples of this. Mold is another common indoor quality concern[4].

In the 1970s, to address the growing public health concerns, research began into the potential exposure to radioactive radon gas in buildings. Radon gas, which is generated by

the decay of naturally occurring uranium in soils and rocks, was found to be able to enter overlying building and expose the inhabitants. This phenomena came to the public attention in the mid 1980s, after a Pennsylvanian nuclear power plant worker set off radioactivity sensors at the plant, the actual cause of which was the high concentration of radon gas in the workers home[5]. Exposure to radon gas can significantly increase the risk of developing lung cancer, and is to this day the second leading cause of lung cancer in many countries[6]. With the discovery of radon intrusion into buildings, it did not take long for the same concerns to be extended to the entry of anthropogenic contaminant vapors - vapor intrusion (VI).

Vapor intrusion is the migration of contaminant vapors from a contaminant source, often contaminated groundwater, into the overlying buildings. These vapors evaporate from the contaminated groundwater and enter through cracks in the building foundation, gaps between walls and floors, sump pits, or other openings[7]. In these aspects, VI is more or less similar to radon intrusion, and thus much of the early VI research was heavily influenced by the work done by radon intrusion researchers. This is largely true to this day, but vapor intrusion differs in some non-trivial ways, that make it an unique issue. Many of these differences stem from the properties of the contaminants themselves, and from the fact that many of the VI contaminants that we concern ourselves with, mainly volatile organic compounds (VOCs) and chlorinated solvents, are of anthropogenic origins.

One difference is that radon is unstable, and has a half-life of around 3.8 days (at least  $\text{Rn}^{222}$ , the only naturally occurring isotope of radon), and it follows that radon accumulation will be naturally mitigated, which is not the case with other contaminants[8]. The closest analogy is that certain VOCs of VI concern are able to be biodegraded by bacteria in the soil, but this effect can vary significantly as this process is oxygen limited[7, 9].

A more significant difference is the anthropogenic origin of VI contaminants. In VI, we often are concerned with a contaminated groundwater source underneath the afflicted building, and the source of the groundwater contamination typically originates from some

contaminant spill at one or more sites in the surrounding area. Thus, a large number of buildings may be impacted by VI via a single contaminant source. The origins of such spills are numerous, but any activities that employ the contaminants of VI concern are possible culprits[7]. In the United States (US), the Environmental Protection Agency (EPA) maintains a list of significantly polluted sites throughout the country, so called Superfund sites, and as of 2020 there are 1335 recorded sites, many of which contain the contaminants of concern[10, 7]. Additionally, many of the contaminants of concern do not readily degrade, and legacy contamination is an issue[7]. It should also be noted that VI from a contaminated groundwater is only one type of contaminant source, with leaky subsurface tanks, spills into soils, etc., likewise being contaminant sources of concern. Figure 1.1 shows some of the VI processes.

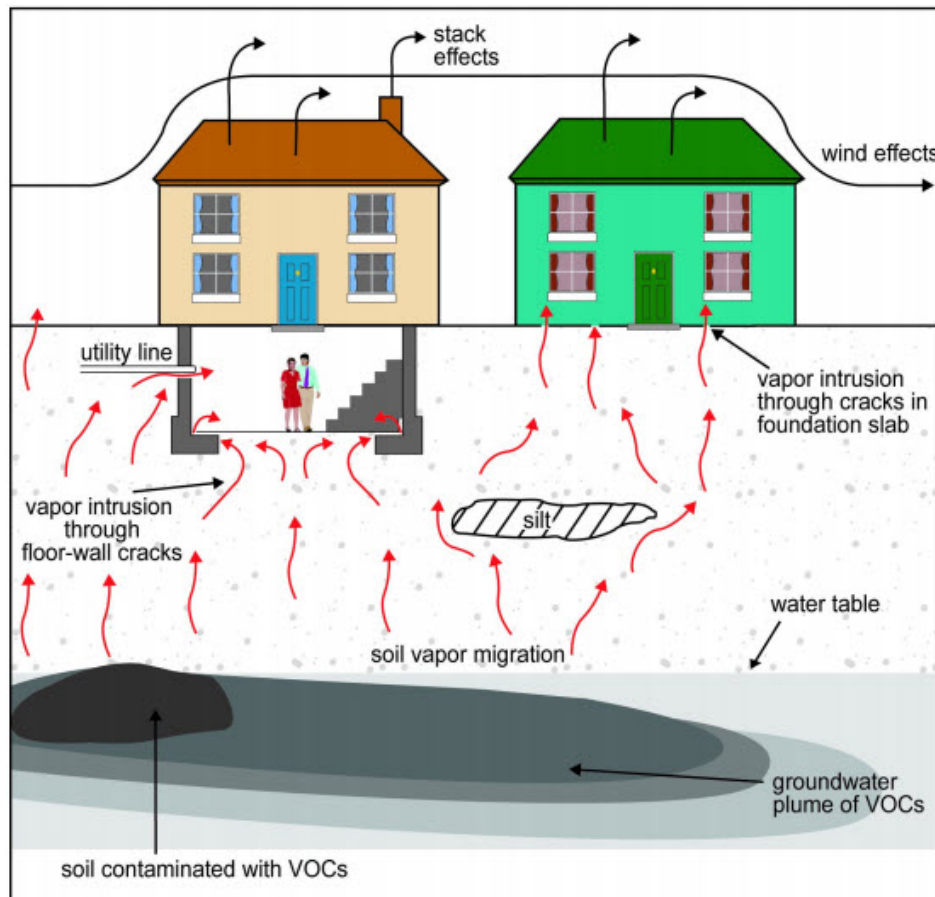


Figure 1.1: Vapor intrusion into a building can occur through a variety of means, from a variety of sources. Figure from the EPA[11].

In VI, some common contaminants of concern are chlorinated solvents such as trichloroethylene (TCE), tetrachloroethylene (PCE), or chloroform. Various other organic compounds such as benzene, or other petroleum products are also of concern. Out of the various VI contaminants, TCE has emerged as of perhaps particular concern. TCE is an excellent degreaser and has seen extensive use as such, and has been commonly used by dry cleaners, the military, auto repair shops etc[7]. The concern over TCE is partly due to its associated cancer risk and partly because it was recently hypothesized to possibly play a role in birth defects. A review study by Makris et al.[12] showed that TCE may be associated with increased risk of congenital heart defects (CHD), but a more recent study by Urban et al.[13] concluded that, mainly due to reproducibility issues and new studies, there is not adequate evidence to support that TCE causes CHD. Regardless, it is carcinogenic and surprisingly despite the concerns about its health effects, its use remains legal.

Considering the widespread existence of potential VI sites and the associated health concerns, an industry for identifying and characterizing these sites and either remediating or mitigating them has emerged. This is particularly true in the US, where the law dictates that the responsible party of the contaminant spill or release is liable for cleanup and mitigating human exposure. In this situation significant effort is spent on determining liability. Determining if VI occurs at a particular site, as we will see in this work, is not easy, and while VI has been studied for decades, many questions and challenges remain, in particular with regards to the great spatial and temporal variability that exist both within and between VI sites[7].

## 1.2 Issues In Vapor Intrusion Investigations

Determining if vapor intrusion occurs at a building is often difficult. One might be tempted to believe that collecting an indoor air sample inside the building would be sufficient, i.e. that if the vapor contaminant concentrations is over some threshold in the house, this proves

that VI occurs, and the absence of contaminant vapors is proof that no VI occurs. However, this approach is too simplistic and may yield false positives.

Many common consumer products contain the same contaminants that are of concern in VI, and the presence in the home of e.g. a gasoline-containing storage vessel may be the culprit. Not all indoor contaminant sources are so obvious though, and many contaminants may be inadvertently introduced, such as by bringing home newly dry-cleaned clothing (a common source of PCE). Great care is taken to eliminate such indoor sources during formal VI investigations, but this can be challenging[7].

A compounding issue related to this is that many of the contaminants can sorb onto/into various materials and subsequently desorb for significant periods of time, potentially extending the influence of indoor sources beyond their removal[14, 15]. This a phenomena, among other related issues with sorption, we will discuss in Chapter 5.

Since indoor air sampling may not alone prove that VI occurs, investigations usually involve further steps. One possibility is to collect air samples right below the foundation of the building, and if contaminant vapors are found there, as well as in the indoor air, that is more compelling evidence that VI occurs. However, as work by Holton et al.[16] has shown, contaminant vapors in the indoor environment may actually migrate from inside the building to the subslab, creating a contaminant cloud in soil beneath the building that may persist for significant periods of time.

Collecting samples from the contaminant source, such as the groundwater underneath a building, to determine the presence of contaminants can be used as potential evidence of VI. However, even identifying such a potential source is not enough evidence of VI, as the presence of a contaminant source does not mean that the contaminant vapor actually enters the overlying building. Folkes et al.[17] conducted a decade long study of VI sites in Redfield, Colorado, and a 19 month long study in New York showed that many of the sites, even though they were above a contaminated groundwater source, were not impacted by VI.

Often investigators take samples from different locations, those already discussed as well

as soil-gas samples, and compare the relative decrease in contaminant vapor concentration from the source to the indoor to establish what is termed a "completed pathway". This decrease is called *attenuation* and is quantitatively represented in concentration from one point to the next as an *attenuation factor*. For example, in one particularly widely used form of the attenuation factor, the indoor contaminant concentration is divided by the contaminant concentration at the soil-gas groundwater interface.  $\alpha$  is commonly used in this work to denote attenuation factor and we will often use a subscript to denote attenuation from one measurement point to another. In the case of groundwater attenuation for instance, one would divide the indoor contaminant concentration by the groundwater contaminant vapor concentration (that is when the contaminant concentration is in equilibrium with air, e.g. Henry's Law).

$$\alpha_{\text{gw}} = \frac{c_{\text{in}}}{c_{\text{gw}} K_H} \quad (1.1)$$

Where  $\alpha_{\text{gw}}$  is the attenuation from groundwater;  $c_{\text{in}}$  [ $\text{mol m}^{-3}$ ] is the indoor contaminant concentration;  $c_{\text{gw}}$  [ $\text{mol m}^{-3}$ ] is the groundwater *liquid phase* contaminant concentration; and  $K_H$  is the dimensionless Henry's Law constant.

Over time, the U.S. Environmental Protection Agency (EPA) has compiled data on attenuation factors relative to different source depths and types. Using these data, standards as to which attenuation factors are expected have been established to help guide investigators and regulator determine the VI risk. This is helpful, but often we are faced with VI sites that render these sort of standards difficult to use. For instance, the EPA recommends that an attenuation from the subslab region to the indoor of  $\alpha_{\text{subslab}} \approx 0.03$  for determining if VI occurs. In reality, attenuation factor values can vary by orders of magnitude due to a variety of factors, and that these recommended values can therefore be too conservative[18].

Some of the factors influencing attenuation factors are soil heterogeneity, nonhomogeneous contaminant source concentrations, as well as differences in the nature of the source (e.g. a contaminant spill in the soil itself vs. a leaky underground chemical tank). These can all contribute to significant spatial variability in contaminant concentration at a site.

A good example of this is seen in a study by Luo et al.[19] where contaminant concentration beneath a building foundation varied from 200 to less than 0.01 mg/L. Bekele, Naidu, and Chadalavada[20] also found that TCE soil-gas concentration could vary by an order of magnitude underneath the foundation of another site.

Likewise, not all indoor environments are perfectly mixed and indoor contaminant concentration can vary significantly between different rooms or compartments in a building. This was observed at a site in Boston, Massachusetts by Pennell et al.[21] who found that the indoor contaminant concentration was significantly higher in the upstairs bathroom than in the basement, where one typically would expect higher concentrations.

The work by Pennell et al.[21] further revealed that VI could occur through sewers and enter the building through broken plumbing fixtures, which requires considering another level of complexity in VI - associated with the existence of preferential pathways. A preferential pathway is a term used describe something permitting enhanced contaminant vapor transport to near or into a building, in contrast with the more "traditional" view that contaminant transport occurs through soil. McHugh et al.[22] studied a VI impacted building in Indianapolis, Indiana, and found that the sewer system there acted as a preferential pathway bringing contaminants into the house (in addition to the soil pathway from the contaminated groundwater). There contaminated groundwater infiltrated into the sewer system a few blocks away from the site.

Similarly, Guo et al.[23] studied a site in Layton, Utah, that was found to be impacted by a sewer connected land drain that allowed contaminant vapors to be transported to the near-slab region beneath a house (and close to a visible breach in the foundation). The results of this study and the role of the preferential pathway is a significant focus of this work and will be discussed in more detail in Chapter 3.

Holton et al.[24] (same group as Guo et al.) demonstrated the very significant temporal variability in indoor contaminant concentrations that exist at some sites, where they found close to four orders of magnitude in variability during the multi-year study period. Hosan-

gadi et al.[25] studied another site in San Diego, California, that likewise showed orders of magnitude temporal variability, albeit on a shorter time scale. Also, the aforementioned site in Indianapolis exhibited significant temporal variability[8].

This temporal variability often has a seasonal component, and the highest indoor contaminant concentrations are usually found during the colder months of the year[8, 24], although there are cases when the opposite is true. Steck et al.[26] shows this at a radon impacted building in Minnesota, where the highest radon levels were observed during summer. Some authors such as Bekele, Naidu, and Chadalavada[20] suggest that it may be necessary to collect samples at intervals across a full year, to account for all seasonal effects, to avoid mischaracterization of VI.

The complexity and nuances of VI has made it necessary for a multiple lines-of-evidence (MLE) approach to be taken when determining if a building is impacted by VI[7, 27]. However, the complexities associated with this approach has prompted the development of new methodologies and techniques that can reduce the uncertainty and complexity associated with conducting VI site investigations.

## 1.3 Innovations In Vapor Intrusion Investigations

In an attempt to reduce the uncertainty in determining human exposure due to vapor intrusion caused by the significant spatial and temporal variability in VI, a number of new investigatory techniques and methods have been proposed, but in general their efficacy is yet to be fully established[28]. This work won't deal with all of these exhaustively, but rather primarily address two approaches (together with other topics related to variability.)

### 1.3.1 Controlled Pressure Method

Most buildings are naturally depressurized relative to atmosphere due to the operation of heating, ventilation, and air conditioning systems, and the so-called stack effect, a topic that

will be covered in greater detail in Chapter 4. This depressurization induces a flow of air from soil into the building; this flow can carry contaminant vapors into the building. (This view is rather simplistic, as will be discussed throughout this work, but suffices for now.) Using this idea, the controlled pressure method (CPM) was suggested, where blowers are used to control the depressurization of the building, and thereby more effectively control the indoor environment (see Figure 1.2). The basic idea was to create a "worst case" scenario in which contaminant soil vapors are induced to enter the building.

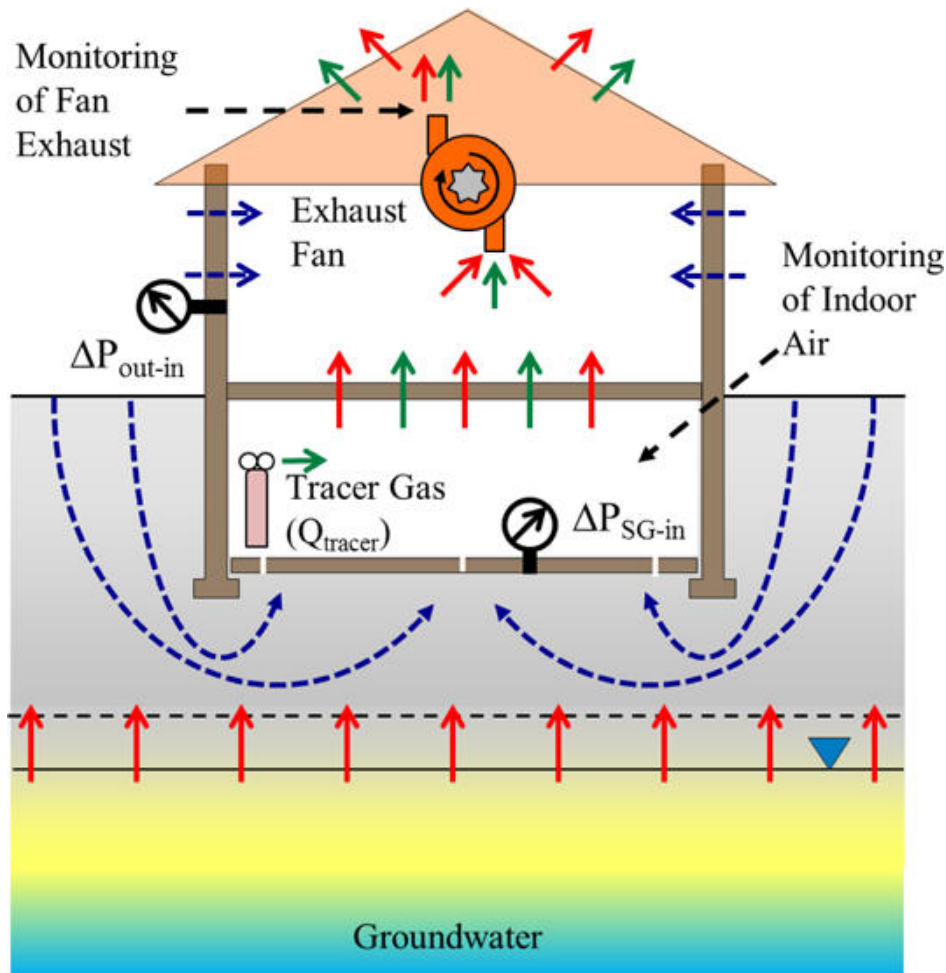


Figure 1.2: Conceptual idea of the controlled pressure method - a VI impacted building is forcefully pressurized using a blow, theoretically controlling the contaminant entry into the building. Figure from Holton et al.[29].

Within the CPM framework, overpressurizing a building will then prevent contaminant entry from occurring. Thus, this can be used to identify indoor contaminant sources, as

the presence of any contaminant vapors in the indoor environment in the overpressurized building have to originate from such a source. This approach can be applied as needed and hopefully will reduce the uncertainty and difficulty of VI investigations[30].

### 1.3.2 Indicators, Tracers, and Surrogates

The conventional sampling schemes currently employed, due to the spatial and temporal variability of VI, has a propensity for creating false positives and negatives. While one solution to this problem is to increase the scope of VI investigations of a particular site, by for instance continuously monitoring the indoor contaminant concentration or by collecting an increasing number of samples, this approach is not practical, especially when numerous sites are involved. Thus, there is a need to develop guidelines that help reduce the sampling requirements and scope of VI investigations, while retaining the same degree of confidence that the relevant level of VI has been determined[31].

To achieve this, it has been suggested to use indicators, surrogates, and tracers (ITS) to determine when to conduct a VI site investigation. For example, one question that has been posed is if meteorological ITS be used to determine when VI is expected to be the greatest, e.g. at which temperature and barometric pressure is, for instance, the 95th percentile indoor contaminant concentration most likely to be found[31]? This is a promising approach, because as we have already discussed, many VI sites have the highest indoor contaminant concentration during colder seasons. So far this is more of a qualitative observation rather than quantitative guidelines for use in VI site investigations.

## 1.4 Issues With Applying CPM and Using ITS

On the surface, the CPM and ITS methods are two different approaches that try to address the same problem. However, they both attempt to utilize some external variable, such as building pressurization, and either manipulate it directly, or by inference, to determine or

predict the indoor contaminant concentration.

The issue with these approaches is that they assume that different VI sites will respond comparably to these external variables, which in reality is not the case. Guo et al.[23] used CPM to (inadvertently) identify a preferential pathway at their site, closed it, and noticed a markedly different relationship between indoor contaminant concentration and building pressurization for the period before and after the closing of the preferential pathway.

The reason for this change in behavior will be elaborated on in Chapter 3, but consider that contaminant transport from soil into a building across a foundation breach occurs by two means - diffusion and advection. If advective transport dominates, then one would expect a strong correlation between building pressurization and contaminant entry rate, which determines the indoor contaminant concentration; if diffusive transport dominates, this relationship would be absent or weak.

Thus, to reliably apply any technique such as CPM or to use ITS, one needs a good mechanistic understanding of how, for instance, contaminant transport occurs at a VI site, and how the various site specific characteristics give rise to different transport phenomena. Assessing this in the field can be challenging, and therefore we turn to the use of numerical models of VI scenarios, guided by a first-principles perspective, which gives the ability to study physical phenomena in great detail.

## 1.5 Mathematical Modeling of Vapor Intrusion

Early in the history of VI, mathematical models of VI were formulated to aid investigators and regulators predict human exposure risk. Most of these adapted work done by Nazaroff[32] who had developed mathematical models of radon intrusion. Perhaps one of the more widely used VI models was the one developed by Johnson and Ettinger in 1991[33]. This analytical model could be used to describe the transport of various VI contaminants from a groundwater source into the overlying building, and it was quickly adopted by the EPA as a spreadsheet

tool that has seen widespread use since that time[7]. Over time more advanced numerical models were developed, which allowed for more physical features to be added for VI scenarios to be modeled in greater detail. Some notable examples are the work by Abreu and Johnson[34] and Pennell, Bozkurt, and Suuberg[35].

A benefit of using models in VI, besides as a predictive tool, is that their use allows the user to inspect in detail the role that various physics plays in determining VI. In a field that is dominated by empirical field studies of VI sites (which are environments that are difficult to control), models are an invaluable tool that help deepening our understanding of the VI phenomena. Already these models have been used to investigate topics such as the role of soil moisture in VI transport[36], how different foundation features affect contaminant entry[37], or how wind and outdoor temperature affects building air exchange with the outdoor and pressurization[38].

In this work, we will likewise use numerical models, in combination with analysis of field-data from well-studied VI sites to explore the nature of contaminant transport. Some specific topics that will be covered include analysis of how preferential pathways can fundamentally change contaminant transport, and how the lessons learnt can be used to aid in resolving some of the issues in VI investigations, and broaden our understanding of the temporal and spatial variability at VI sites. The role that sorption of contaminant vapors on soils and in the indoor environment, a largely unstudied phenomena, will also be explored, and some of the implications discussed.

## 1.6 Outline

Numerical models of VI scenarios will be used throughout this work, and understanding the underlying mathematics that governs VI, as well as how these models are implemented, are crucial for understanding this work. Chapter 2 covers these aspects of VI modeling, where we develop a model of a hypothetical VI scenario. Here, the governing equations

will be introduced, as well as the finite element method (FEM), which will be used to solve our model. In this process, we will cover the work of constructing a model geometry mesh, configuring solvers, post-processing results, and a variety of practical considerations when modeling VI. Lastly, a brief summary of VI models and recent developments will be addressed.

With this knowledge of VI modeling, we will first use them to tackle the issues of preferential pathways in Chapter 3. A significant focus is placed on modeling and analyzing the preferential pathway found at the "ASU house" VI site in Layton, Utah. This work will demonstrate how and why preferential pathways can contribute so greatly to temporal and spatial variability in VI. The preferential pathway at "EPA duplex" VI site in Indianapolis, Indiana, will also be explored here.

From the work in Chapter 3, we find that it is important to consider if vapor contaminant transport from the subsurface into a building is dominated by advective or diffusive transport, a topic that will be further explored in Chapter 4. Here we discuss some of the site specific conditions that give rise to either of these transport mechanisms to dominate. These conclusions have wider implications for CPM or using ITS, and the efficacy of these investigative methods can hinge on characterizing the dominant transport mechanism at a site. We also explore how weather conditions and outdoor temperature can be used to predict building pressurization, which becomes an important potential ITS for advection dominated sites.

In Chapter 5 the role that sorption of vapor contaminant in the indoor environment and onto soil particles is explored. The capacity of a variety of common materials to sorb TCE are measured at relevant conditions, where we find that these capacities can vary by orders of magnitude. These sorption data are then applied to a VI model, where the potential influence of these sorption effects on contaminant transport, VI investigations, and application of mitigation systems.

Lastly, Chapter 6 provides a summary of the conclusions and findings in this thesis, and

suggestions future work.

# Chapter 2

## Numerical Modeling of Vapor Intrusion

### 2.1 Summary

In this chapter we develop and solve a numerical model that simulates vapor intrusion (VI) at a house overlying a contaminated groundwater source. The purpose of this chapter is to introduce VI modeling and the necessary fundamentals of how models are used in this work. The physics and associated governing equations required to model this scenario are presented, as well as the necessary initial and boundary conditions to solve these equations. This model is solved using the finite element method (FEM), which is briefly described, and this choice discussed. Practical considerations of implementing a FEM model are covered - including geometry and mesh generation, solver configuration, and post-processing of results.

### 2.2 Introduction

To formulate a mathematical description of VI, we consider a simple hypothetical VI scenario at steady-state and develop a three-dimensional model of this. Consider a VI impacted house with a 10 m by 10 m foundation footprint with a basement whose foundation lies 1 m below

ground surface (bgs). There is also a 1 cm wide crack along the perimeter of the 15 cm thick foundation slab, where all contaminant vapor entry into the house is assumed to occur. Here we will consider the basement alone as the control volume for which the indoor contaminant concentration will be determined. It is assumed to have a ceiling height of 3 m, giving a total volume of  $300 \text{ m}^3$  and that contaminant vapors are expelled via air exchange with the exterior of the house; the air exchange rate with outdoor air is assumed to be  $0.5 \text{ h}^{-1}$ .

The contaminant source is the underlying groundwater, which is assumed to be 4 m bgs, and it is infinitely and homogenously contaminated with TCE (we will normalize everything to this source concentration, so the value does not matter), i.e. the groundwater contaminant concentration does not change over time nor does it have any concentration gradients. We will only consider contaminant transport in the portion of soil between the open ground surface and the groundwater interface - the *vadose zone*. This soil is assumed to be homogenous and consist only of *sandy loam* type soil, i.e. there are no soil layers, rocks, etc. For now, we will assume that no contaminant sorption into/onto the soil occurs, but this phenomena will be explored in Chapter 5. The house is assumed to be surrounded by open ground that extend 10 m from the house wall. Contaminant concentration in the atmosphere is assumed so low that is effectively zero, i.e. contaminant vapors that reach the ground surface are immediately infinitely diluted.

The house interior is assumed to be slightly depressurized relative to ambient due to the stack effect; the indoor/outdoor pressure difference is  $-5 \text{ Pa}$ . This induces an airflow from the ground surface, through the soil, and into the house via the foundation crack. The airflow interacts with contaminant diffusion in the soil. Figure 2.1 shows a figure summarizing this VI scenario.

The basement interior will be modeled as a continuously stirred tank reactor (CSTR), (but without reactions), where the indoor contaminant concentration will depend on the contaminant entry rate  $n_{ck}$  from the soil via the foundation crack and the air exchange rate  $A_e$ . The details of this will be covered section 2.5.1.

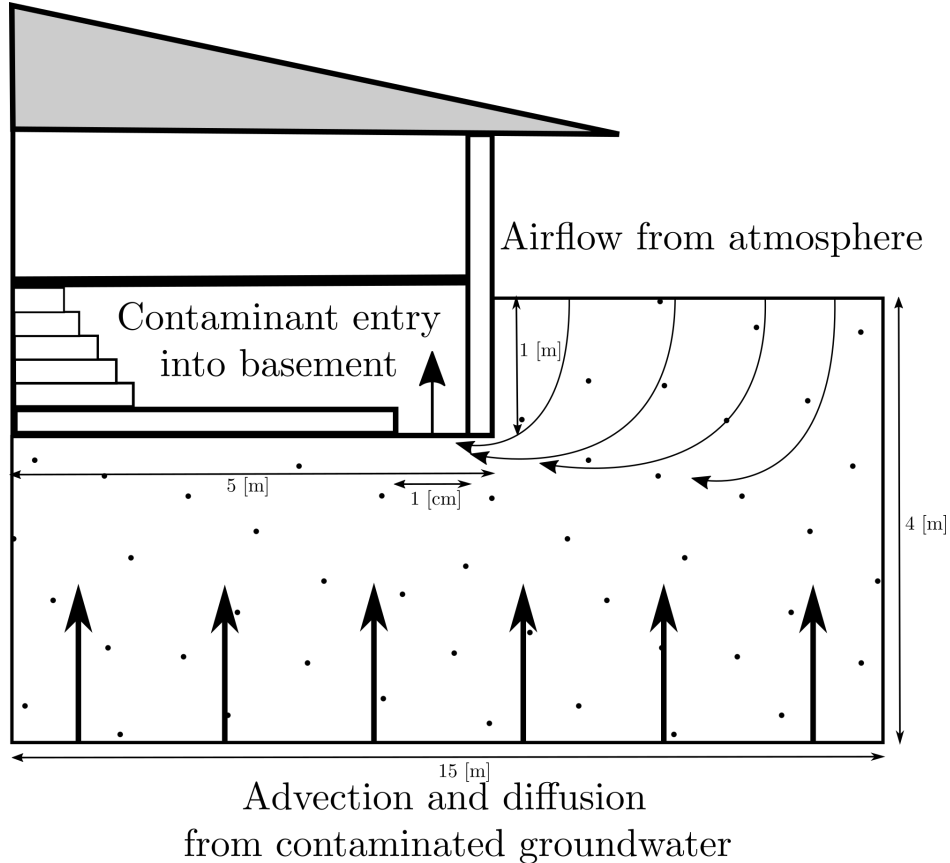


Figure 2.1: The considered VI scenario.

To determine  $n_{ck}$  the contaminant transport in the soil needs to be modeled. This will be done using the advection-diffusion equation, which will be modified for transport in soils. The contaminant transport itself is driven by a concentration gradient (leading to diffusive transport) and airflow (leading to advective transport) in the soil. The contaminant source (groundwater) and sink (atmosphere and contaminant entry into the building) will largely determine the concentration gradient, while the airflow needs to be calculated separately.

The airflow in the soil is modeled by Darcy's Law, and is driven by a pressure gradient in the soil, which induced by the indoor/outdoor pressure difference at the interface between soil and building foundation. Details are discussed in section 2.5.3.

One last consideration is that the vadose zone is generally partially saturated with water, with the soil pores more or less water-filled near the groundwater interface, and with soil moisture content decreasing as a function of elevation above groundwater  $z$  [m]. The soil

moisture content has a profound effect on transport in the soil; it restricts both the airflow and contaminant diffusivity in the soil. Thus, the soil moisture content  $\theta_w$  must first be determined in order to solve the contaminant transport and Darcy's Law.

The resulting physical system is highly coupled, with many physical aspects dependant on others. Figure 2.2 shows the coupling between each physcals process, its output, and how it relates to the other processes that ultimately determine VI.

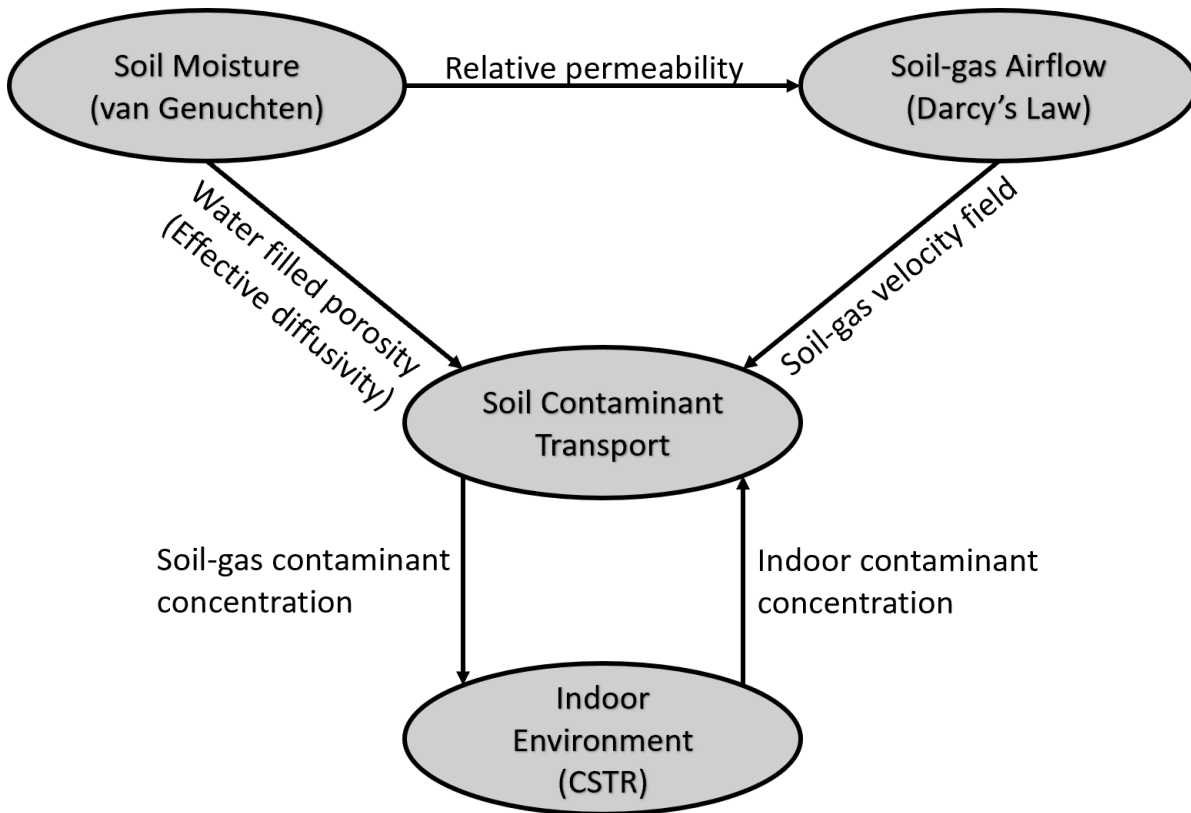


Figure 2.2: Coupling between the physics used to model VI.

In this chapter, we will walk through the process of numerically modeling this VI scenario using the finite element method (FEM) and post-processing of the results. A discussion regarding past and present VI models, their advantages and limitations, will follow. Note that a particular numerical values cited above have been chosen to be "typical" of a VI scenario. Clearly other values can be chosen for most of the parameters. When results are presented below, the sensitivity of the results to particular parameter choices will be

explored.

## 2.3 Finite Element Method

Many physical phenomena are described by partial differential equations (PDEs), but for anything but the simplest scenarios, these do not have an analytical closed-form solution; therefore numerical methods are needed for finding an approximate solution. This is achieved by discretizing the problem, i.e. transforming a continuous problem into a discrete one. There are numerous ways to discretize a problem, and some of the more popular schemes are finite difference (FDM), finite volume (FVM), and finite element method (FEM).

In this work we use FEM, which is a popular numerical scheme that offers some distinct advantages over other schemes for modeling VI. FEM subdivides the domain of the PDE problem into many smaller subdomains called elements. These elements can take a wide variety of shapes, e.g. tetrahedra, prisms, or cuboids for three-dimensional problems and triangles or rectangles for two-dimensional problems. The collection of elements that make up the domain or geometry is called a *mesh*. The fineness of the mesh is what largely determines the accuracy of the solution, but also increases the computational costs.

The size of each element can be highly nonuniform which allows FEM to discretize complicated geometries. This is advantageous for modeling VI, where different parts of the geometry can have dramatically different resolution requirements; the 1 cm foundation crack requires elements on the scale of mm, while in other parts of the geometry the resolution requirement is on the scale of m. This ability to easily represent complicated geometries with elements of non-uniform sizes helps maintain accuracy while saving computational resources. Another benefit of using these elements is that it is easy to assign different constant values throughout the domain, and heterogenous materials can easily be represented.

The purpose of this work is not to provide a detailed description of the finite element method (FEM), but rather motivate the choice is using it over other numerical schemes

and give some practical considerations of using it. For the interested reader, there exists a wide body of work regarding FEM, and in this work *The Finite Element Method: Theory, Implementation and Applications*[39] is continuously used as a source.

However, it is important to understand what determines the quality of the approximated solution. For numerical schemes such as FDM, the quality of the solution is directly related to the fineness of the discretization (either in time or space). While this is also true for FEM, there is another aspect that helps determine the quality of the approximated solution - the choice of *basis function*.

Say that the function  $u$  is the exact solution to some PDE in a given interval  $I$ ,  $u$  can then be approximated by  $u_h$

$$u \approx u_h \quad (2.1)$$

where  $u_h$  is a linear combination of basis functions and their respective *nodal coefficients*.

$$u_h = \sum_i^n u_i \psi_i \text{ in } I = [x_0, x_n], \quad i = 0, \dots, n \quad (2.2)$$

$u_i$  is a nodal coefficient;  $\psi_i$  is a basis function; where  $x_0$  and  $x_n$  are the end nodes of the interval  $I$ .

One of the key purposes of the basis functions is that they are used to transform a continuous PDE problem into a discrete one. Exactly how this is achieved is not further described here, and the reader is referred to *The Finite Element Method: Theory, Implementation and Applications*[39] for such details. What matters is that the discretization results in a linear system of equations that may be solved to find all of the nodal coefficients  $u_i$ . A wide variety of basis functions may be used, but simple ones are usually chosen, e.g. a "hat" functions or some lower-order polynomial, but it is not restricted to these.

An example of an approximation to some solution  $u$  by  $u_h$  as a linear combination of "hat" basis functions can be seen in Figure 2.3. The combination basis functions  $\psi_i$  with their respective nodal coefficients  $u_i$  form  $u_h$  which form a piecewise linear approximation

of  $u$ . This also shows why basis functions are often called *interpolation functions* - they can be used to find the value of  $u_h$  between nodes. And just as when choosing functions for an interpolation scheme, i.e. whether to use piecewise linear or cubic splines, the choice of basis functions in FEM can affect the quality of the solution.

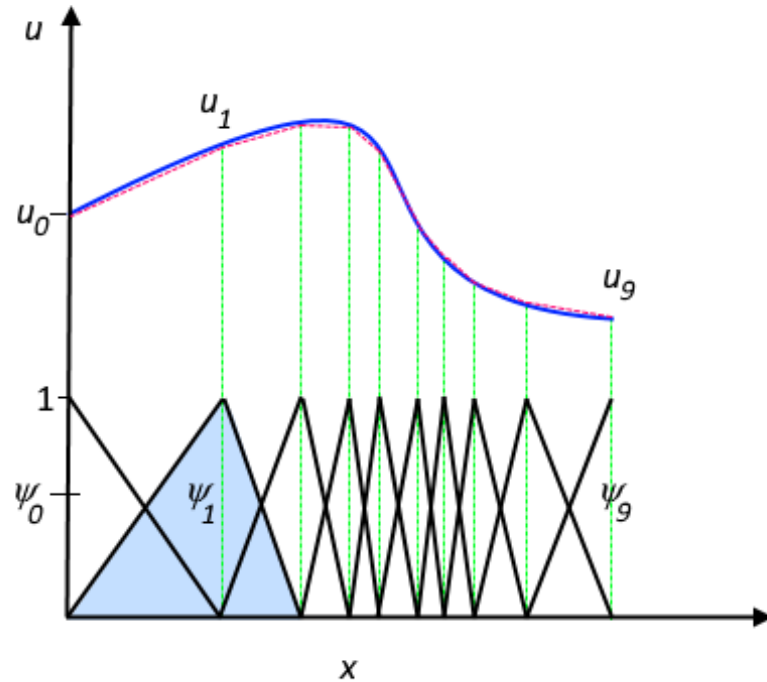


Figure 2.3: The exact solution  $u$  to some PDE (blue line) and its approximate solution  $u_h$  (dashed red line). The "hat" basis functions  $\psi_i$  (black lines) for each element of the interval. The combination of the each nodal coefficient  $u_i$  and basis function  $\psi_i$  form the piecewise linear approximation  $u_h$  of  $u$ . Figure from COMSOL[40].

Using a higher-order basis functions can be much more computationally expensive, and thus typically simple ones are favored - such as hat functions or second order polynomials. The fineness of the mesh becomes more important with simpler basis functions, and becomes the primary means for improving the solution quality. However, there are circumstances when increasing mesh fineness is impossible, and in such cases choosing a higher-order basis function may improve the quality instead.

In this work we use a commercial FEM software called COMSOL Multiphysics, where

subsequent sections will cover the steps required to implement our VI model in COMSOL.  
(Of course, this could easily be translated into use in another software package.)

In order, we will cover:

1. Creation of a model geometry.
2. Defining physics/governing equations, boundary, and initial conditions.
3. Discretize/mesh the geometry.
4. Solver configuration.
5. Post-process the results.

## 2.4 Geometry Generation

Designing a good model geometry is critical as it can save significant computational resources. When designing a geometry the FEM user should try to represent the model geometry as accurately as possible while:

1. Avoid unnecessarily fine details; these may require an excessively fine mesh to resolve.
2. Leverage symmetry to reduce the domain size over which solution must be effected, and thereby the mesh can be made finer in a smaller portion of the domain.

Achieving these goals is not always straightforward, and success depends on the skill of the modeler and on the available tools. Typically a model geometry is constructed in some computer assisted design (CAD) software, and the particular tools available in these packages vary. While not absolutely necessary, the use of a CAD package outside of the COMSOL solver might sometimes make development of the domain description easier.

COMSOL has a built-in geometry generation tool, which allows the construction of advanced geometries by performing various operations on simpler geometries, e.g. a cylinder

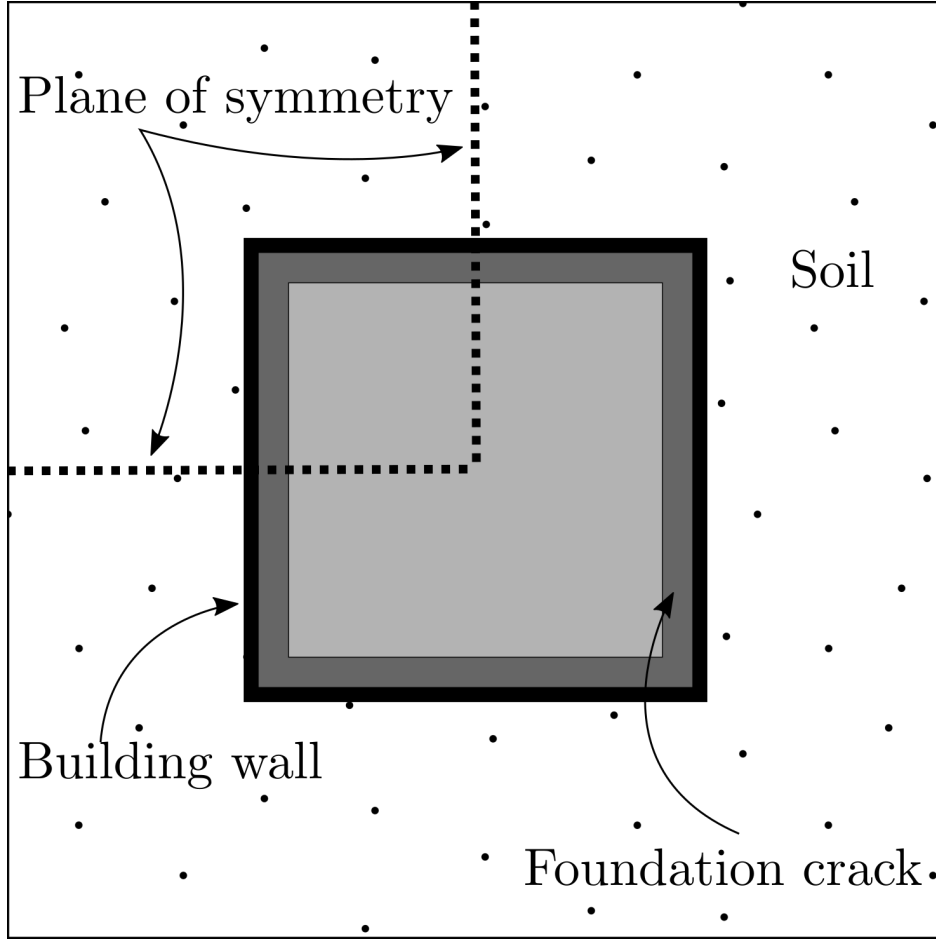


Figure 2.4: Birds-eye view of the VI scenario, showing the foundation and the breach, building wall, as well as the plane of symmetry that allows only a quarter of the total domain to be generated.

and half sphere can be combined to make a rivet. But as noted, it is also possible to import pre-generated geometries from other CAD software. For present illustrative purposes, we will create our own geometry.

The interior of the house itself will not be explicitly modeled, instead we only consider the soil surrounding the house. This is done for the simple reason that it is not important to model the interior of the house. Once the contaminant is in the structure, the damage, so to speak, has been done. We are interested in how fast the contaminant enters from the soil, which is what determines indoor contaminant concentration. In addition, typical building interiors are simply too heterogenous to generalize in any meaningful way. Trying

to explicitly model the interior so as to offer insights into indoor concentration variations while at the same time modeling the necessary subsurface transport, would be prohibitively expensive. Instead the interior is implicitly modeled as a CSTR and simply coupled with the explicit soil and foundation geometry via the foundation crack boundary.

One of the nice properties of the described VI scenario is that, due to symmetry, we only need to explicitly model a quarter of it (see Figure 2.4). This reduces the number of required mesh points by 75%, which is a huge computational saving. To create the specified geometry, see the instructions for geometry generation in the appendix.

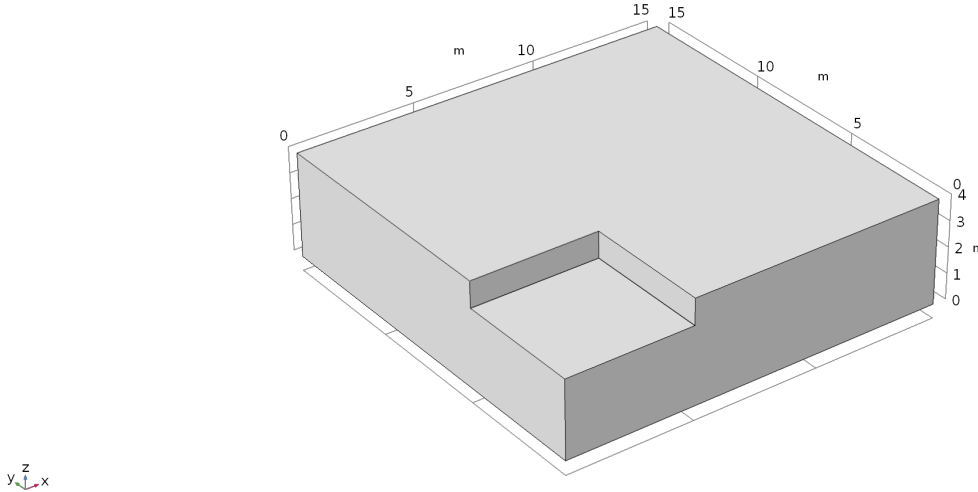


Figure 2.5: The complete geometry of the VI scenario as implemented in COMSOL.

## 2.5 Vapor Intrusion Physics and Governing Equations

Throughout this section the books *Contaminant hydrogeology*[41] by Fetter, and *Dynamics of fluids in porous media*[42] by Bear are used as sources, especially on topics regarding soil physics and contaminant transport in soils. The COMSOL reference manuals[43, 44] are also used as sources.

### 2.5.1 The Indoor Environment

The impacts on the indoor air space is perhaps the most important part of modeling VI, as the goal of these models ultimately is to predict indoor exposure given some external factors. The indoor environment is, however, only modeled implicitly as a continuously stirred tank reactor (CSTR). We assume that all contaminant entry into the house occurs via a foundation crack. It has been shown in other modeling work that results are not overly sensitive to the nature and position of the actual foundation breach[37], so we do not need to be overly concerned about the nature of the crack - the key feature is the overall area that it presents for contaminant entry. Once the contaminant enters the interior, it is instantly perfectly mixed, which is a key assumption of a CSTR. Contaminant expulsion occurs via air exchange with the outdoor environment, and is regulated by *air exchange rate*  $A_e$ , which dictates what fraction of the indoor air is exchanged with outdoor air over a given period of time. For instance, a common air exchange rate for a house is  $A_e = 0.5 \text{ h}^{-1}$ , i.e. half of the indoor air is exchanged every hour. The impacts of air exchange rate will be explored in Chapter 3.

It should be noted that in this simple VI model implementation, we assume that there are no indoor sources nor that any sorption of contaminant to/from any indoor materials occurs. Thus, the reaction term that would ordinarily be part of a CSTR is dropped (but is reintroduced in Chapter 5) and the temporal change in indoor contaminant concentration is thus given by (5.29).

$$V_{\text{bldg}} \frac{\partial c_{\text{in}}}{\partial t} = n_{\text{ck}} - V_{\text{bldg}} A_e c_{\text{in}} \quad (2.3)$$

Here  $c_{\text{in}}$  [ $\text{mol m}^{-3}$ ] is the indoor air contaminant concentration;  $n_{\text{ck}}$  [ $\text{mol s}^{-1}$ ] is the contaminant entry (or exit) rate into the building via the foundation crack;  $A_e = 0.5 \text{ h}^{-1}$  is the air exchange rate; Finally,  $V_{\text{bldg}} = 300 \text{ m}^3$  is the volume of the house interior (or basement in this case).

A limitation of this approach is that we only consider one control volume or compart-

ment, while in reality indoor contaminant concentrations can vary significantly between compartments, in particular between different floors. There are VI models that use multiple compartments, which in essence are just coupled CSTRs[45]. Basements typically have higher indoor contaminant concentrations than other floors, so in this implementation we assume that our sole compartment is the house basement, which  $V_{\text{bldg}} = 300 \text{ m}^3$  reflects.

Solving (5.29) requires us to determine the contaminant entry and air exchange rates. Air exchange rates can vary quite significantly, and are a significant source of temporal variability in VI, a topic that will be further explored in Chapter 3. However, they typically vary around relatively well-known values as air exchange rates are regulated in building codes. For residential buildings, it is typical that air exchange rate is around  $A_e = 0.5 \text{ h}^{-1}$  and thus for simplicity we will choose this value.

**Contaminant entry into the building** Contaminant entry rates are significantly more difficult to determine, as they depend on air velocity through the foundation breach and the concentration gradient across it. The determination of these is the main point, and challenge in VI modeling.

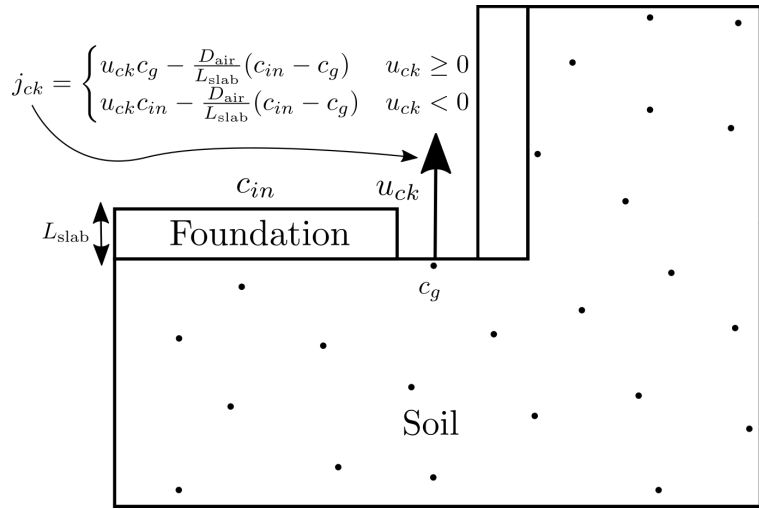


Figure 2.6: Soil-gas contaminant vapors are transported from the underlying soil into a building via a breach in the foundation. The scale is exaggerated, and in our modeled scenario the crack is only 1 cm wide.

The contaminant entry  $n_{ck}$  is given by integrating the contaminant entry flux  $j_{ck}$  across

the foundation crack boundary  $A_{ck}$ .

$$n_{ck} = \int_{A_{ck}} j_{ck} dA \quad (2.4)$$

The contaminant flux through the foundation crack is modeled as transport between two parallel plates and has an advective and a diffusive component.

$$j_{ck} = j_{\text{advection}} + j_{\text{diffusion}} \quad (2.5)$$

Since contaminant concentration indoors is lower than it is in the soil or near foundation crack region a concentration gradient from the soil-gas to the indoor will exist. The interior of the crack is not explicitly modeled, but assumed to only contain air and thus we assume the diffusion coefficient is the same as in air.

$$j_{\text{diffusion}} = -\frac{D_{\text{air}}}{L_{\text{slab}}} (c_{in} - c_g) \quad (2.6)$$

here  $D_{\text{air}} = 7.2 \times 10^{-6} \text{ m}^2 \text{ s}^{-1}$  is the diffusion coefficient of TCE in air as a sample contaminant of interest; other contaminant of common concern have comparable diffusivities.  $L_{\text{slab}} = 15 \text{ cm}$  is a typical thickness of a foundation slab;  $c_{in}$  [ $\text{mol m}^{-3}$ ] is the indoor contaminant concentration;  $c_g$  [ $\text{mol m}^{-3}$ ] is the contaminant gas-phase concentration at the foundation crack boundary.

Advective transport through the slab can occur in both directions, i.e. contaminants can be carried from the soil into the house and from the house into the soil[16]. The direction of this transport depend on the direction of the flow, with a positive sign indicating that airflow goes into the house.

$$j_{\text{advection}} = \begin{cases} u_{ck} c_g & u_{ck} \geq 0 \\ u_{ck} c_{in} & u_{ck} < 0 \end{cases} \quad (2.7)$$

here  $u_{ck}$  [ $\text{m s}^{-1}$ ] is the airflow velocity through the foundation crack.

Thus the total contaminant transport through the foundation crack is given by (5.11).

$$j_{ck} = \begin{cases} u_{ck}c_g - \frac{D_{\text{air}}}{L_{\text{slab}}}(c_{in} - c_g) & u_{ck} \geq 0 \\ u_{ck}c_{in} - \frac{D_{\text{air}}}{L_{\text{slab}}}(c_{in} - c_g) & u_{ck} < 0 \end{cases} \quad (2.8)$$

(See Figure 2.6.) Not only will (5.11) be used to calculate the contaminant entry rate into house, but it is a necessary boundary condition for calculating the contaminant concentration in the soil. However, as we see, (5.11) is a function of both the soil-gas concentration at the foundation crack boundary  $c_g$  and the indoor contaminant concentration  $c_{in}$ , thus these two are coupled and need to be solved simultaneously.

### 2.5.2 The Importance Of Soil Moisture Content

The portion of soil between groundwater and ground surface is variably saturated with water and is called the vadose zone. Under environmental conditions, TCE and many other contaminants are miscible in water, and will be partitioned between water and vapor phases, which has profound effects on the total contaminant transport in the vadose zone. The rates of diffusion in liquids and gases usually differ by orders of magnitudes. Likewise, advective transport in the two phases occurs at vastly different rates, and as such it is important to account for the effects of soil moisture content on transport of contaminant.

Water filling of soil pores from the groundwater surface is driven by a negative pressure gradient induced by surface tension, called capillary potential and is here represented by  $\psi$ . This capillary potential is a function of the soil moisture content, and becomes increasingly negative as the water content decreases, and is zero when the soil matrix is saturated with water. The capillary potential varies with the hydraulic properties of specific soil types.

In addition to the capillary potential, soil moisture content is driven by a gravitational potential, e.g. induced groundwater flow due to some elevation gradient. The total soil

moisture potential  $\phi$ , is the sum of the capillary and gravitational potentials, here expressed as a pressure head.

$$\phi = \frac{\psi(\theta_w)}{\rho g} + h_g = h + h_g \quad (2.9)$$

where  $\phi$  [m] is the total soil moisture potential;  $\psi$  [Pa] is the capillary potential;  $h$  [m] is the capillary potential expressed as a pressure head above the groundwater/soil interface;  $\theta_w$  is the volumetric moisture content by volume soil, i.e. dimensionless;  $\rho$  [ $\text{kg m}^{-3}$ ] is the density of water;  $g$  [ $\text{m s}^{-2}$ ] is the acceleration due to gravity; and  $h_g$  [m] is the gravitational potential above a reference plane.

In the VI scenario considered here, we assume that the groundwater is at steady-state and its soil interface is flat<sup>1</sup>. Thus, the soil moisture content is entirely determined by the capillary potential  $h$ .

There are two common methods for modeling the capillary potential, one developed by Brooks and Corey[46] in 1966, and another by van Genuchten[47] in 1980. Both of these are semi-empirical approaches and relies on experimentally determined parameters for a specific soil type to be used. In this work, we only use van Genuchten's method, simply because parameters for a wide variety of soils have been made available by the EPA (Table B.1).

### van Genuchten's Soil-Water Retention Model

The relationship between capillary pressure and moisture content is called *soil moisture retention*, and is what van Genuchten's method describes. Specifically, his method models the water saturation of the soil and is given by (5.1).

$$Se = \begin{cases} \frac{1}{(1+(\alpha|h|)^n)^m} & h < 0 \\ 1 & h \geq 0 \end{cases} \quad (2.10)$$

---

<sup>1</sup>If these assumptions cannot be made and one wishes to model the groundwater and vadose zones as a continuum, the soil moisture content is determined by Richard's equation.

here  $Se$  is the saturation, which ranges from 0 to 1, where 1 is fully saturated with water;  $\alpha$ ,  $m$ , and  $n = \frac{1}{1-m}$  are the empirically determined van Genuchten parameters given in Table B.1; and  $h$  [m] is the capillary pressure head as elevation above the groundwater/soil interface.

It is important to note that  $Se = 0$  does not mean that there is no moisture in the soil; soils retain a small amount of water in the matrix - residual moisture content (which is soil specific). Thus, the soil moisture content is given by (5.2)

$$\theta_w = \begin{cases} \theta_r + Se(\theta_t - \theta_r) & h < 0 \\ \theta_t & h \geq 0 \end{cases} \quad (2.11)$$

where  $\theta_w$  is the volumetric soil moisture content;  $\theta_t$  is the soil porosity; and  $\theta_r$  is the residual moisture content.

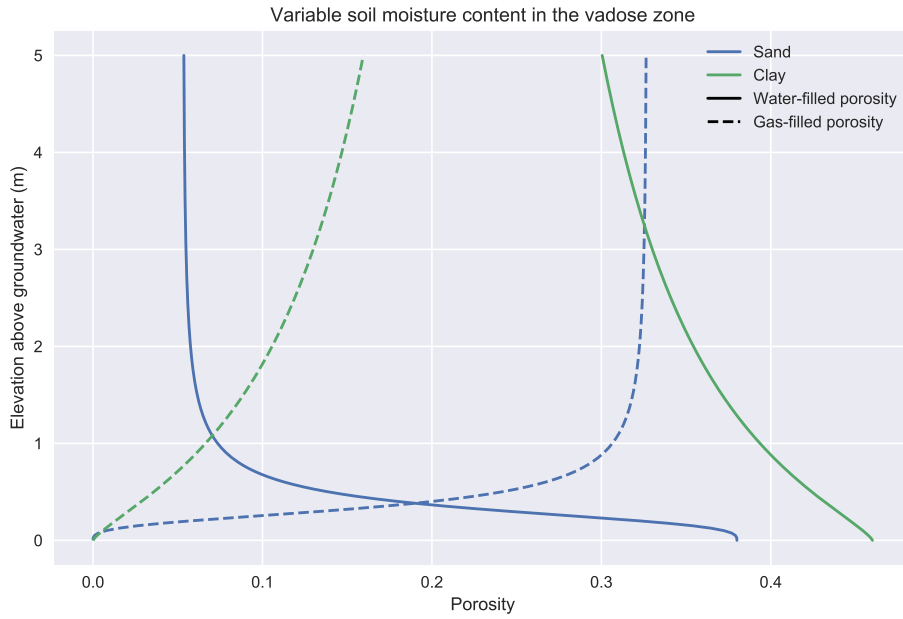
By extension, the soil gas or air content is given by

$$\theta_g = \theta_t - \theta_w \quad (2.12)$$

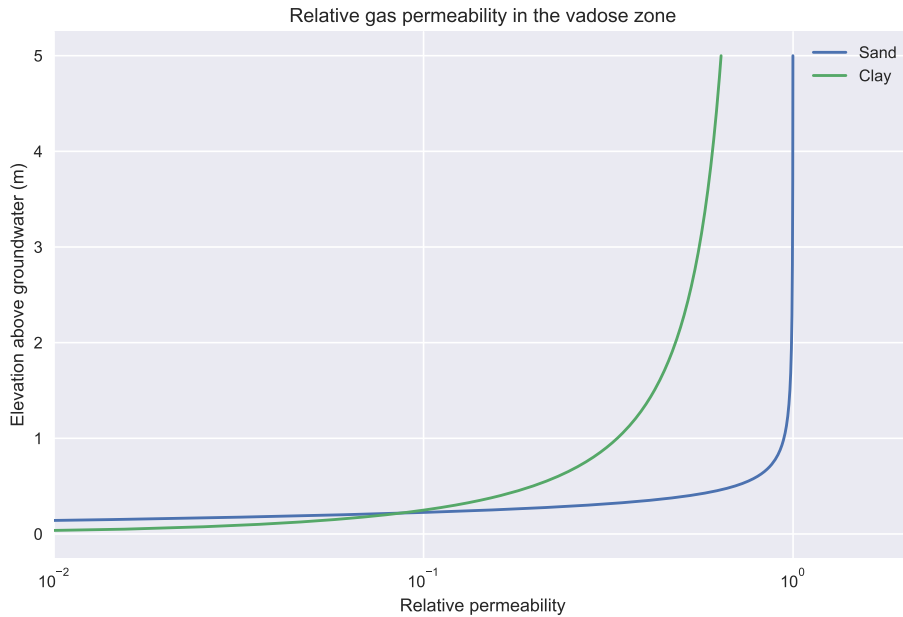
An example of the soil saturation and moisture content as a function of height above groundwater is shown in Figure 2.7a. Note the steep decline in moisture content near the groundwater interface - that is the capillary zone and we will see that this zone presents a significant barrier to contaminant transport from the groundwater in section 2.5.4.

The presence of water in the soil matrix has profound implications for transport as the pore space available for transport may be restricted. For instance, in the capillary zone, contaminant transport is mostly limited by the water phase, while gas phase transport is extremely limited because air-filled porosity is limited and largely isolated. The opposite is true near the ground surface, where most of the pore space is filled with air.

Soil already limits transport, i.e. it is harder to pump water through a soil column than a pipe of the same diameter. This extra phase-specific transport inhibition is modeled by a



(a) Example of a soil moisture retention curve as a function of pressure head above the groundwater/soil interface.



(b) Relative air and water permeability in the vadose zone or above the groundwater interface.

Figure 2.7: The van Genuchten soil moisture retention curve and relative permeability of soil to air and water transport.

*relative permeability* and is given by (5.3).

$$k_r = \begin{cases} (1 - Se)^l (1 - Se^{\frac{1}{m}})^{2m} & h < 0 \\ 0 & h \geq 0 \end{cases} \quad (2.13)$$

here  $k_r$  is the relative permeability for air; and  $l = 0.5$  is another van Genuchten parameter.

The relative permeability varies from 0 to 1, where 0 indicates that the soil matrix is completely impermeable to the fluid, while a value of 1 means that there is no additional permeability cost. Figure 2.7b shows how the relative gas permeability varies in the vadose zone.

### 2.5.3 Airflow In The Vadose Zone

In our VI scenario, the depressurized house induces an advective airflow from the ground surface, through the vadose zone, and into the house via a foundation crack, this flow carries contaminant vapors with it. This airflow is modeled using a modified version of Darcy's Law. The modification is made to account for the variable moisture content in the vadose zone, which is discussed in section 5.3.2.

Darcy's Law describes the flow of a fluid through a porous medium. This flow is typically driven by a pressure gradient, and its magnitude depends on the permeability of the porous medium and the fluid's viscosity.

$$\vec{u} = -\frac{\kappa}{\mu} \nabla p \quad (2.14)$$

here  $\vec{u}$  [ $\text{m s}^{-1}$ ] is the airflow velocity vector;  $\kappa$  [ $\text{m}^2$ ] is the permeability of the porous medium;  $\mu$  [ $\text{Pa s}$ ] is the dynamic viscosity of the fluid; and  $\nabla p$  [ $\text{Pa m}^{-1}$ ] is the pressure gradient.

This (2.14) formulation of Darcy's Law assumes that the porous medium is saturated with the transporting fluid,<sup>2</sup> hence the need to modify this expression when there are two fluid phases present. While porosity is not directly part of (2.14), it is an intrinsic property that determines the permeability  $\kappa$  of the porous medium; the degree of saturation in pores determines the air permeability. This variation in permeability is modeled using the relative permeability expression from van Genuchten's equation (5.3). The effective soil permeability is the product of the saturated soil permeability and its relative permeability giving our

---

<sup>2</sup>Darcy's Law also assumes that the flow is in the laminar regime, i.e. the Reynolds number  $\text{Re} < 1$ . Due to the small pressure gradients in most VI scenarios, this assumption is rarely unfulfilled, but if it is, then Brinkman's equation should be used instead.

modified Darcy's Law (2.15).

$$\vec{u} = -\frac{k_r \kappa}{\mu} \nabla p \quad (2.15)$$

Recall that by definition  $k_r$  is the relative permeability of the soil to *air*, and thus  $k_r \kappa$  form an effective permeability.

To calculate the soil-gas velocity field in the vadose zone, we need a continuity equation, which for fluid flow is (2.16).

$$\frac{\partial \rho}{\partial t} + \nabla \cdot (\rho \vec{u}) = 0 \quad (2.16)$$

Inserting our modified Darcy's Law for the velocity gives (2.17).

$$\frac{\partial}{\partial t}(\rho \theta_g) + \nabla \cdot \rho \left( -\frac{(1 - k_r) \kappa}{\mu} \nabla p \right) = 0 \quad (2.17)$$

where  $\theta_g$  is the gas-filled porosity of the soil from (2.12);  $\rho = 1.225 \text{ kg m}^{-3}$  is the density of air; and  $\mu = 18.5 \times 10^{-6} \text{ Pas}$  is the dynamic viscosity of air. Contaminant vapor concentrations are typically very low in VI scenarios, and therefore we assume that the contaminant does not affect the transport properties of air.

In order to solve (2.17) we need to define some boundary conditions. In our VI scenario, air is pulled from the atmosphere through the ground surface and into the building via the foundation crack. To model this only three boundary conditions are required. We also need to choose a basis function, and we use the COMSOL recommended "hat" here, which will be used to determine the pressure  $p$  throughout the modeled domain.

**Boundary Conditions** The first boundary condition defines a pressure gauge, i.e. a reference point for where the pressure is zero, and is where air will be pulled from. This is applied to the ground surface boundary. The second is that we apply the indoor/outdoor pressure difference (-5 Pa) to the foundation crack boundary, assuming that the indoor air pressure exists at the crack entrance at the soil interface. The third type of boundary condition is applied to all remaining boundaries and is a no flow boundary condition, indicating that

no flow passes through these boundaries. This also applies to the symmetry planes present recalling that we are solving over only a quarter domain.

$$\text{Ground surface} \quad p = 0 \text{ Pa} \quad (2.18)$$

$$\text{Foundation crack} \quad p = p_{\text{in/out}} = -5 \text{ Pa} \quad (2.19)$$

$$\text{Remaining} \quad -\vec{n} \cdot \rho \vec{u} = 0 \quad (2.20)$$

where  $\vec{n}$  is the boundary normal vector.

**Initial Conditions** For steady-state problems, initial conditions are not needed. Transient simulations however, require initial conditions and these are typically assumed to be given by some steady-state solution that exists before a transient disruption.

#### 2.5.4 Mass Transport In The Vadose Zone

To begin deriving a governing equation for contaminant transport in our VI scenario, we consider the continuity equation which states that the change of concentration in some volume of space depends on the advective and diffusive fluxes in and out of the system, as well as any generation or consumption inside the system.

$$\frac{\partial c}{\partial t} + \nabla \cdot (j_{\text{adv}} + j_{\text{diff}}) - G = 0 \quad (2.21)$$

here  $c$  [ $\text{mol m}^{-3}$ ] is the concentration of the chemical species;  $t$  [s] is time;  $j_{\text{adv}}$  and  $j_{\text{diff}}$  [ $\text{mol s}^{-1} \text{m}^{-2}$ ] are the advective and diffusive fluxes respectively; and  $G$  [ $\text{mol s}^{-1}$ ] is the generation or consumption of the chemical species.

In our model we will assume that  $G = 0$  as the groundwater is the sole contaminant source, i.e. there are no other sources of TCE in the soil, and TCE also does not readily degrade in soils<sup>3</sup>. However, this term should be retained and an appropriate expression

---

<sup>3</sup>Although, it is possible to introduce certain bacteria to bioremediate TCE in soils, but this typically

developed if one wants to model:

- Biodegradation of some compound in the soil.
- Radon intrusion (remember radon gas is generated throughout soils and rocks).
- A soil or subsurface source, e.g. a leaky tank or evaporation from a liquid contaminant spill.

The advective flux is given by

$$j_{\text{adv}} = \vec{u}c \quad (2.22)$$

where  $\vec{u}$  [ $\text{m s}^{-1}$ ] is a velocity vector. The diffusive flux is given by Fick's Law

$$j_{\text{diff}} = -D\nabla c \quad (2.23)$$

where  $D$  [ $\text{m}^2 \text{s}^{-1}$ ] is the diffusion coefficient of the contaminant in the soil air; and  $\nabla c$  [ $\text{mol m}^{-3} \text{m}^{-1}$ ] is a concentration gradient. Thus we get the advection-diffusion equation which generally governs transport of a chemical species

$$\frac{\partial c}{\partial t} + \nabla \cdot (\vec{u}c + -D\nabla c) = 0 \quad (2.24)$$

However, this simple gas phase transport equation will not accurately represent contaminant transport in the vadose zone if:

- Contaminant transport occurs inside a variably saturated porous matrix which significantly affect transport properties.
- The contaminant concentration in the vadose zone is distributed between three phases - gas, water, and solid (via sorption).

---

requires specific conditions, which generally are not naturally met. Under these specific conditions TCE may be biodegraded by some bacteria[48, 49]

The total contaminant concentration in the soil is given by the sum of the gas, water, and solid phase concentrations at any given point in the soil.

$$c_T = \theta_w c_w + \theta_g c_g + c_s \rho_b \quad (2.25)$$

Here  $\theta_g$  and  $\theta_w$  are the gas-filled and water-filled porosities respectively;  $c_T$  [ $\text{mol m}^{-3}$ ] is the total soil contaminant concentration;  $c_w$  and  $c_g$  [ $\text{mol m}^{-3}$ ] are the contaminant concentrations in water and gas respectively;  $c_s$  [ $\text{mol kg}^{-1}$ ] is the solid phase or sorbed concentration per mass of soil; and  $\rho_b = (1 - \theta_t) \rho$  [ $\text{kg m}^{-3}$ ] is the bulk density of the soil, which can be calculated from the soil porosity  $\theta_t$  and solid phase density of the soil  $\rho$  [ $\text{kg m}^{-3}$ ].

The attentive reader will now notice that (2.24) depends on three variables instead of one. However, remember that we're concerned with low contaminant concentrations, we can relate the gas and liquid phase concentrations via Henry's Law (5.8)

$$c_g = K_H c_w \quad (2.26)$$

where, for example  $K_H = 0.402$  is the dimensionless Henry's Law constant for TCE at  $20^\circ\text{C}$ [50]. We also assume that there are no temperature gradients throughout the vadose zone.

The solid phase concentration can be related to the others via a linear sorption isotherm. Here either the gas-solid or water-solid sorption interaction can be chosen; the former is used in Chapter 5 where we will explore the effects of gas-solid sorption.

$$c_s = \begin{cases} K_p c_w & \text{Water-solid sorption} \\ K_p c_g = K_p K_H c_w & \text{Gas-solid sorption} \end{cases} \quad (2.27)$$

here  $K_p$  [ $\text{m}^3 \text{kg}^{-1}$ ] is a sorption partitioning coefficient.

Another approach is to simply ignore the role of sorption completely, i.e.  $K_p = 0$ , which

has historically been done in VI modeling and is done in the following parts of this example too. The reason for this is two-fold.

1. Relevant soil sorption data have not been readily available.
2. At steady-state, sorption doesn't affect the solution; the fact that there is TCE sorbed to soil particles does not influence the vapor transport at steady state, since equilibrium is assumed to have been established prior to the steady-state analysis. This has been a common assumption in most VI modeling studies, which have mostly focused on steady-state.

Regardless, we will continue carrying the sorption  $K_p$  term, because this will become relevant in Chapter 5 where experimentally derived relevant sorption data are available, and in which the role of this sorption process is considered in the context of transient models.

Using Henry's Law and the linear sorption assumptions we can relate the total contaminant concentration at any point in the soil matrix to the water-phase contaminant concentration at that point, from which the air phase and solid phase concentrations may be immediately calculated. The focus on water concentration is arbitrary, but commonly used.

$$c_T = (\theta_w + \theta_g K_H + K_H K_p \rho_b) c_w \quad (2.28)$$

The terms in front of  $c_w$  are collected as  $R = (\theta_w + \theta_g K_H + K_H K_p \rho_b)$ . This term is called the *retardation factor* and reflects the potentially increased contaminant residence time in the matrix due to transferring between the phases. Again, this only becomes an important factor in transient transport simulations.

In the vadose zone, advective transport can occur in both the water and gas phases inside the soil pores.

$$j_{\text{adv}} = \vec{u}_{w,\text{pore}} c_w \theta_w + \vec{u}_{g,\text{pore}} c_g \theta_g \quad (2.29)$$

here  $\vec{u}_{w,\text{pore}}$  and  $\vec{u}_{g,\text{pore}}$  [ $\text{m s}^{-1}$ ] are the water and gas phase pore velocities vectors respectively. However, from mass conservation, we know that the product of the pore velocity and porosity

gives the superficial velocity of a fluid in porous media, i.e. the Darcy's Law velocities. This together with Henry's Law gives

$$j_{\text{adv}} = (\vec{u}_w + \vec{u}_g K_H) c_w \quad (2.30)$$

and here  $\vec{u}_w$  and  $\vec{u}_g$  [ $\text{m s}^{-1}$ ] are the Darcy or superficial velocity vectors.

In section 5.3.2 we assumed that soil-water is stationary, i.e.  $\vec{u}_w = 0$  giving

$$j_{\text{adv}} = \vec{u}_g K_H c_w \quad (2.31)$$

where  $\vec{u}_g$  is the solution obtained from solving Darcy's Law in section 2.5.3.

To model a scenario where there is a gravitational water potential resulting in ground-water flow, one would have to solve two-phase Darcy's Law to get both  $\vec{u}_g$  and  $\vec{u}_w$ . This significantly complicates the mass transport aspect as well, and as such is beyond the scope of this work. This rarely contributes much to understanding VI and the rates of groundwater movement are typically too slow to be of much consequence.

The diffusive transport expression likewise needs to be adjusted for multiphase systems, and the total diffusive flux through the pore matrix is given by

$$j_{\text{diff}} = -(D_w \theta_w \tau_w \nabla c_w + D_g \theta_g \tau_g \nabla c_g) \quad (2.32)$$

here  $D_w = 1.02 \times 10^{-9} \text{ m}^2 \text{s}^{-1}$  and  $D_g = 6.87 \times 10^{-6} \text{ m}^2 \text{s}^{-1}$  are the contaminant diffusion coefficients of TCE in pure water and air respectively; and  $\tau_w$  and  $\tau_g$  are the water and gas tortuosity terms, reflecting the fact that in a granular bed, the flow does not occur in a straight line direction.

Due to the irregular shapes of pores, diffusion of a chemical species will inevitably often occur along a tortuous path, which the tortuosity terms attempt to capture. As tortuosity depends on the structure of the porous matrix, it is difficult to accurately portray, but a

popular approach is to use the Millington and Quirks model[51].

$$\tau_w = \frac{\theta_w^{\frac{7}{3}}}{\theta_t^2}, \quad \tau_g = \frac{\theta_g^{\frac{7}{3}}}{\theta_t^2} \quad (2.33)$$

here  $\theta_t$  is the total or saturated porosity of the soil matrix. Another popular approach is Bruggeman's model.

Combining (5.13) and (5.8) in our diffusion flux expression gives

$$j_{\text{diff}} = - \left( D_w \frac{\theta_w^{\frac{10}{3}}}{\theta_t^2} + D_g \frac{\theta_g^{\frac{10}{3}}}{\theta_t^2} K_H \right) \nabla c_w \quad (2.34)$$

the terms in front of  $\nabla c_w$  can be collected as an effective diffusion coefficient  $D_{\text{eff}}$  [ $\text{m}^2 \text{s}^{-1}$ ], which with our isothermal vadose zone assumption only depends on the soil moisture content. Thus we get the final diffusive flux expression

$$j_{\text{diff}} = -D_{\text{eff}} \nabla c_w \quad (2.35)$$

Figure 2.8 shows how the effective diffusivity varies from being close to that of the pure water diffusivity near the capillary zone, and increases to something closer to gas-phase diffusivity as the soil moisture decreases.

Putting all this together finally gives us the governing equation for contaminant transport in the vadose zone for our modeled VI scenario.

$$R \frac{\partial c_w}{\partial t} = \nabla \cdot (D_{\text{eff}} \nabla c_w) - K_H \vec{u}_g \cdot \nabla c_w \quad (2.36)$$

To solve this we need to define some boundary and initial conditions. We also need to choose a basis function which is used to determine the contaminant concentration throughout the domain, and we use the COMSOL recommended second order polynomial here.

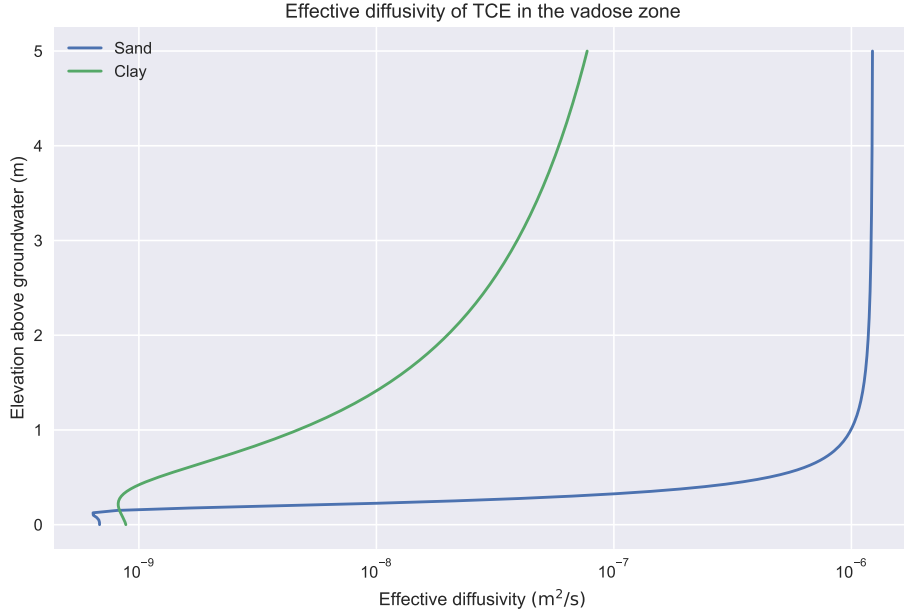


Figure 2.8: Effective diffusivity of TCE in the vadose zone using the Millington-Quirk model. Soil water and gas filled porosites are calculated using van Genuchten's equations.

**Boundary Conditions** In this VI scenario, the sole contaminant source is assumed to be the homogenously contaminated groundwater, which we assume to have a fixed concentration. The atmosphere acts as a contaminant sink and thus this is simply a zero concentration boundary condition. Contaminants leave the soil domain and enter the building through a combination of advective and diffusive gas phase transport. The boundary condition applied to all other boundaries is a no-flow boundary.

$$\text{Atmosphere} \quad c_w = 0 \text{ mol m}^{-3} \quad (2.37)$$

$$\text{Groundwater} \quad c_w = c_{gw} = 50 \mu\text{mol m}^{-3} \quad (2.38)$$

$$\text{Foundation crack} \quad -\vec{n} \cdot \vec{N} = -j_{ck} \text{ mol m}^{-2} \text{ s}^{-1} \quad (2.39)$$

$$\text{All other} \quad -\vec{n} \cdot \vec{N} = 0 \text{ mol m}^{-2} \text{ s}^{-1} \quad (2.40)$$

$\vec{n} \cdot \vec{N}$  is the dot product between the boundary normal vector and the contaminant flux;  $j_{ck}$  [ $\text{mol m}^{-2} \text{ s}^{-1}$ ] is the contaminant flux into the building from section 2.5.1.

**Initial Conditions** For steady-state problems, the initial conditions do not enter. Transient simulations however, require initial conditions and these are assumed to be given by the steady-state solution.

## 2.6 Meshing

The mesh in FEM model is the collection of small discrete elements that make up the model geometry or domain. Meshing is the process of generating a mesh. Meshing is one of the most important aspects of FEM modeling as the mesh directly influences the accuracy of the solution; it is important that the various gradients are resolved by the mesh. However, designing a good mesh can be challenging as a finer mesh has a higher computational cost. A good mesh designer must constantly balance accuracy and computational costs by considering where a mesh can be finer and where it can be coarser.

The most fundamental unit of the mesh is the element(s) that comprise the mesh. There are many different types of elements that can be used for meshing and choosing which ones to use depend primarily on the spatial dimensionality of the model, the particularities of the geometry, and the physics that we wish to model. Obviously different element types are by necessity needed to model a 2D vs. 3D geometry; you cannot mesh a 3D geometry with 2D squares.

There are primarily four types of 3D mesh elements available - the tetrahedral, cuboid, prism, and pyramid. Figure 2.9 shows some common mesh elements. These can be combined in various ways to represent any 3D geometry. The most general 3D element is the tetrahedral and will approximate any geometry well. However, it is not always the most effective choice for meshing a geometry and another element type may be better suited. This is easiest illustrated with an example.

Imagine that you are trying to simulate the laminar flow of some fluid in a pipe. Because of symmetry, only a wedge of the pipe needs to be explicitly modeled. Therefore, in this

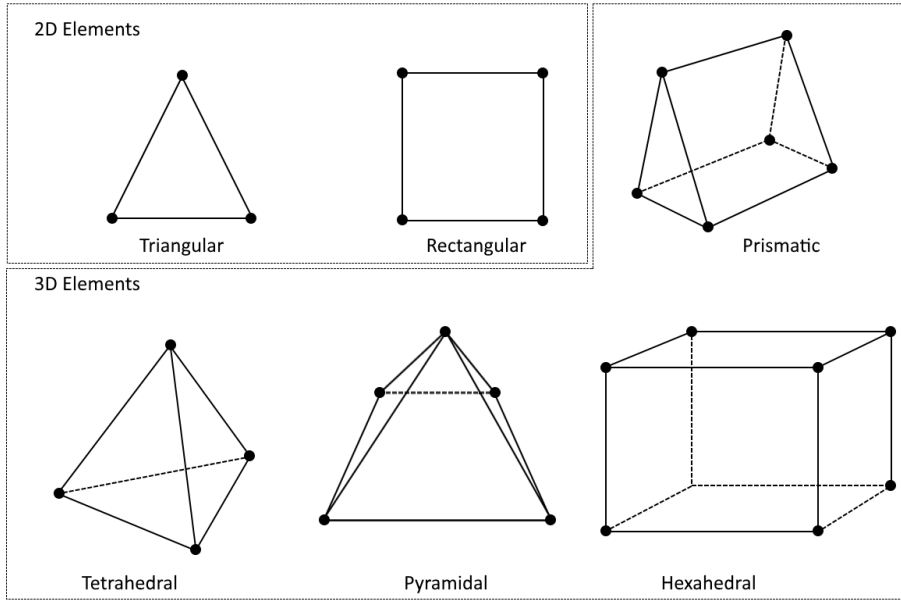


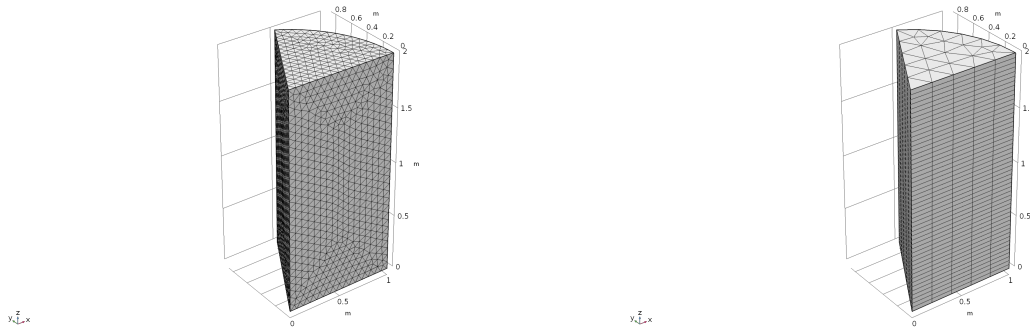
Figure 2.9: Some common mesh elements. Figure from COMSOL[40].

scenario, it might be beneficial to use prism elements rather than tetrahedrals, since these are already wedge shaped.

The laminar pipe flow will have a gradient in the direction of the flow. Thus the mesh mostly only needs to be fine in the flow direction, while the mesh can be coarser in the radial direction. Constructing a mesh on this basis would allow us to achieve a solution of high accuracy while still keeping the number of elements relatively small - all through clever mesh design (see Figure 2.10).

This is of course a relatively simple example and more complicated geometries may need all kinds of element for constructing a clever design. These type of multi-element meshes can give significant computational saving but at the expense of often requiring significant user input to be generated. Sticking to one type of elements is often simpler as these can quickly and easily mesh geometries.

Meshing can be done manually, but is often performed by a meshing algorithm. The creation of these algorithms is a science in itself, but their use often involve passing some basic parameters to the algorithm. Here the user could, for instance, specify the maximum



(a) Mesh using tetrahedrals. 50,197 elements. (b) Mesh using prism elements. 1900 elements.

Figure 2.10: By understanding the physics, here considering laminar flow in a pipe (segment), clever mesh design can significantly reduce the number of mesh elements. Notice that the mesh density in the axial direction is more or less the same.

and minimum element sizes, maximum element growth rate, how finely small features or curves (typically quite difficult to mesh) should be meshed. These instructions can be specific to various parts of the model, e.g. much finer meshing resolution can be specified for an area of interest and vice versa. There are also a variety of specialty mesh features such as a mesh boundary layer available: adding finely spaced mesh layers along a boundary. How to use all of these tools effectively to mesh a geometry is why meshing can be one of the most challenging aspects of FEM modeling.

### 2.6.1 Meshing The VI Model

The first choice we need to make is which type of element to use, and in order to do that we need to think about the gradients of the dependent variables.

From van Genuchten's retention curves, we know there will be a large soil moisture gradient in the capillary zone, which will need a relatively fine mesh to be resolved. The airflow from Darcy's Law will form some sort of arcing streamline from the ground surface to the foundation crack; the pressure gradient will be inline with these streamline. The concentration gradient is difficult to predict a priori, but there likely will be some gradient from the groundwater to the ground surface and foundation crack. Since many of these

gradients intersect and go in different directions from each other it makes sense to use tetrahedral elements to mesh the geometry; these are the more general 3D elements.

Properly meshing our geometry can be a challenge due to the great range of geometric scale. The house and soil domains are on the order of meters while the foundation crack is only 1 cm side, and requires very fine meshing. This is not only due to its small size, but because the contaminant entry will be calculated based on the solution here, which largely determines the indoor contaminant concentration.

The COMSOL meshing algorithm only require a few parameters to relatively mesh a geometry with tetrahedrals. A description of each parameter and its value can be seen in Table 2.1.

Input	Value	Description
Maximum element size	1.5 m	Maximum size of a element
Minimum element size	1 mm	Minimum size of a element
Maximum element growth rate	1.3	Maximum allowed size increase of adjacent elements. 1.3 indicates that an element can only be 30% larger than its neighbor. A smaller value gives a finer mesh.
Curvature factor	0.4	Ratio between the boundary element size and the geometry curvature radius. A smaller value gives a finer mesh.
Resolution of narrow regions	1	Control the number of layers of elements that are created in narrow regions. A larger value gives a finer mesh.

Table 2.1: Inputs to COMSOLs meshing algorithm.

### 2.6.2 Boundary Layer Mesh

When posed with steep gradients in one particular direction at boundaries, as we have here, it is often useful to use a *boundary layer mesh* at the impacted boundaries. This is a type of mesh that introduces a dense layer of meshes along the normal direction from a boundary. Boundary layer meshes are common features in meshing algorithms, and COMSOL's is no exception.

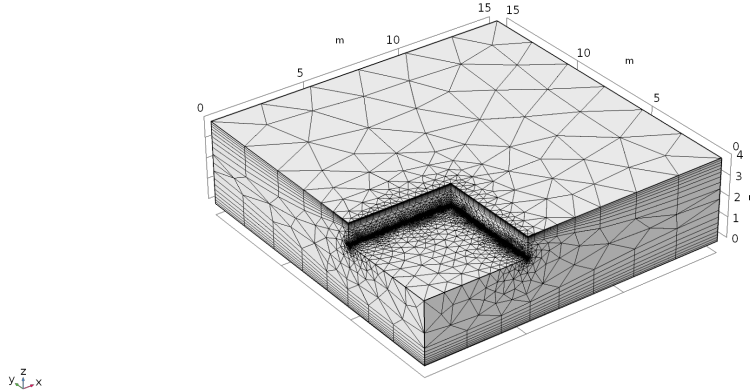
The number of boundary layers are supplied by the user, and in our case we will use 8 layers, but more could be added if needed. The distance between each layer is determined by the size of the other elements in its vicinity, as well as the distance growth rate between each layer, which we set to 1.3, i.e. the distance increases by 30% for each layer. Figure 2.11 shows our completed mesh.

## 2.7 Solver Configuration

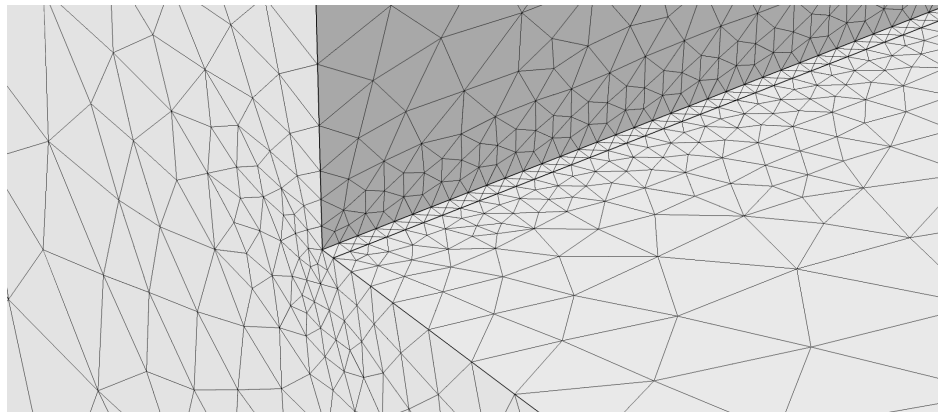
A solver(s) is required to solve the VI model, and a few considerations need to be taken into account when choosing one. For choosing and motivating a solver configuration, the *COMSOL Multiphysics Reference Manual v5.3a*[43] is here continuously used as a source.

For simplicity we will now first consider a stationary or steady-state problem. Since our model is a multiphysics problem, i.e. many of the physical parameters depend on each other, we first need consider how to couple them. They can be coupled by either using a *segregated* or *fully coupled* approach.

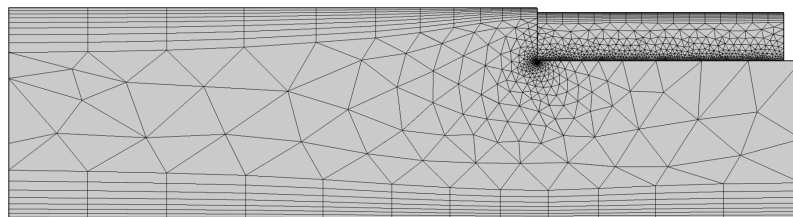
**Segregated vs. fully coupled physics** In a segregated solver, each governing equation is solved separately in a specific order. For instance, in our VI example we can solve Darcy's Law first, get some solution for airflow in soil, and then use that velocity field in the transport equation, solve that, and then solve the indoor concentration equation, i.e. we solve one system equation per step. These steps are simply iterated until convergence occurs in all of the separated steps. In the case of VI calculations, the use of the segregated approach is fully justified because the concentrations of contaminant vapors are normally so low that they have no impact on the solution of soil airflow using Darcy's Law. The fully coupled approach assembles a single large system of equations. Both of these approaches should reach the same solution, but the fully coupled approach will do so faster, but at the expense of using more memory.



(a) The darker perimeter around the foundation highlights the higher mesh density along the foundation crack.



(b) Close-up of the foundation crack mesh.



(c) Side-view highlighting the boundary layer mesh.

Figure 2.11: Initial finite element mesh of the modeled vapor intrusion scenario.

**Direct vs. iterative solver** Within each of these coupling approaches, we need to specify a solver to solve the system of equations. Here we are again faced with a choice, and we could either use a *direct* or *iterative* solver. Direct solvers, as the name implies, arrive at a solution

directly and are based on LU-decomposition. Iterative solvers on the other hand, iteratively approach the solution, and are based on conjugate gradient method. The advantage of direct solvers is that they are faster, but use more memory, while iterative solvers are slower but use less memory. In terms of choosing a solver algorithm, there are many options, but MUMPS and GMRES will be used as the respective algorithm for direct and iterative solvers.

**Time-dependent solvers** To solve a transient or time-dependent problem (which will be done in subsequent chapters) a solver to step forward in time is required. Too large a time step will cause stability issues and ultimately convergence will be impossible, but obviously some discrete time step is required for a solution to be achievable. A time-dependent solver picks an appropriate time-step and there are some popular approaches, such as using some high-order Runge-Kutta (RK) or backwards differentiation formula (BDF). Regardless of the type of solver, for each time step the system of equations will be solved using one of the aforementioned solvers. The difference between RK and BDF is that RK explicitly discretizes time while BDF does so implicitly. In this work we will only use BDF as it is more stable than RK.

**Choosing solvers** The choice of solver will not affect (or should not at least) the solution to the problem. However, it can have a large impact on computational time and resources, and these considerations dictate solver choice (this is also partially dependent on the mesh used, as this will affect memory usage too). In this example, and throughout the models used in this work, we will favor speed over memory and therefore fully couple all our equations and use direct solvers.

### 2.7.1 Adaptive Mesh Refinement

The accuracy of the solution obtained by FEM is dependent on the quality of the mesh, something that was discussed in section 2.6. While the mesh designer can do much to create

a mesh that performs well for the particular problem posed, refinement of the mesh is often needed and should be performed for every new model.

There are two types of mesh refinements in FEM. The first type reduces the size of the elements and thereby the accuracy of the solution, this is called *h-type* refinement (*h* is often used to denote the mesh size). The second increases the order of the polynomial of the basis function, called *p-type* refinement which will likewise increases the solution accuracy.

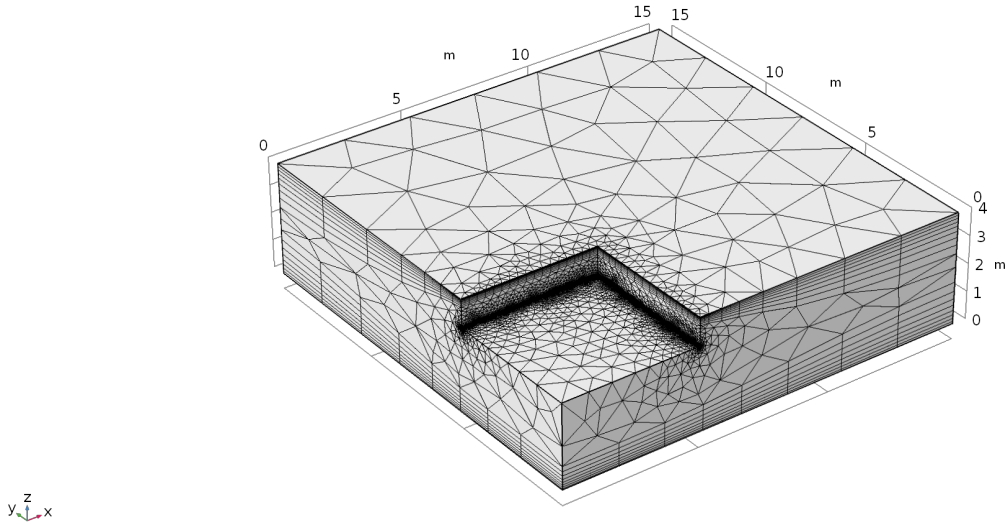
*h*-type refinement is generally more attractive because it is simpler and the computational cost of *p*-type refinement increase faster than *h*-type. However, *p*-types are useful if the user imports an already existing mesh, and is unable to change it, rendering *h*-type refinement impossible. These two method can be combined to perform a *hp*-type refinement.

Refinement is usually done by an algorithm, which is possible because FEM has the built-in ability to estimate the local error of the solution anywhere in the domain. The downside with using an algorithm is that the user has little control over how the mesh is refined. The user can also manually refine the mesh by solving the model and plot how some relevant metric converges as the mesh is refined. This can be a very time consuming, and therefore algorithms are usually preferable; a hybrid solution is to manually alter the mesh after the algorithmic mesh refinement.

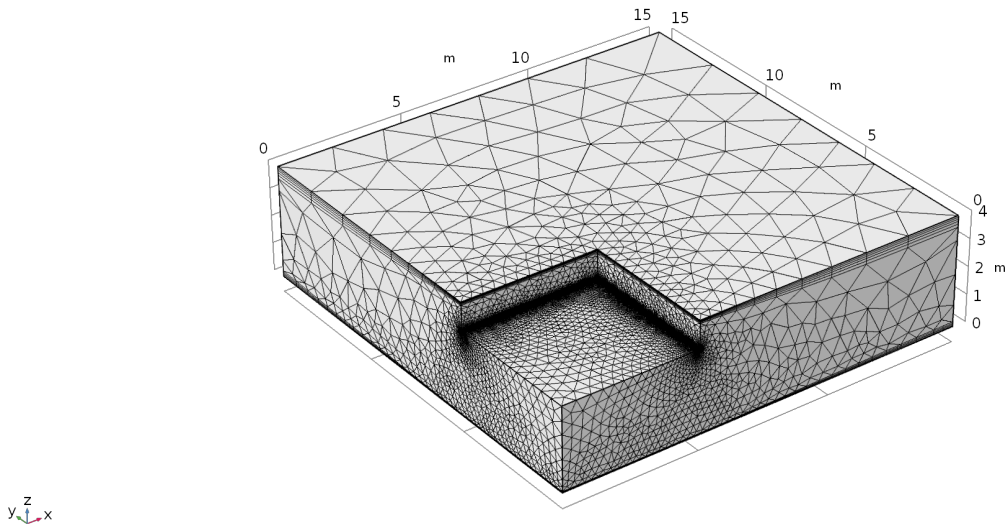
Refinement can either be done locally or globally. Global refinement involves defining some singular metric that will be used to evaluate the quality of the mesh, e.g. one might use the total stress in a metal bar as a metric here. In local refinement, one still has to define some metric for evaluating the quality of the refinement, but evaluation only occurs on a subset of the domain, e.g. the stress on just one boundary of the same metal bar. In both approaches the elements that have the largest estimated local relative error are refined, but the exact details of the refinement can differ between specific refinement algorithms. The local relative error is defined as the difference of the approximated solution  $u_h$  from one mesh to another.

$$e = u_{h1} - u_h \quad (2.41)$$

$e$  is the estimated local relative error (for every node);  $u_{h1}$  and  $u_h$  are the approximated solutions on the refined and original meshes respectively. The optimal type of refinement varies by problem, but a global refinement will generally be more computationally expensive.



(a) Original mesh. 362,657 elements.



(b) Refined mesh after global refinement w.r.t. the indoor contaminant concentration. 1,065,743 elements.

Figure 2.12: Original and adaptatively refined mesh.

In this work we will use a global h-type refinement and use the indoor contaminant concentration  $c_{in}$  as our refinement metric. COMSOLs refinement algorithm has the nice

ability to reinitialize the mesh, and can thereby coarsen elements, i.e. increase  $h$  where the local error is very small. This is handy as a fine mesh is not needed far away from the foundation crack - saving computational resources. In this example we will tell the algorithm to refine the mesh three times, and stop if the total number of elements exceed 1 million, with a maximum coarsening factor of 3, and element growth rate of 1.3, i.e. the number of elements increase by roughly 70% each iteration.

The result of this refinement can be seen in Figure 2.12 where the original and refined mesh are juxtaposed. Notice how the mesh is now denser near the foundation, the boundary layers tighter (in particular near the groundwater boundary), and how the elements are larger in the periphery. The original and refined meshes has 362,657 and 1,065,743 elements respectively.

Figure 2.13 shows how the value of  $c_{\text{in}}$  converges for each mesh refinement iteration. What is plotted is the change in calculated indoor contaminant concentration with iteration. Initially, very large changes are seen in the predicted values with the first iterations. By the 4th iteration, the improvements in estimates are getting very small.

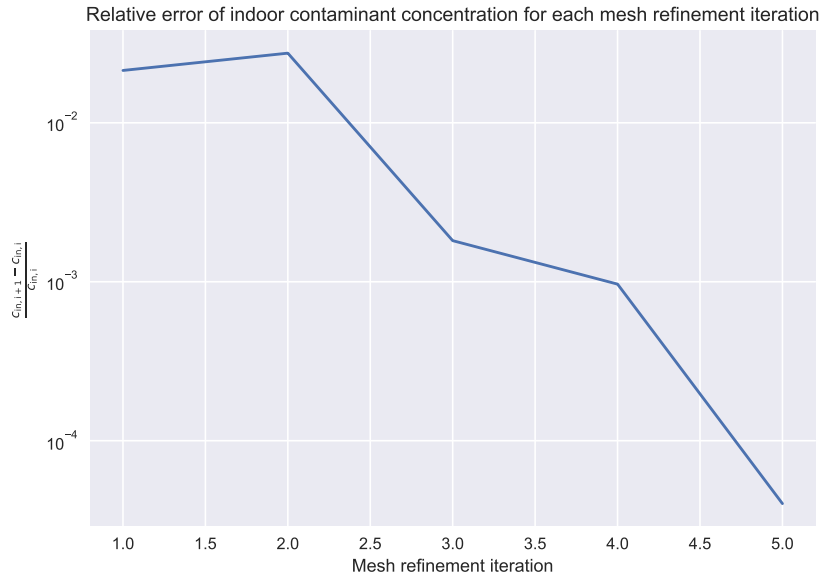


Figure 2.13: Convergence of indoor air contaminant concentration as the mesh is refined.

## 2.8 Post-processing & Results

One of the benefits of using a FEM software like COMSOL is its advanced post-processing capabilities. This allows the user to examine the physics driving VI in great detail. Figure 2.14 shows the resulting pressure field from solving Darcy's Law, as well as the associated airflow streamlines in the soil. Here we see the pressure in the near foundation crack region is roughly the same as the house pressurization of  $-5 \text{ Pa}$ , which quickly decreases towards the ground surface. It is also apparent how this pressure field induces a airflow from the ground surface, with air near the house heading relatively straight to the foundation crack, whereas the air further away from the house penetrates deeper into the soil and almost "whirlwinds" underneath the house.

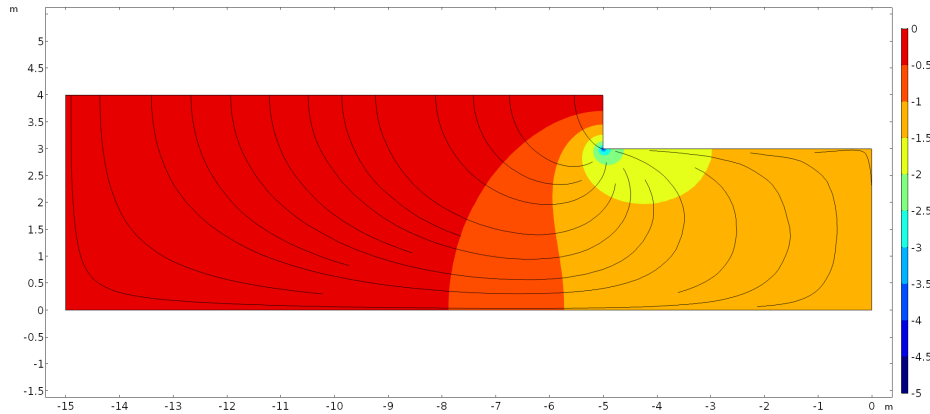


Figure 2.14: Pressure field from Darcy's Law with associated airflow streamlines.

The contaminant concentration in the soil, normalized to the groundwater source concentration and log-transformed, with the contaminant flux streamlines, is examined in Figure 2.15. Here see that far away from the house, the contaminant vapor simply diffuse straight from the groundwater source to the atmosphere, while beneath the house foundation, contaminant vapors accumulate because the foundation acts as a diffusion blocker. Based on those streamlines we can conclude that the advective component of the flux is very here small. Perhaps surprisingly, we do not see a significant advective transport downwards along the wall of the house. However, considering that the soil type is sandy loam, airflow velocities

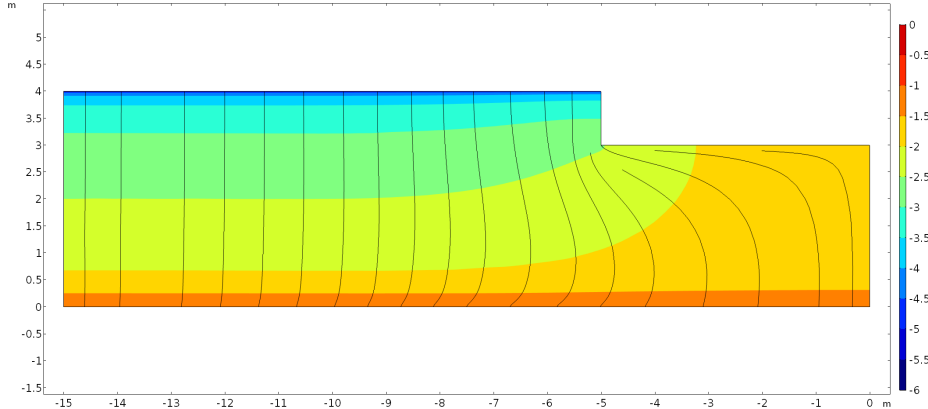


Figure 2.15: Contaminant concentration in the soil, normalized to groundwater concentration and log-transformed, with transport streamlines.

are expected to be small.

One might think that advective transport is large in the horizontal direction along the foundation slab, as the transport and airflow streamlines are so similar. However, by inspecting Figure 2.16 we see that airflow velocities are not greater here than elsewhere, and therefore the advective transport is not either. To make sense of this, we can inspect the horizontal diffusive flux, divided by the magnitude of the total flux

$$\frac{j_{\text{diff},y-\text{direction}}}{|j_{\text{total}}|} \quad (2.42)$$

to see what portion of the total contaminant flux transport the diffusive horizontal represents here. Figure 2.17 shows that the horizontal contaminant transport underneath the foundation is in fact driven by the large contaminant concentration gradient between the region underneath and outside the house foundation. This shows the power of modeling and how it can reveal things that at first seem intuitively correct, but in fact are not.

Another useful feature of post-processing is that it can be used for bug searching and to evaluate where the mesh can be potentially improved. When the transport equation is used to numerically model contaminant transport, there is a tendency for the solution to oscillate around the "true" solution, and thereby violate mass conservation, if the mesh size in a particular element is too large. This can be quantified by the cell Péclet number, which

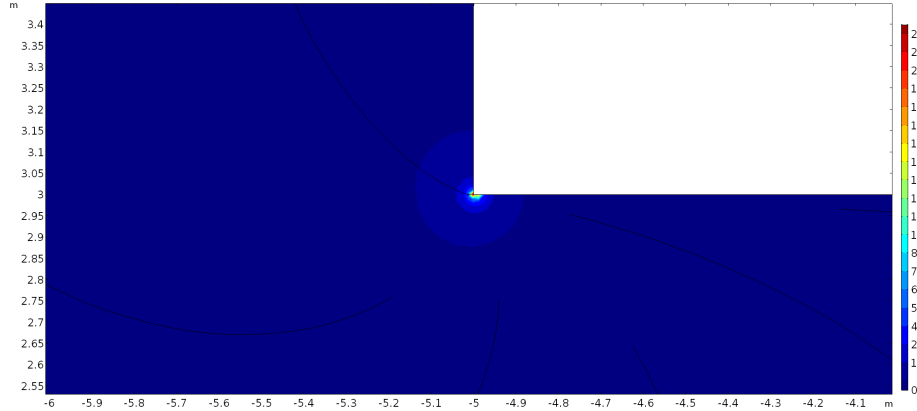


Figure 2.16: Airflow velocity  $\vec{u}_g$  [ $\text{mm h}^{-1}$ ] near the foundation crack with associated its streamlines.

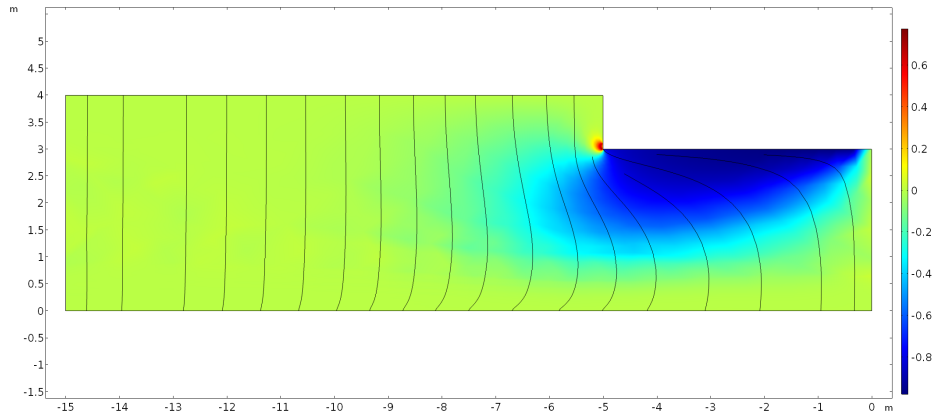


Figure 2.17: Horizontal (y-axis) diffusive flux component normalized to the magnitude of the total flux. A value of 1 here indicates that the total contaminant transport flux is due to diffusion, while 0 would indicate the opposite - that all contaminant transport is due to advection. The sign signifies the direction, with positive and negative values indicating a flux in the rightward and leftward direction respectively. E.g. a value of -0.8 indicates that the 80% of the magnitude of the contaminant transport is due to horizontal (along the y-axis) diffusion, and occurs leftward.

characterizes the relative magnitude of advection/diffusion in a cell.

$$\text{Pe}_{\text{cell}} = \frac{\text{adv}_{\text{cell}}}{\text{diff}_{\text{cell}}} = \frac{u_g h}{2D_{\text{eff}}} \quad (2.43)$$

here  $u_g$  [ $\text{m s}^{-1}$ ] is the soil-gas airflow velocity;  $h$  [m] is the mesh size in the element or cell; and  $D_{\text{eff}}$  [ $\text{m}^2 \text{s}^{-1}$ ] is the effective diffusivity in the cell. If  $\text{Pe}_{\text{cell}} > 1$  there is a risk that this oscillating behavior will manifest. Small exceedances,  $\text{Pe}_{\text{cell}} < 25$ , are usually mitigated

by various stabilization schemes, which are inherently integrated into COMSOL as well as many other FEM packages, but for larger values further mesh refinement may be required.

Figure 2.18 shows  $Pe_{cell}$  as a volume plot, and excludes all values that fall below one. As we can see, only the region close to the groundwater exceeds  $Pe_{cell}$ , which is due to the very small  $D_{eff}$  there. The exceedance is small, so the stabilization scheme is able to compensate which is confirmed by Figure 2.15 (no oscillations visible). This is also a region where even if such oscillations occurred, would probably not affect the indoor contaminant concentration. Regardless, Figure 2.18 shows where the mesh may potentially be refined, which comes in handy to know if one runs a model where airflow velocities are significantly higher than in this example.

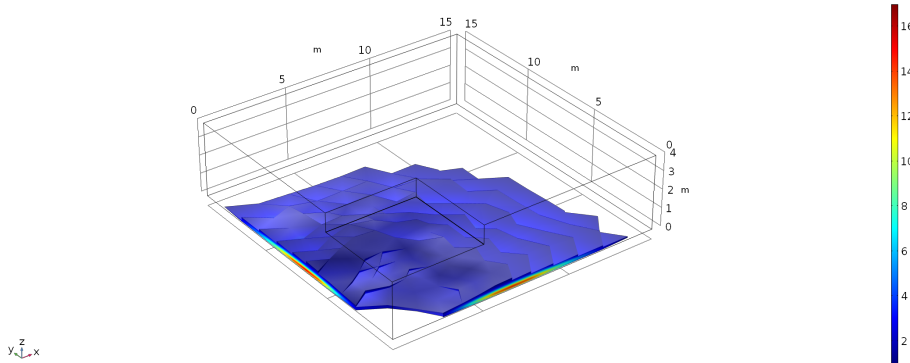


Figure 2.18: Volume plot showing where the cell Péclet number exceeds 1 and its actual value. I.e. it suggests where the mesh may be improved.

## 2.9 Review of Vapor Intrusion Models

Mathematical models of VI were from an early stage adopted by investigators and regulators alike. The primary purpose of these was to provide screening-level risk assessment, i.e. determine if a particular site likely to be impacted by VI based upon specific site characteristics such as groundwater contaminant concentration measurements. This was necessary as VI sites are potentially numerous and a means to prioritize was needed. Since such models

had successfully been used in radon intrusion, similar ones were, and still are, developed for VI[7].

The EPA has recommended the use of VI models as a screening risk assessment tool as well as a line-of-evidence in VI investigations in conjunction with field measurements[7]. Likewise, various VI models have been used in many European countries in similar applications[52]. However, the main obstacle of using models in VI investigations has been, and still is, the difficulties of validating them. These difficulties stem from the lack of available comprehensive datasets of VI sites and the inability to change the conceptual site model (CSM) that underpins the development of many of the most widely used VI models, e.g. if a particular model assumes the only contaminant source is the groundwater, it will never perform well for a site that is characterized by a preferential pathway. Regardless, VI models offer a means to examine the underlying physics that drive VI and is therefore a valuable research tool.

### 2.9.1 Analytical Models

One of the first, and arguably one of the most well-used VI model was developed by Johnson and Ettinger[33], the J&E model, and was based on much of the modeling work by Nazaroff[32]. Here a VI scenario similar to the one presented here was used as a basis for their mode, i.e. a house overlying an infinitely contaminated groundwater source, where contaminant vapors enter through a foundation crack along the perimeter of the foundation. However, due they sought to develop an analytical model, and therefore certain physics was discarded to enable them to solve the associated PDE.

One such is that contaminant transport from the groundwater source to the building foundation was assumed to occur solely through diffusion. This is a reasonable assumption, as we have seen airflow is very slow in the soil, and especially in the deeper parts of the soil, so in most scenarios, contaminant transport here will be dominated by diffusion. The contaminant diffusivity was likewise modified using Millington-Quirks model. However, their

implementation lacked a way to model the soil moisture content, which instead had to be supplied by the user. Multiple soil layers were supported and with sufficient knowledge or assumptions, and using these, effective diffusivities could be reasonably approximated.

While diffusion was assumed to be the only transport mechanism in the soil, both advection and diffusion was assumed to contribute to contaminant entry into the building. The advective contaminant flow through the foundation crack was here determined using a modified version of Darcy's Law that had been developed previously by Nazaroff[53] where the driving force was the pressure differential between the indoor and outdoor environments. However, this approach lacks the relative permeability term from van Genuchten, and requires user input to determine the effective soil permeability. Contaminant entry through the crack was modeled as transport between two parallel plates, and involved solving the one-dimensional advection-diffusion equation at steady-state. Indoor contaminant concentration was determined in a similar fashion as presented here, i.e. as a steady-state mass balance between the contaminant entry and expulsion, the latter which is controlled by air exchange rate. A major drawback of this model is its one-dimensional nature, which forces all of the contaminant released from groundwater beneath a building to enter that building. That is, no lateral transport of contaminant could be included.

In 1998 the EPA implemented the J&E model as a spreadsheet tool for screening risk, where the user could give a wide variety of input such as air exchange rate, building pressurization, groundwater contaminant concentration, define multiple soil layers with their associated permeabilities and porosities, etc. Thus, the model was adopted by investigators and regulators as a risk assessment screening tool[7]. However, recently many state regulatory agencies have begun to question the use of these sorts of models in VI investigations and currently are given relatively low weight when considering if a site is impacted by VI.

Following the J&E model, a wide variety of analytical models were developed. These were often similar to the J&E model in many regards, and often used the same governing equations, but with modifications to accommodate different VI scenarios. For instance some

would have contaminant entry via a crawl space instead of a foundation crack[54], or include soil biodegradation[55, 56]. Yao et al.[57] wrote a comprehensive review of VI models, discussing their advantages and disadvantages, and which type of scenarios they modeled. However, due to the analytical nature of these models, some physics had to be omitted in order to develop an analytical solution to that particular problem; this is the inherent disadvantage of analytical VI models.

## 2.9.2 Numerical Modeling

Numerical models do not require the sacrifice of any physical phenomena to be solvable and can be solved in up to three-dimensions, while most analytical models are one-dimensional. Thus numerical models can offer a more detailed and generalized description of a wider range of VI scenarios. However, solving numerical models to a satisfactory accuracy can be challenging and often require some expertise on behalf of the user, and such can be less accessible compared to the analytical spreadsheet models. But from a research perspective they are far more interesting for examining the physics driving VI.

### **Abreu and Johnson Model.**

Abreu and Johnson[34] developed one of the first numerical model of VI - the "ASU model". This model considered the same VI scenario as in the J&E model and what has been presented here; an infinitely contaminated groundwater source with contaminant entry into the overlying building occurring through a 1 mm perimeter foundation crack. The Abreu model was a three-dimensional model developed using a finite difference approach.

Abreu used a similar mathematical description to the one presented here, i.e. used Darcy's Law to characterize flow of the soil-gas, the advection-diffusion equation for contaminant soil transport, the indoor environment was modeled as a CSTR, and the expression for contaminant entry into the building was the one developed in the original J&E model. Biodegradation was also supported in their model.

A key difference between the Abreu model and this one was that they do not simulate the effect of soil moisture as a function of elevation above groundwater. Instead, different soil moisture content would either be defined by the user for the entire soil domain, or for specific layers - very much like in the J&E model. Thus, contaminant transport in the soil would be less well described.

The Abreu model was used in a collaborative project with the EPA to investigate a wide range of VI topics. For instance, they investigated the effect of other buildings adjacent to a VI impacted building, how a laterally located groundwater source (i.e. the source is not directly below the building) affect contaminant entry, and combinations of these. They also considered finite sources in transient simulations, effect of an impermeable ground cover (like a sidewalk) around a building, and many more. However, a limitation of their study here was that they only considered sandy soils.

### **The Brown Model**

A new addition to the family of VI models was the predecessor to the finite element model presented here. This 3D model was originally developed by Pennell, Bozkurt, and Suuberg[35] - the Brown model. In terms of governing equations and mathematical description of VI, it was quite similar to the Abreu model. Specifically, soil-gas airflow was again modeled using Darcy's Law, soil contaminant transport with the advection-diffusion equation, the indoor as a CSTR, and expression for contaminant entry into the building was the one from the J&E model. The FEM nature of the model meant that heterogenous soil conditions could easily be modeled. Another benefit of this model was that it was able to run transient, or time-dependent simulations. However, this model did not calculate soil moisture content and its effect on contaminant transport.

Investigating various heterogenous soil conditions was the topic of one of the first works using this model by Bozkurt, Pennell, and Suuberg[58]. They investigated how different soil layers of different properties alter the soil-gas contaminant concentration profiles. Their

findings reinforced the importance of accurately characterizing the geology underneath a VI impacted in the development of its conceptual site model. In particular, clay layers in the soil were found to have a particularly profound effect on soil-gas contaminant concentrations.

Yao, Pennell, and Suuberg[59] used the same model to investigate how "capping" around a building affects soil-gas contaminant concentrations, e.g. how does a sidewalk affect contaminant concentration profiles. Using this they showed that caps in close proximity to a building can have a significant effect on soil-gas contaminant concentrations. For instance, buildings with very shallow foundations but were surrounded by an impermeable pavement, had relatively higher indoor contaminant concentrations than buildings without paving but whose foundations were a few meters bgs. Some other VI investigated by Yao et. al. was to explain the order of magnitude variability in attenuation factors in the EPA database[60], oxygen limited biodegradation of VOCs in soils[61], and the effect of modeling other contaminant entry pathways other than a perimeter crack[37], where it was concluded that for the "classic" modeled VI scenario, the location or shape of the crack has little impact on overall VI.

Shen and Suuberg[62] used the Brown model to study the effect of time-varying soil-gas entry (i.e. volumetric air flow) and air exchange rate. Here they showed that these variations can significantly contribute to variations in indoor contaminant concentrations. Air exchange rate could under some circumstances contribute to roughly an order of magnitude, while soil-gas entry more than that.

## CVI2D and PVI2D

Verginelli, Yao, and Suuberg[63] developed a steady-state two-dimensional analytic VI model. Here they considered the "classic" VI scenario with a free-standing building, surrounded by open ground, with a perimeter crack, and a groundwater source. A solution to the presented governing equations was established using the Schwarz–Christoffel mapping method. This model comes in two versions, one for primarily chlorinated solvents - chlorinated va-

por intrusion tool 2D (CVI2D). The other mainly deals with petroleum contaminants and VOCS, and supports (oxygen limited) biodegradation - petroleum vapor intrusion tool 2D (PVI2D). These tools have been well received, in particular by the Chinese regulatory community, where they are often used to assess potential VI risk at brownfield sites prior to new construction.

# **Chapter 3**

## **Preferential Pathways: Drivers of Temporal and Spatial Variability in Vapor Intrusion**

### **3.1 Summary**

Preferential pathways have recently been recognized for the significant role that they may play in enhancing vapor intrusion (VI). The nature and specific effect of a preferential pathway can vary greatly and is largely site specific; generalizing their impact can therefore be difficult. Two well-studied VI sites were revealed to be impacted by preferential pathways, providing an excellent opportunity to explore their influence. One of these sites was in Layton, Utah, which featured a preferential pathway that had a very significant impact on, among other things, but in particular, the temporal variability of indoor contaminant concentration. This preferential pathway was at a later date closed, and the comparison between the periods before and after the closing offers some unprecedented opportunities for understanding preferential pathways. A preferential pathway similar to that one will be implemented in our numerical model, and through analysis of data from the site, will offer

insights how preferential pathways can enhance VI. The implications of these insights have wider consequences for VI investigations in general, which is further explored in Chapter 4. Another well-studied site in Indianapolis, Indiana, was also affected by a preferential pathway, but its role and influence was very different from the Layton site, and in particular played a significant role in the spatial variability of subsurface contaminant concentrations, a topic which will be explored using data from that site, as well as from the Layton site.

## 3.2 Introduction

Long term vapor intrusion (VI) studies in both residential and larger commercial structures have raised concerns regarding significant observed transient behavior in indoor air contaminant concentrations of anthropogenic origin[7, 17, 24, 64, 25, 28, 65], a phenomenon that has previously been observed at houses impacted by radon intrusion[66]. Such variations make it difficult for those charged with protecting human health to formulate a response and conduct appropriate risk evaluation. Furthermore there is uncertainty within the VI community regarding how to best develop sampling strategies to address this problem[7, 24, 67, 28].

To address these concerns, two groups concerned with vapor intrusion researched purchased two different VI impacted houses and outfitted them with a wide variety of sensors and sampling instrumentation to study VI at these houses in great detail. Indoor contaminant concentration as well as soil-gas and groundwater contaminant concentration at different depths and locations were recorded, while simultaneously recording metrics such as indoor and outdoor temperature, wind speed and direction, and building pressurization. These measurements were taken continuously over multiple years, offering an unprecedented detailed dataset for exploring VI.

One of these houses was in Layton, Utah, near Hill AFB, and was purchased by a research group at Arizona State University (ASU), who conducted most of the research at the site -

this site will be referred to as the "ASU house" throughout this work[24]. The other was in duplex in Indianapolis, Indiana, purchased by the U.S. EPA and will be referred to as the "EPA duplex". There work was performed by multiple groups.

One thing both of these sites had in common was that after a few years of study, preferential pathways were discovered at the sites. A preferential pathway is typically thought of as some conduit that can transport large amounts of contaminant vapors into a building, in contrast with the slower vapor transport through soils.

At the ASU house, this took the form of a land drain underneath the house foundation, presumably installed during earlier house construction to drain excess water from the sub-slab region. This land drain was connected to the nearby sewer and its entrance as in a gravel layer under the house foundation, near a breach in the slab. The sewer it connected to was buried deep enough to be partially submerged in the TCE contaminated groundwater, which likely infiltrated into the sewer. The land drain when discovered was later excavated and fitted with a valve, allowing the researchers to control its influence - which was revealed to be very significant[23]. The details of this are covered further below.

At the EPA duplex, the sewer acted as a preferential pathway, somewhat similar to the ASU house, but the nature of this preferential pathway was quite different from the one at the ASU house. A tracer gas test demonstrated that contaminant vapors were directly transported into the duplex[22]; similar to a site in Boston, Massachusetts, where PCE was transported into a bathroom through broken plumbing fixtures[21]. It was also demonstrated that contaminated groundwater infiltrated into the sewer from a few blocks away from the duplex, where a dry-cleaners had previously been. This type of distributed contamination via a sewer network has likewise been recorded in Denmark[68] as a VI source - giving rise to a very different situation compared to radon intrusion or vapor intrusion from a groundwater source involving no preferential pathway.

It is also likely that the sewer pipe at the duplex leaked contaminant vapors somewhere near the vicinity of the house. This would give a situation that is similar to the ASU house

land drain, but somewhat mitigated since the pipe leakiness was likely due to structural degradation, e.g. cracks in the mantle area; quite different from open channel flow from the ASU house land drain that brought contaminated air directly to the sub-slab area.

These studies shows some of the diverse ways that a preferential pathway can play a role in VI (Figure 3.1 shows a visual summary of these ways), and illustrate our often poor understanding in evaluating their significance. However, since the influence of the preferential pathway at the ASU house was able to be turned on and off (via the valve), we have an unprecedented opportunity to explore the effects of such a preferential pathway at a VI site.

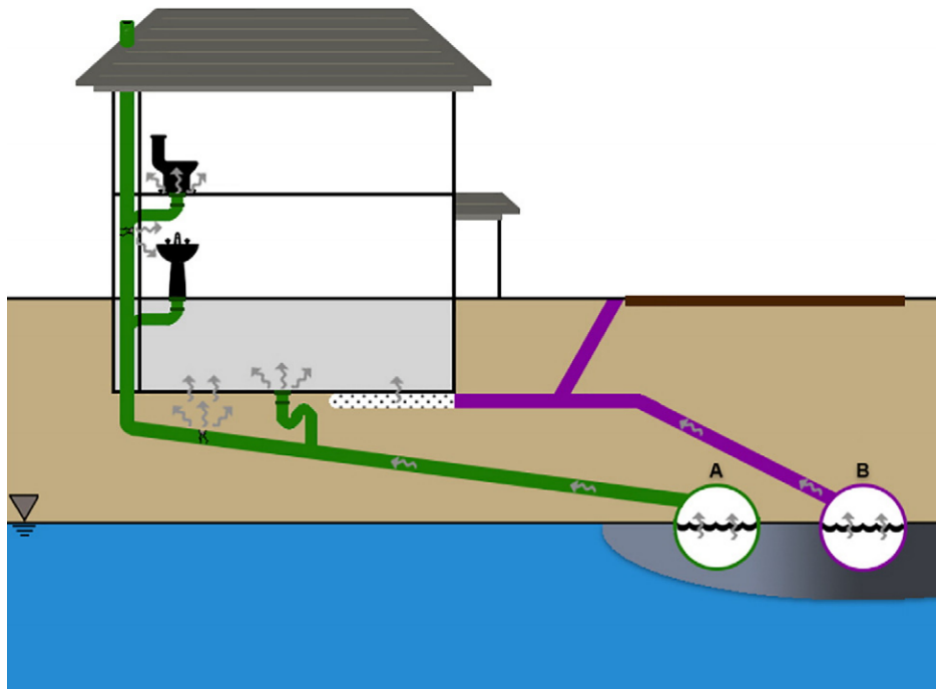


Figure 3.1: Visual summary of some of the different ways that contaminant can transport into a VI affected building via preferential pathways. Figure from McHugh et al.[22].

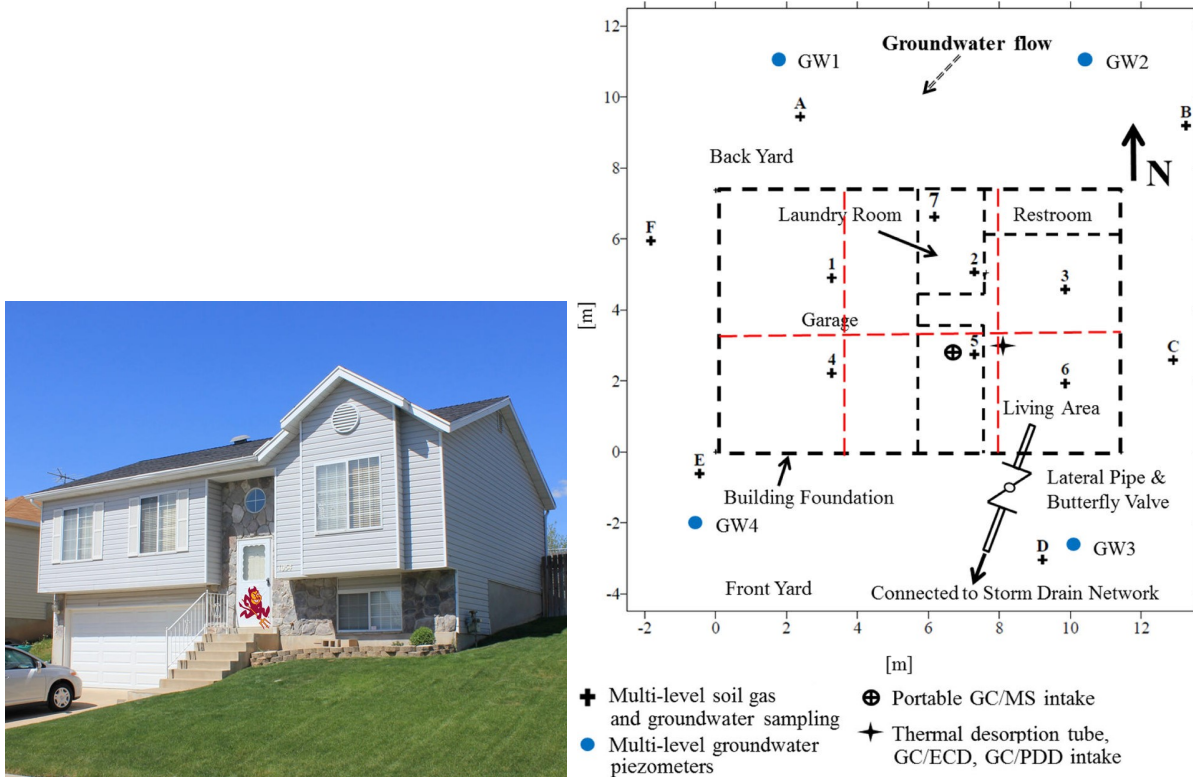
### 3.2.1 The ASU House

The VI study at the ASU house had two primary purposes:

1. Investigate VI with a particular focus on understanding the temporal and spatial variability.

2. Test and evaluate the performance of the controlled pressure method (CPM).

This was to be achieved by monitoring various metrics relevant to VI, such as building pressurization, air exchange rate, indoor and outdoor temperature, and other metrological variables, while simultaneously monitoring the indoor air contaminant concentration. Additionally, soil-gas and groundwater contaminant concentration underneath and around the house were monitored; the specific sampling locations, as well as a photo of the house, can be seen in Figure 3.2a. The study of the ASU house is one of the most detailed studies of a VI site to date and fully describing the experimental setup and measured metrics is beyond the scope of this work but is detailed in Holton et al.[24].



(a) Picture of the ASU house from Holton et al.[24] (b) Floor plan of the lower level of the "ASU house". Locations of all sampling ports and of the land drain preferential pathway marked. Figure from Guo et al.[23].

Figure 3.2: The "ASU house" VI site in Layton, Utah.

CPM seeks to control the pressurization of the building, thereby controlling the contam-

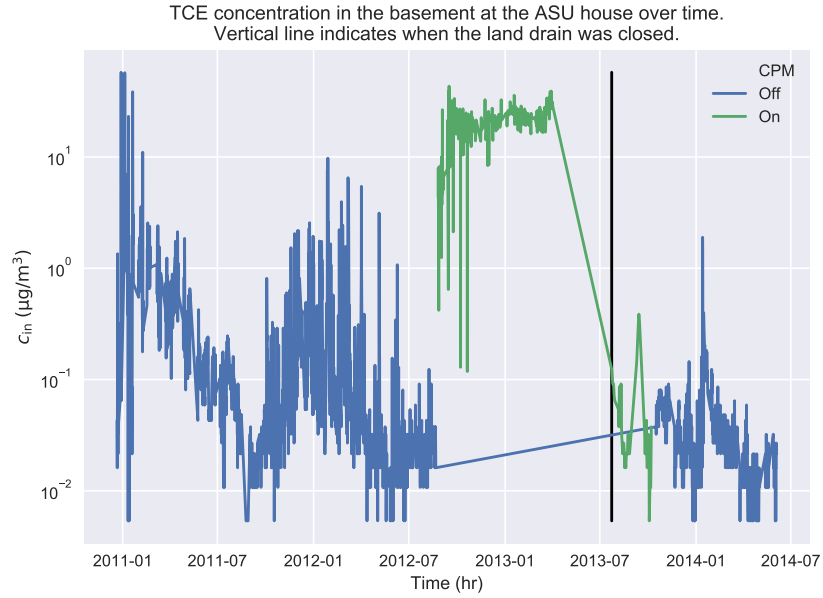
inant entry rate. In this framework, overpressurizing a building will minimize or eliminate contaminant entry rate by VI into the building, thereby identifying existence of indoor contaminant sources. By contrast, depressurizing a building will increase contaminant entry rate, giving a theoretical "worst-case" VI scenario. At the ASU house, the researchers would used a 20 inch window box fan to control the pressurization of the building.

The site was monitored for roughly 1.5 years before the testing of the CPM system commenced. During this time, it was established that the indoor contaminant concentration fluctuated significantly at the site - roughly an order of magnitude on a weekly basis, while up to three or more orders of magnitude on a seasonal basis. Once the house was depressurized using the CPM system, indoor contaminant concentration increased to higher concentration levels previously recorded providing an initial verification of the CPM strategy[29].

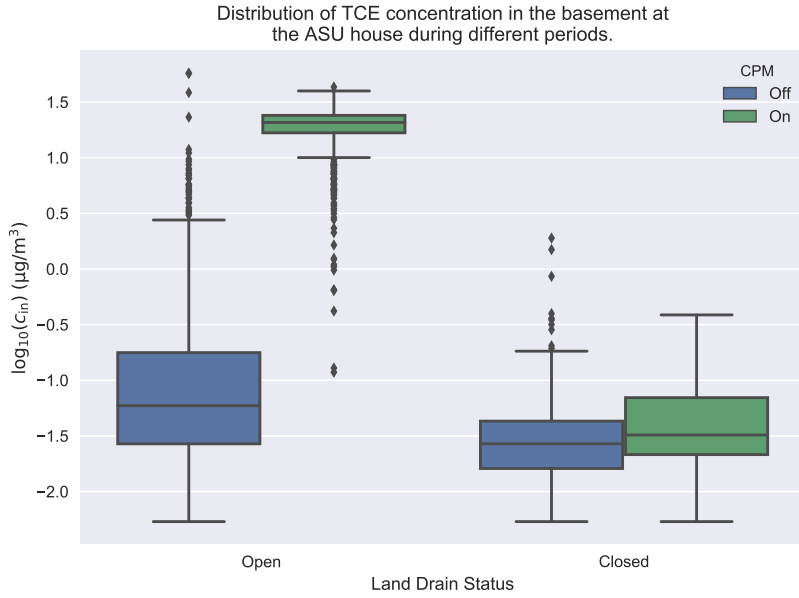
However, during the CPM testing period, the researchers noticed that the house and nearby sewer seemingly communicated with each other. This was shown by the movement of a plastic tarp, which covered a nearby manhole, as the door of the house was opened and closed. This lead to the discovery of the land drain preferential pathway at the site; the location of it in relation to the house floorplan can be seen in Figure 3.2b. The land drain was determined to exit into the gravel sublayer beneath the foundation, near a visible breach in the foundation slab, and was subsequently excavated and fitted with a butterfly valve [23] to control its influence.

The land drain was closed towards the later part of the CPM study, which lead to a significant decrease in indoor contaminant concentration. This effect can be seen in Figure 3.3a, which shows the log-10 transformed indoor contaminant concentration for the entire study period. Here the pre- and post-CPM periods are marked by colors, and the closing of the land drain by the black vertical line. Notice how the temporal variability in indoor contaminant concentration decrease significantly after the closing of the land drain.

Figure 3.3b shows the same data, i.e. the log-10 transformed indoor contaminant concentration, but as a boxplot instead of a timeseries plot. Here the colored box represents



- (a) The temporal variability of indoor air contaminant concentrations recorded at the ASU house. Measurements were taken in the basement. The periods during which the CPM system was on and off are marked.



1

- (b) Boxplot showing the log-10 transformed TCE concentrations at the ASU house. The CPM and natural periods, and the period before and after the land drain was closed are considered separately. The box signifies the interquartile range (IQR) of values, with the central line representing the median value, and the top and bottom of the box are the 25th and 75th percentiles. The whiskers extend to 1.5 times the IQR. Markers indicate outlier data points that fall outside the whiskers.

Figure 3.3: Analysis of the indoor contaminant concentration at the ASU house.

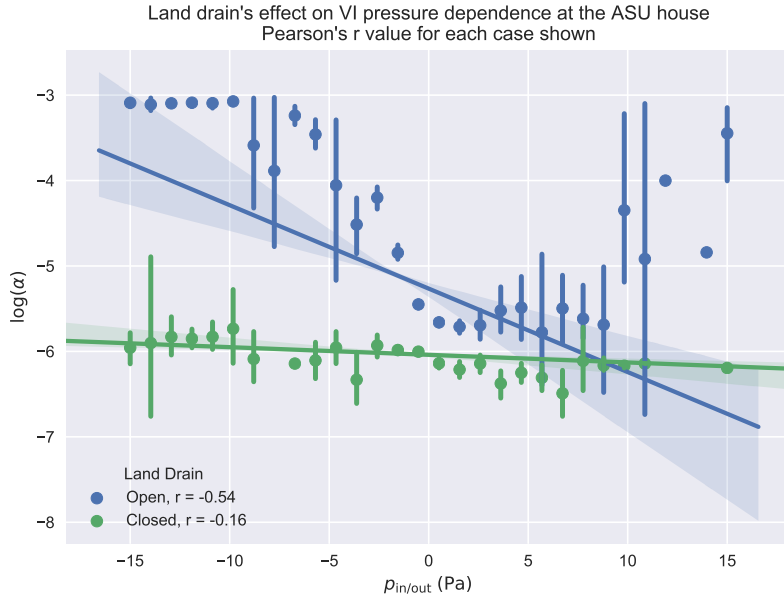


Figure 3.4: Regression plot showing the indoor/outdoor pressure difference dependence on indoor air concentration. Here the indoor air concentration is normalized to the groundwater source concentration, i.e. attenuation factor, and log-10 transformed. Data is placed in evenly spaced (but not sized) bins. The bars indicate the 95% confidence intervals.

the interquartile range (IQR) of the distribution - the middle line is the 50th or median value, while the top and bottom of the represent the 75th and 25th percentile values. The whiskers are the extent of the dataset, while "outlier" points are given by the dots, here formally defined as data lying 1.5 times outside the IQR; these are "real" data points but simply plotted as outliers not to skew the IQR. This figure again reinforces the significant effect that the land drain preferential pathway had on the temporal indoor contaminant concentration variability at the ASU house.

In the VI field, it is widely held that the building depressurization relative to the ambient outdoor is a key driver of contaminant entry into VI impacted building. Since building pressurization fluctuations can occurs rapidly, this is a prime factor for investigating the transport dynamics of the preferential pathway. Figure 3.4 considers the relationship between the indoor air concentration and building pressurization, specifically indoor/outdoor pressure difference, for the periods when the preferential pathway was open and closed. This clearly

shows the dramatic change in sensitivity of the indoor contaminant concentration to building pressurization after the closing of the preferential pathway, which is not only apparent from visual inspection but also from the change in the Pearson's r values for the considered periods. Pearson's r essentially tells us how good is a linear correlation between two datasets; a value of 1 indicates that there is a perfect positive linear relationship, and -1 a perfectly negative linear relation. In our context, a negative value indicate that a decrease in building pressurization leads to an increase in indoor contaminant concentration, which makes sense as contaminant entry rates into the house would increase as it is further depressurized.

The question then becomes why this fundamental shift in the relationship between building pressurization and indoor contaminant concentration occurred, and how it relates to temporal variability in indoor contaminant concentration. Answering this is one of the primary objectives of this thesis, which will be done by developing a numerical model of a VI site that is *similar* to the ASU house, and in combination with comparison to the field data, will give insights how a preferential pathway can fundamentally alters contaminant transport at a VI site. We will also explore how such a preferential pathway can significantly contribute to the spatial variability in contaminant concentration, in particular in the near sub-surface region.

### 3.2.2 EPA Duplex

The EPA duplex was, similarly to the ASU house, the subject of a highly detailed VI study; Figure 3.5a shows a photo of the site. Here the indoor contaminant concentrations of TCE, PCE, chloroform, and radon were measured in different floors of each side of the duplex, as well as in different locations and depths in the subsurface and groundwater - these sampling location ports, as well as a floorplan of the duplex can be seen in Figure 3.5b. These sampling ports also allowed pressure differences between different locations to be measured. Metrological data were collected throughout the study period, which lasted for around 2.5 years, and included indoor and outdoor temperatures, wind speed and direction,

precipitation, and recorded snow coverage[65]. The data from this site are publicly available online[69].

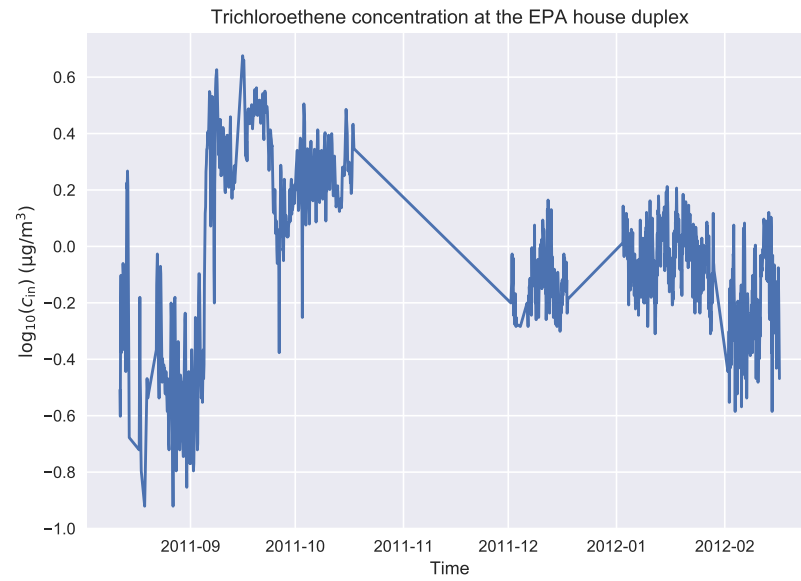


(a) Photo of the EPA duplex. The right-hand side is the heated "422" location ports.  
side, while the left-hand side is the unheated "420" side.

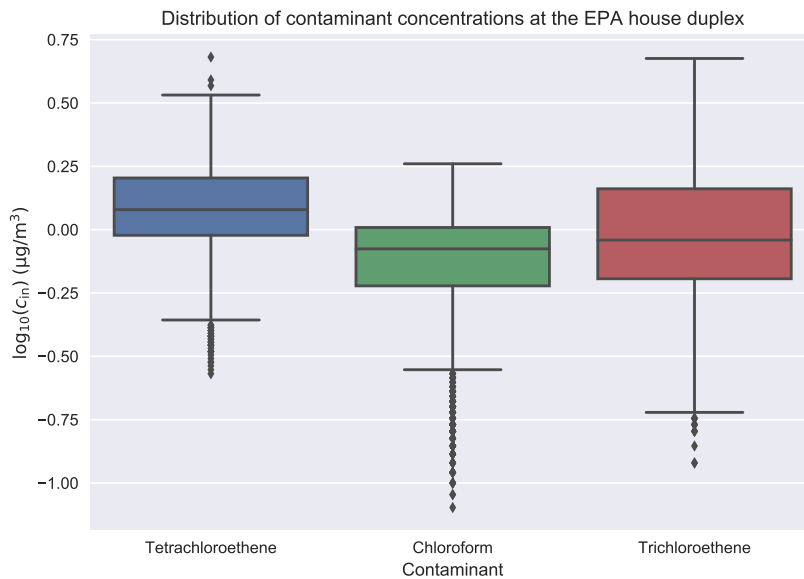
Figure 3.5: The "EPA" duplex VI site in Indianapolis, Indiana.

This site was likewise characterized by significant temporal variability in indoor contaminant concentrations, which can be seen in Figure 3.6. This variability was not as significant as was recorded at the ASU house, but substantial nonetheless. Understanding the observed variability was a major focus of this study, but additionally the researchers sought to evaluate the efficacy of a subslab depressurization (SSD) system. A SSD system depressurizes the subslab region, which diverts contaminant vapors from entering the structure into a pipe placed through the foundation slab, which then expells the vapors into the atmosphere[65]. There are many different possible configurations of these pipes, and their design is its own research topic, one which will not be addressed in this work. However, it is important to know when they were operated, and we will only consider data before the implementation of the SSD system. It should also be noted that only one side of the duplex was heated, and we will only consider data from this side.

Like the ASU house, it was later determined that a sewer preferential pathway existed at the site. This preferential pathway seemingly played a very different role than the one found at the ASU house, and different in primarily two ways:



(a) Time series plot of the indoor TCE concentration in the heated side of the EPA duplex. Only the period before the SSD system was turned on considered.



(b) Boxplot showing the distribution of log-10 transformed indoor concentration of three different contaminants in the heated side of the EPA duplex. The box is the interquartile range, with the line in the middle representing the median, and the top and bottom of the box representing the 75th and 25th percentiles respectively. The whiskers denote the extent of the data, with the points classified as "outliers", and are defined to be 1.5 times the IQR range.

Figure 3.6

1. Infiltration of contaminant vapors into the sewer did not occur near the duplex, but instead occurred a few blocks away - at the site of an old dry cleaner.
2. Communication between this preferential pathway and the indoor environment does not seem to have been as strong; the researchers believe that this may be due to the poor condition of the sewer pipe, which may have leaked somewhere along its path.

The first of these points was demonstrated by McHugh et al.[22], which tracked contaminant vapors along the length of the sewer system. The second point, or rather the evidence that communication between the indoor environment and the preferential pathway may not have been so strong is indicated by the lower temporal indoor contaminant concentration variability. It is also indicated by the weaker association between indoor contaminant concentration and the indoor/outdoor pressure difference, which can be seen in Figure 3.7; this weaker association is indicated by the smaller Pearson's r values compared to the ones at the ASU house before the closing of that preferential pathway.

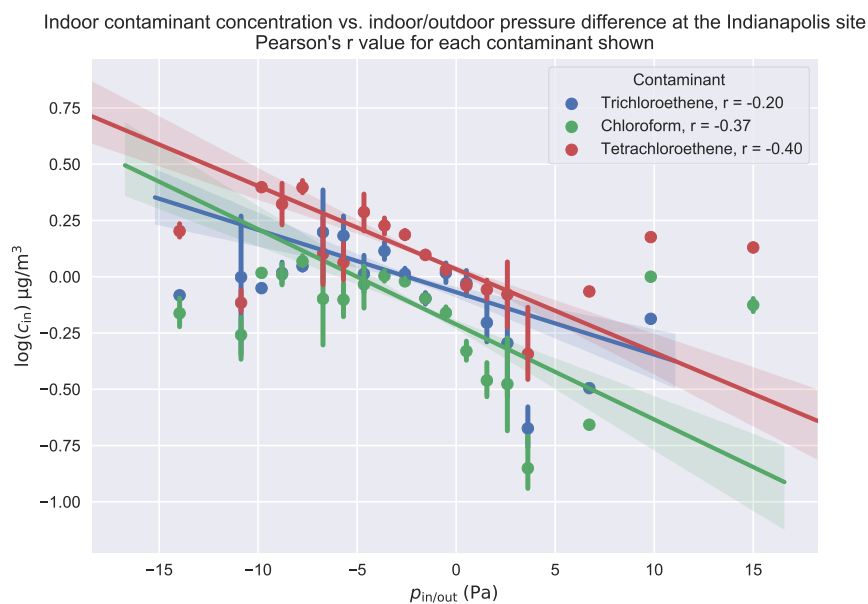


Figure 3.7: Relationship between indoor/outdoor pressure difference and indoor contaminant concentration of three contaminants - TCE, PCE, and chloroform at the EPA duplex.

Unfortunately, the EPA duplex preferential pathway is less well characterized, and its

influence was never removed. This makes it difficult to assess how it contributed to overall VI at the site, or the observed temporal variability in indoor contaminant concentrations. However, it is possible to explore if the preferential pathway leaked somewhere near the site - which likewise will be a focus in this chapter.

In the case of the ASU House, the preferential pathway delivered the contaminant vapor directly to the gravel subbase that underlay the foundation slab, and there was good communication with the interior of the house, via a large crack between the foundation slab and wall. At the EPA Duplex, the situation was not nearly as clear. There was also a sewer pipe that led into the building, but unlike the sewer line at the ASU House, it did not "dead end" in such a fashion that vapor leakage was inevitable. Rather, the sewer line at the EPA Duplex was of the more usual kind that ended in traps within the building. Properly maintained traps (i.e., those kept filled by water use in the building) are excellent barriers to vapor entry - that is their design. It is when traps are permitted to dry out that vapor entry into a house from the sewer becomes possible. The extent to which that might have been the case at the EPA Duplex is unknown. But beyond this mechanism, a sewer line can still be an effective conduit for carrying contaminant vapor to the property. The question is whether there is a pathway into the building. We believe that the evidence from the EPA Duplex suggests that the sewer line might actually have delivered contaminant vapor to the soil immediately adjacent to the structure, via a break in the sewer line. Breaks in sewer lines are not at all uncommon, and sewer lines, once placed, are rarely maintained.

Determining the possible leakiness of the possible sewer line preferential pathway at the EPA duplex will be done by performing a kriging analysis of the measured contaminant concentrations in the soil gas surrounding the duplex sampling. Kriging is a type of interpolation technique which allows sparse data to be interpolated in multiple dimensions. It is ideal for interpolating soil-gas contaminant concentration in the soil surrounding the duplex. This allows one to visually inspect the interpolated soil-gas contaminant concentration for "hot spots", which could indicate where such a leak might be.

In what follows, numerical VI modeling is performed that is relevant to the two different types of preferential pathway scenarios. First, the ASU House scenario is considered, as its character is better established. Then the situation at the EPA duplex is considered, in order to see if that different sort of preferential pathway can make a difference.

### 3.3 Modeling A Preferential Pathway

To investigate the role a land drain type preferential pathway may have on a VI site, we extend the VI model presented in Chapter 2. This is effectively looking at the situation known to exist at the ASU house, but without fully capturing all of the details from that site. By adding a gravel sub-base layer underneath the foundation slab and a preferential pathway conduit to the earlier presented model, we have developed a VI model scenario that is similar to that at the ASU house.

Here we assume the gravel sub-base layer is 30 cm thick and extends from the edges of the foundation slab. While the exact thickness of the gravel sub-base layer at the ASU house is not known, it was estimated to be roughly that thick. This is a typical thickness in US residential construction. The soil surrounding the house is assumed to be homogenous sandy clay. This is based on a description of the soil, and was chosen as the appropriate choice in modeling work by Guo[70], one of the researchers at the ASU house.

The gravel sub-base, unlike the rest of the soil, is relatively dry; it is covered by the foundation slab, so no rain infiltration will occur, and due to the coarseness of the gravel, no moisture will be drawn up by capillary forces. Nonetheless, some van Genuchten parameters for the gravel are necessary. Table B.1 has the van Genuchten parameters used to model the soil and gravel.

Based on the description of the land drain preferential pathway at the ASU site, we modeled the preferential pathway as a 10 cm diameter pipe that exits at the interface between the soil and gravel sub-base layer. It terminates near the foundation crack - as was actually

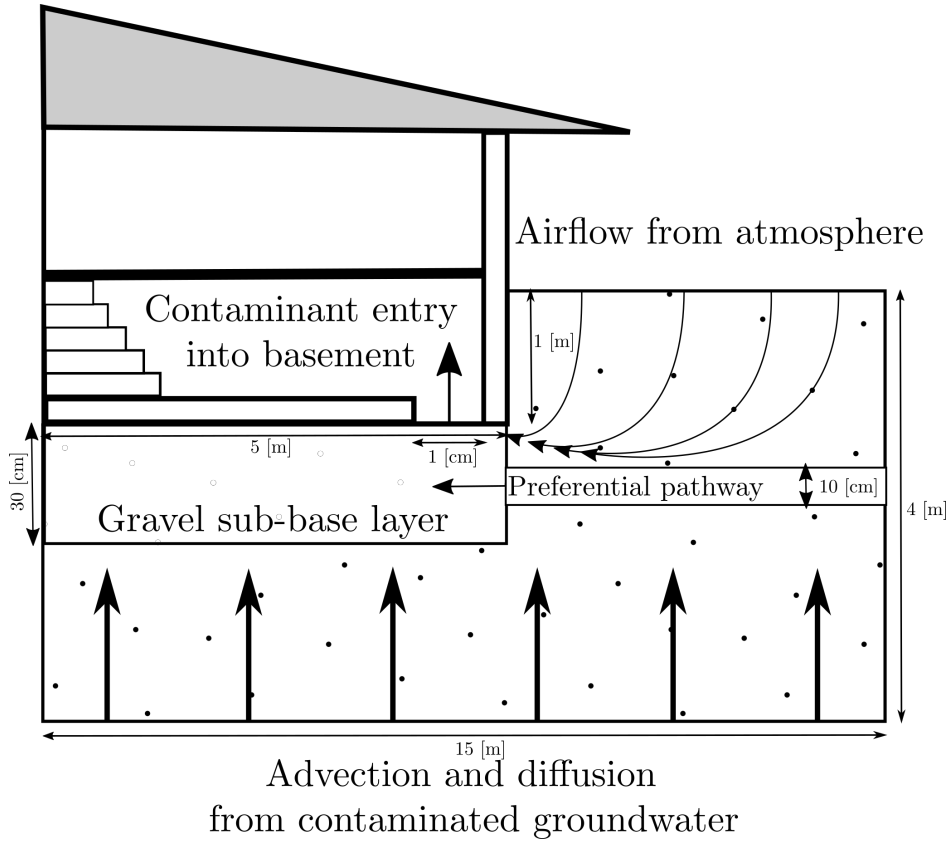


Figure 3.8: The modeled preferential pathway VI scenario.

the case at the ASU house[23]. Figure 3.8 shows the described scenario.

### 3.3.1 Geometry And Mesh

Explicitly modeling the entire preferential pathway in detail would require a significant number of elements with little gain; contaminant vapor transport in the pathway itself is not of great interest. To save computational resources only the exit of the pipe was modeled as a 10 cm diameter circle representing the boundary between pipe and gravel.

With the addition of the preferential pathway pipe, now only one plane of symmetry exists instead of two, and it becomes necessary to model half of the domain model geometry instead of just a quarter of it as in Chapter 2. On the scale of Figure 3.9, the area around the exit of the preferential pathway is barely visible as a darker cluster or mesh nodes in the lower left side of the cutout representing the foundation.

The meshing of the model follows the steps detailed in Chapter 2, with the addition that a boundary layer mesh is generated on the preferential pathway exit plane. A similar initial mesh is generated as earlier, including subsequent adaptive mesh refinement. Figure 3.9 shows the resulting meshed geometry.

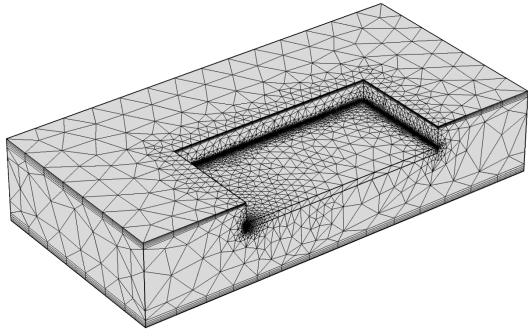


Figure 3.9: Meshed geometry of the preferential pathway model. Notice the gravel sub-base layer and the preferential pathway exit near the left hand foundation crack.

### 3.3.2 Physics And Boundary Conditions

In this model, we use the same governing equations introduced in Chapter 2, and they are only included here for completeness. However, to simulate the preferential pathway, it is necessary to supply two new boundary conditions - one related to the airflow from the pipe, and another for the contaminant transport, which are discussed in their respective section below.

## Indoor Environment

The indoor environment is still modeled using:

$$V_{\text{bldg}} \frac{\partial c_{\text{in}}}{\partial t} = n_{\text{ck}} - V_{\text{bldg}} A_e c_{\text{in}}$$

$$n_{\text{ck}} = \int_{A_{\text{ck}}} j_{\text{ck}} dA$$

$$j_{\text{ck}} = \begin{cases} u_{\text{ck}} c_g - \frac{D_{\text{air}}}{L_{\text{slab}}} (c_{\text{in}} - c_g) & u_{\text{ck}} \geq 0 \\ u_{\text{ck}} c_{\text{in}} - \frac{D_{\text{air}}}{L_{\text{slab}}} (c_{\text{in}} - c_g) & u_{\text{ck}} < 0 \end{cases}$$

$c_{\text{in}}$  [mol m<sup>-3</sup>] is the indoor contaminant concentration;  $n_{\text{ck}}$  [mol s<sup>-1</sup>] is the contaminant entry rate into the building via the foundation crack;  $A_{\text{ck}}$  [m<sup>2</sup>] is the foundation crack boundary area;  $A_e = 0.5 \text{ h}^{-1}$  is the air exchange rate;  $V_{\text{bldg}} = 300 \text{ m}^3$  is the volume of the house basement.  $D_{\text{air}} = 7.2 \times 10^{-6} \text{ m}^2 \text{s}^{-1}$  is the diffusion coefficient of TCE in air;  $u_{\text{ck}}$  [m s<sup>-1</sup>] is the airflow velocity through the foundation crack;  $L_{\text{slab}} = 15 \text{ cm}$  is the thickness of the foundation slab; and  $c_g$  [mol m<sup>-3</sup>] is the contaminant gas-phase concentration at the foundation crack boundary.

## Soil Moisture

Soil moisture content is determined using van Genuchten's retention model. We use two "soil" types in this model - gravel and sandy clay; their parameters and constants are shown

in Table B.1.

$$\begin{aligned} \text{Se} &= \begin{cases} \frac{1}{(1+(\alpha|h|)^n)^m} & h < 0 \\ 1 & h \geq 0 \end{cases} \\ \theta_w &= \begin{cases} \theta_r + \text{Se}(\theta_t - \theta_r) & h < 0 \\ \theta_t & h \geq 0 \end{cases} \\ k_r &= \begin{cases} (1 - \text{Se})^l (1 - \text{Se}^{\frac{1}{m}})^{2m} & h < 0 \\ 0 & h \geq 0 \end{cases} \\ \theta_g &= \theta_t - \theta_w \end{aligned}$$

$h$  [m] is the elevation above the groundwater interface; Se is the saturation;  $\alpha$ ,  $m$ ,  $n = \frac{1}{1-m}$ ,  $l = 0.5$  are the van Genuchten parameters;  $\theta_w$  is the water filled porosity;  $\theta_g$  is the gas filled porosity;  $\theta_t$  is the soil porosity;  $\theta_r$  is the residual moisture content. and  $k_r$  is the relative permeability for air;

## Soil Airflow

Airflow is still modeled using our modified Darcy's Law expression.

$$\frac{\partial}{\partial t}(\rho\theta_g) + \nabla \cdot \rho \left( -\frac{k_r \kappa}{\mu} \nabla p \right) = 0$$

$\vec{u}$  [ $\text{m s}^{-1}$ ] is the airflow velocity vector;  $\kappa$  [ $\text{m}^2$ ] is the permeability of the porous medium;  $\mu$  [ $\text{Pas}$ ] is the dynamic viscosity of the fluid;  $\nabla p$  [ $\text{Pa m}^{-1}$ ] is the pressure gradient;  $\theta_g$  is the gas-filled porosity of the soil;  $\rho = 1.225 \text{ kg m}^{-3}$  is the density of air; and  $\mu = 18.5 \times 10^{-6} \text{ Pas}$  is the dynamic viscosity of air. For steady-state cases, the first term is of course zero.

**Boundary conditions** Since the preferential pathway is assumed to be an open pipe, we assume it acts like a pressure gauge, and is at the reference ambient atmospheric pressure.

Ground surface	$p = 0 \text{ Pa}$
Preferential pathway exit	$p = 0 \text{ Pa}$
Foundation crack	$p = p_{\text{in/out}} \text{ Pa}$
Remaining boundaries	$-\vec{n} \cdot \rho \vec{u} = 0$ , i.e. no flow.

$p_{\text{in/out}}$  is not specified here as we will parametrically choose values for it.

## Soil Contaminant Transport

The contaminant transport in the soil is governed by:

$$(\theta_w + \theta_g K_H) \frac{\partial c_w}{\partial t} = \nabla \cdot (D_{\text{eff}} \nabla c_w) - K_H \vec{u}_g \cdot \nabla c_w$$

$c_w$  and  $c_g$  [ $\text{mol m}^{-3}$ ] are the contaminant concentrations in water and gas respectively;  $K_H = 0.402$  is the dimensionless Henry's Law constant for TCE at  $20^\circ\text{C}$ ;  $\vec{u}_g$  [ $\text{m s}^{-1}$ ] is the Darcy's velocity field; and  $D_{\text{eff}}$  [ $\text{m}^2 \text{s}^{-1}$ ] is the effective diffusivity of the contaminant according to Millington-Quirks model:

$$D_{\text{eff}} = \left( D_w \frac{\theta_w^{10/3}}{\theta_t^2} + D_g \frac{\theta_g^{10/3}}{\theta_t^2} K_H \right)$$

$D_w = 1.02 \times 10^{-9} \text{ m}^2 \text{s}^{-1}$  and  $D_g = 6.87 \times 10^{-6} \text{ m}^2 \text{s}^{-1}$  are the diffusion coefficient of TCE in water and air respectively. Again,  $\frac{\partial c_w}{\partial t} = 0$  for steady-state cases.

**Boundary conditions** The air in the pipe is assumed to be contaminated with TCE at a vapor concentration  $c_g$  in equilibrium with the groundwater source contaminant concentration. This assumption is based on contaminant samples taken from a manhole near the ASU house[70] which demonstrated that contaminant vapor concentrations in the nearby sewer

were of similar magnitude as the contaminated groundwater source.

Atmosphere	$c_w = 0 \text{ mol m}^{-3}$
Groundwater	$c_w = c_{gw} \text{ mol m}^{-3}$
Preferential pathway	$c_g = c_{gw} K_H \text{ mol m}^{-3}$
Foundation crack	$-\vec{n} \cdot \vec{N} = -j_{ck} \text{ mol m}^{-2} \text{ s}^{-1}$
All other	$-\vec{n} \cdot \vec{N} = 0 \text{ mol m}^{-2} \text{ s}^{-1}$ , i.e. no contaminant flux.

Note that we are neglecting any sorption in the soil, i.e. the sorption partitioning coefficient  $K_p = 0 \text{ m}^3 \text{ kg}^{-1}$ , and this term does not enter in a steady-state analysis in any case. We will likewise normalize all concentrations to the source concentration  $c_{gw}$ , and any arbitrary value can be assigned.

### 3.4 Temporal Variability And Preferential Pathways

In the calculation results shown in Figure 3.10, a preferential pathway is assumed to provide air containing contaminant vapor at a concentration equivalent to the vapor in equilibrium with the underlying groundwater source. This shows the true importance of the preferential pathway - it brings contaminated vapors directly to the sub-slab without attenuation in concentration associated with diffusion through soil.

Here, the indoor air exchange rate  $A_e$  was assumed to be a constant 0.5 per hour, and  $p_{\text{in/out}}$  was varied from -5 to 5 Pa. Values of predicted indoor air contaminant concentrations,  $c_{\text{in}}$  were obtained from steady state calculations. The predicted  $c_{\text{in}}$  values were then normalized by the assumed vapor concentration in equilibrium with groundwater  $c_{gw}$ , giving the attenuation from groundwater  $\alpha_{gw}$ . The predicted values of  $\alpha_{gw}$  as a function of  $p_{\text{in/out}}$  are given by the solid line Figure 3.10. These predicted values are compared to actual measured  $\alpha_{gw}$  values from the ASU House for the period during which the preferential pathway was

open given by the blue points.

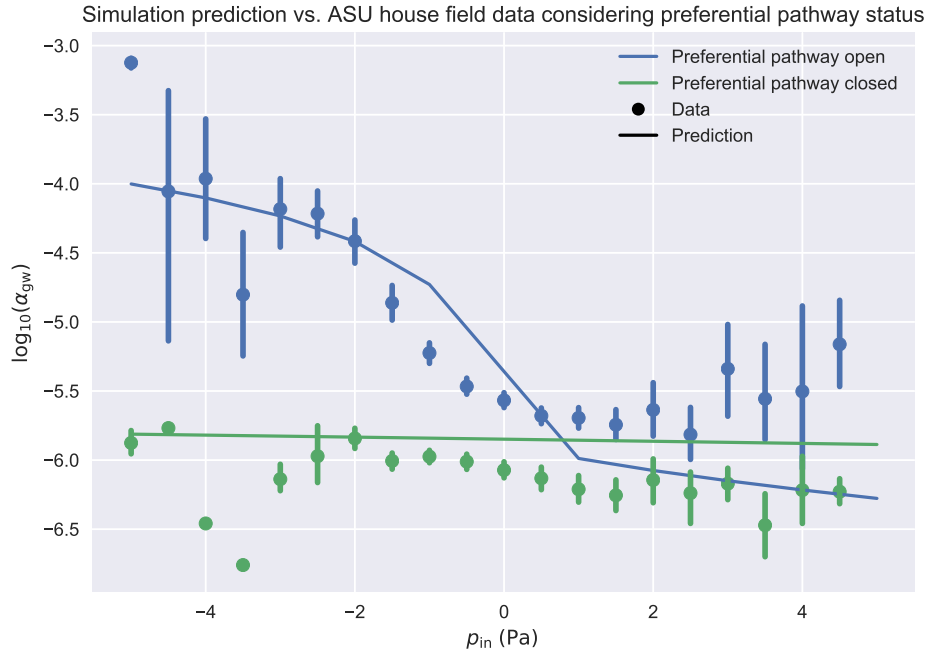


Figure 3.10: Model predicted indoor air concentration (as groundwater attenuation) compared to values recorded at the ASU house. The modeling results are given the solid lines and data by the dots. Blue here represents data before the closing of the preferential pathway and modeling result from the corresponding model, i.e. the model features a preferential pathway and a gravel sub-base. The green color signifies data from the period after the closing of the preferential pathway with the corresponding model, i.e. the preferential pathway is removed but the gravel sub-base remains. Here the data is placed in 20 equally spaced bin, i.e. not equally sized. The dot is the mean value and the error bars represent the 95% confidence intervals.

While the intent was not to exactly model all details of the ASU house, the model captures key details such as house footprint size, crack entry size, existence of a gravel sub-base, and a "land drain". The model successfully predicts the observed trends in  $\alpha_{gw}$  as  $p_{in/out}$  decreases (increased depressurization) but somewhat underpredicts  $\alpha_{gw}$  as the house is overpressurized. Most significantly, the model captures that even for a small increase in depressurization (0 to -5 Pa) a very large increase in  $\alpha_{gw}$  (two order of magnitude) can occur.

The model is also able to capture the weak trend in  $\alpha_{gw}$  with  $p_{in/out}$  when a preferential pathway is absent, but when there still exists a permeable subslab region. These results are

given by the green line in Figure 3.10. These results are again in agreement with what was observed at the ASU House when the preferential pathway was closed, i.e. that there was a much more modest variation in indoor air concentration, irrespective of pressure, when the preferential pathway was cut off.

The model corroborates the significant contribution that such a preferential pathway may have at a VI site. The preferential pathway acts not only as a source of contaminant vapor, but also as a source of air to the subslab. Because of the large resistance to soil gas flow in the surrounding soil, having a local source of air to support the increase of advective flow into the structure from the subslab region makes a large difference. (This will be examined below). While there obviously is still some variability unaccounted for, as indicated by the error bars on the actual field data in Figure 3.10, we can say with some confidence that the model is able to capture the general influence of a preferential pathway. This invites us exploring some of the factors that help explore more of the variability. Using our model, we rerun the scenarios, but this time consider two more cases:

1. We remove the gravel sub-base layer but keep the preferential pathway.
2. We keep the gravel sub-base layer, but remove contaminant vapor from the preferential pathway, i.e. it supplies only "clean" air.

The results of running these cases can be seen in Figure 3.11.

Here the original modeling results and associated data from the period before the closing of the preferential pathway are again given by blue points and curve. The case corresponding to the removal of contaminant vapors from the preferential pathway is shown by the green line, while the removal of the gravel sub-base care is shown by red.

The removal of contaminant vapors from the preferential pathway largely eliminates the significant dependence of  $\alpha_{gw}$  on  $p_{in}$  as shown earlier by blue in Figure 3.10 (see the green curve). However, the increase in indoor air concentration with decreased indoor pressure is smaller than when the preferential pathway was present. This shows that a preferential

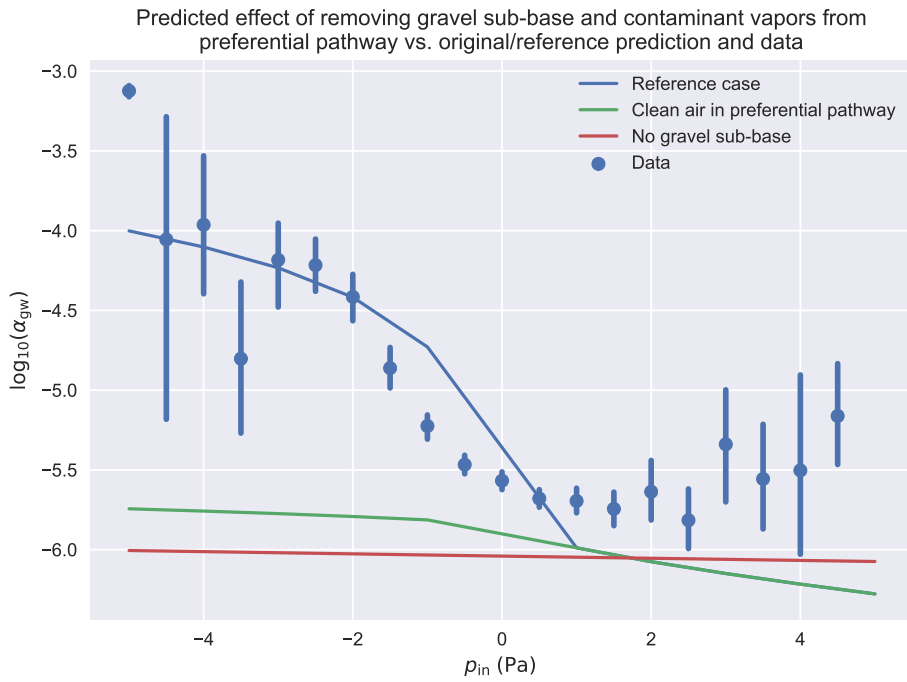


Figure 3.11: How different cases affect the predicted impact of the preferential pathway.

pathway similar to the one found at the ASU house does two things.

First, it provides a preferential source of air, and the depressurized building is able to much easier draw air from the preferential pathway than the surrounding soil; the soil offers a huge resistance to airflow and thus advective transport critical to contaminant entry. Second, the increase in "advective potential" alone is inadequate to cause the large effect as observed at the ASU house, and a preferential source of contaminant vapors is also required - two conditions that were fulfilled at the ASU house.

The removal of the gravel sub-base likewise also has a significant effect on the modeling results. Without it the full potential of a preferential pathway is unrealized (see the red curve). This can again be understood because of the significant resistance to contaminant transport that soils present. This adds a third condition for a preferential pathway to exert a significant influence - a medium for effective communication between the preferential pathway and indoor environment is necessary.

The importance of advective transport can be shown by analyzing the Péclet number

for transport through the foundation crack. The Péclet number is a dimensionless number defined as the ratio of advective to diffusive transport rate across some characteristic length, i.e. it tell us if transport is advective or diffusion dominated. For transport of contaminants through the foundation crack we define this as

$$\text{Pe} = \frac{\text{advection}}{\text{diffusion}} = \frac{u_{\text{ck}} L_{\text{slab}}}{D_g} \quad (3.1)$$

here  $u_{\text{ck}}$  [ $\text{m s}^{-1}$ ] is the airflow velocity across (through) the crack  $L_{\text{slab}} = 15 \text{ cm}$  is the thickness of the foundation slab, i.e. the characteristic length for transport; and  $D_g = 6.87 \times 10^{-6} \text{ m}^2 \text{ s}^{-1}$  is the diffusivity of TCE in air.

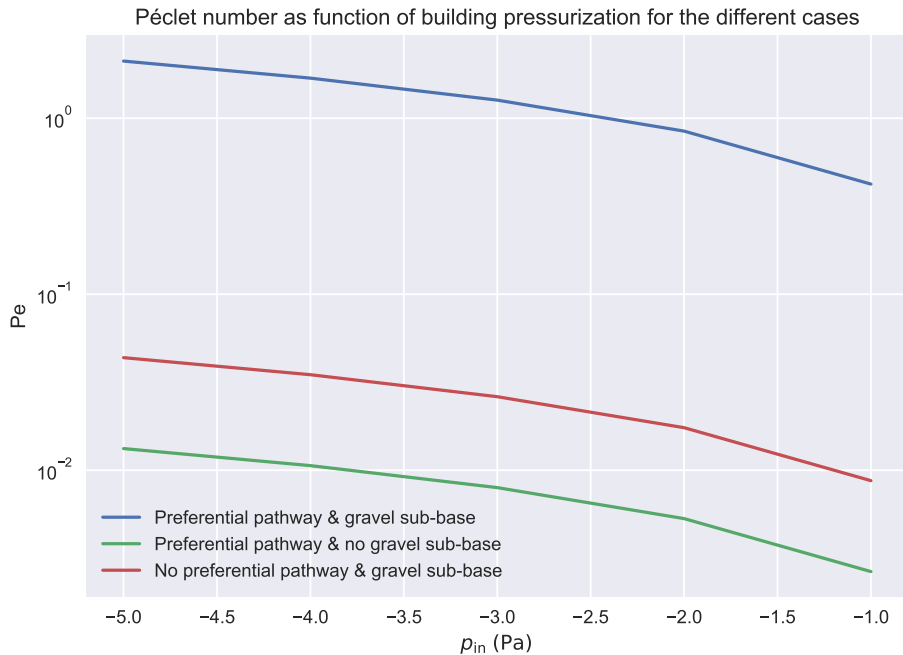


Figure 3.12: Péclet number for transport through the foundation crack of our modeled house as a function of building pressurization. Here we consider three cases where the preferential pathway and gravel sub-base are present/absent, which shows the dramatic effect these site features can have on contaminant transport at a VI site.

The values of Pe characterize transport as:

$Pe \gg 1$	Advection dominated
$Pe \ll 1$	Diffusion dominated
$Pe = 1$	Advection and diffusion equal

Figure 3.12 shows the Péclet number for three of the modeled cases:

1. Preferential pathway and gravel sub-base layer present
2. Preferential pathway present but gravel sub-base layer absent
3. Preferential pathway absent but gravel sub-base layer present

Note that the cases when  $p_{in} > 0$  Pa are not shown. By our definition  $u_{ck} > 0$  indicates airflow into the house, giving  $Pe > 0$ . This figure shows that it is only when there is a combination of a preferential pathway and a gravel sub-base layer that advective transport is able to dominate; diffusive transport dominates for the other cases which explains the weak correlation between  $\alpha_{gw}$  and  $p_{in}$  in Figure 3.11 when the preferential pathway was removed. The rate of diffusion of TCE in air does not depend upon  $p_{in}$ . Likewise it explains the dramatic increase of  $\alpha_{gw}$  as  $p_{in}$  decreases when the gravel sub-base and preferential pathway were present, as advective transport only starts to dominate after  $p_{in} < -2.5$  Pa.

To summarize, for a preferential pathway to have a significant influence at a VI site, the following conditions need to be fulfilled:

1. A preferential source of air is required to enhance the advective transport potential at the site.
2. Contaminant vapors must likewise be preferentially supplied.
3. There needs to exist a medium to facilitate effective communication between the preferential pathway and the indoor environment.

While this may seem like some specific conditions to be fulfilled for a preferential pathway to be so impactful, it can easily be generalized to other scenarios. For instance, one could easily imagine a situation where a house has a gravel backfill surrounding it, with some other subsurface source - like a leaky sewer pipe (that does not exit anywhere the building). Under such a circumstance, one could conceivably observe a similar effect in the indoor contaminant concentration caused by a very different scenario.

### 3.4.1 Role Of Air Exchange Rate

Simulations so far has assumed that the indoor air exchange rate is at a constant  $0.5 \text{ h}^{-1}$  irrespective of the house pressurization. This is not quite realistic, as air exchange rates are constantly fluctuating, and this will have an impact on indoor contaminant concentrations. To account for this, we rerun our model simulations, but this time assuming different air exchange rate values, and determine if this can capture some more of the observed variability.

Ideally, we would wish to be able to determine air exchange rate based on site conditions, and in particular building pressurization. Determining air exchange rate exactly is difficult, as it is influenced by building pressurization, indoor/outdoor temperature differences, wind, operation of HVAC systems, etc. This is a topic that will be expanded on in Chapter 4.

Designed air exchange rates are often legally regulated as part of local building ordinances, and depending on the type of building, its values and bounds are usually more or less known. Here, we will rerun the model and assume a wide range of constant air exchange rate values. At the ASU house, air exchange rates were measured using a tracer-gas study, and the the 10th, 50th, and 90th percentile air exchange rate values are shown in Table 3.1. Also shown are the corresponding values from the EPA duplex, and those from an independent EPA study that measured air exchange rates nationwide. Based on this we rerun the model using air exchange values of 0.1, 0.5, and  $0.9 \text{ h}^{-1}$ .

Figure 3.13 shows the result of incorporating a wider range of air exchange rates when predicting  $\alpha_{\text{gw}}$ . Here the central lines are the result corresponding to  $A_e = 0.5 \text{ h}^{-1}$ , while the

	Percentile		
	10th	50th	90th
EPA study[71, 72]	0.16-0.2	0.35-0.49	1.21-1.49
ASU house[24, 23]	0.21	0.43	0.78
EPA duplex[65]	0.34	0.74	1.27

Table 3.1: Air exchange rate values [ $\text{h}^{-1}$ ]

upper and lower bounds of each shaded area correspond to  $A_e = 0.1$  and  $0.9 \text{ h}^{-1}$  respectively. The shaded area cover much of the confidence interval of  $\alpha_{\text{gw}}$  as a function of  $p_{\text{in}}$ . This indicates that much of the uncertainty of numerically determining  $\alpha_{\text{gw}}$  could be accounted for by considering the range of air exchange values at a site.

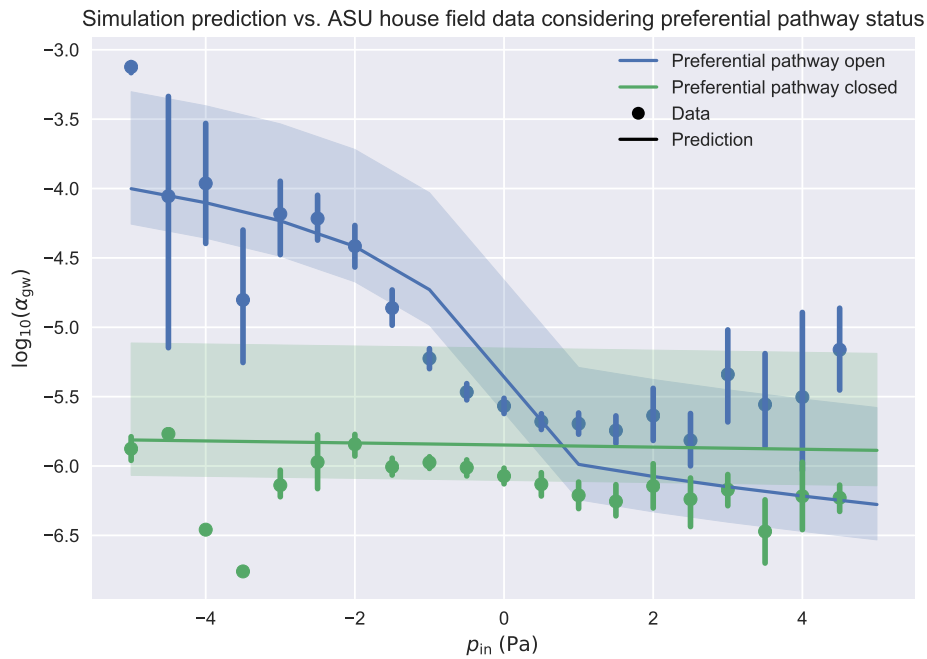


Figure 3.13: Modeling result from Figure 3.10 but with added shaded area to demonstrate the effect of assuming different air exchange values. The central lines are the result corresponding to  $A_e = 0.5 \text{ h}^{-1}$ , while the upper and lower bounds of each shaded area correspond to  $A_e = 0.1$  and  $0.9 \text{ h}^{-1}$  respectively.

The fact that indoor air pressure and air exchange rate can both vary is applied to a transient simulation, where we model a "typical" day at the ASU house by using the median diurnal variation of  $p_{\text{in}}$  and  $A_e$  as model inputs. We consider our model with and without

the preferential pathway present. Specifically, we use the median diurnal values of  $p_{in}$  and  $A_e$  at one hour intervals over a 24-hour period and interpolate using cubic splines between these for continuity. This is compared to a case where we only use the median diurnal values of  $p_{in}$  but keep  $A = 0.5 \text{ h}^{-1}$  constant. Now the transient terms neglected at steady-state will be included.

Figure 3.14 shows how  $\alpha_{gw}$  varies throughout this hypothetical "typical" day. Here we see that when the preferential pathway is present, variability of  $\alpha_{gw}$  is mostly driven by fluctuations in contaminant entry rate; the variable and constant air exchange rate cases do not differ much from each other. When the preferential pathway is absent, then there is no variability of  $\alpha_{gw}$  unless the air exchange rate is fluctuating.

To quantify the predicted variability of  $\alpha_{gw}$  we define ratio between the minimum and maximum  $\alpha_{gw}$  as

$$\Delta_{\max} = \frac{\alpha_{gw,\max}}{\alpha_{gw,\min}} \quad (3.2)$$

Applying this to the cases where air exchange rate is varied, and the preferential pathway present/absent we find that these ratios are  $\Delta_{\max} = 5.09$  and  $\Delta_{\max} = 1.68$  respectively. I.e.  $\alpha_{gw}$  may be expected to vary around half an order of magnitude at a site characterized by a preferential pathway under our considered conditions, whereas one where there is no preferential pathway may vary by a factor of 1.68.

These "maximum daily variability"  $\Delta_{\max}$  values can be compared to those at the ASU house. Indoor contaminant concentration samples at the ASU house were collected roughly every four hours across the study period. By excluding the CPM period, and then resampling these data on a daily basis, we can find  $\Delta_{\max}$  for each day. These data are further separated to consider the period before and after the land drain preferential pathway was closed. The period before the preferential pathway was closed then includes 441 days or data points, giving a median value  $\Delta_{\max} = 2.33$ . For the period after the preferential pathway was closed, we get 181 days of data, giving a median value of  $\Delta_{\max} = 1.60$ . Thus, we can see that we somewhat overpredicted the expected variability for the period when the preferential

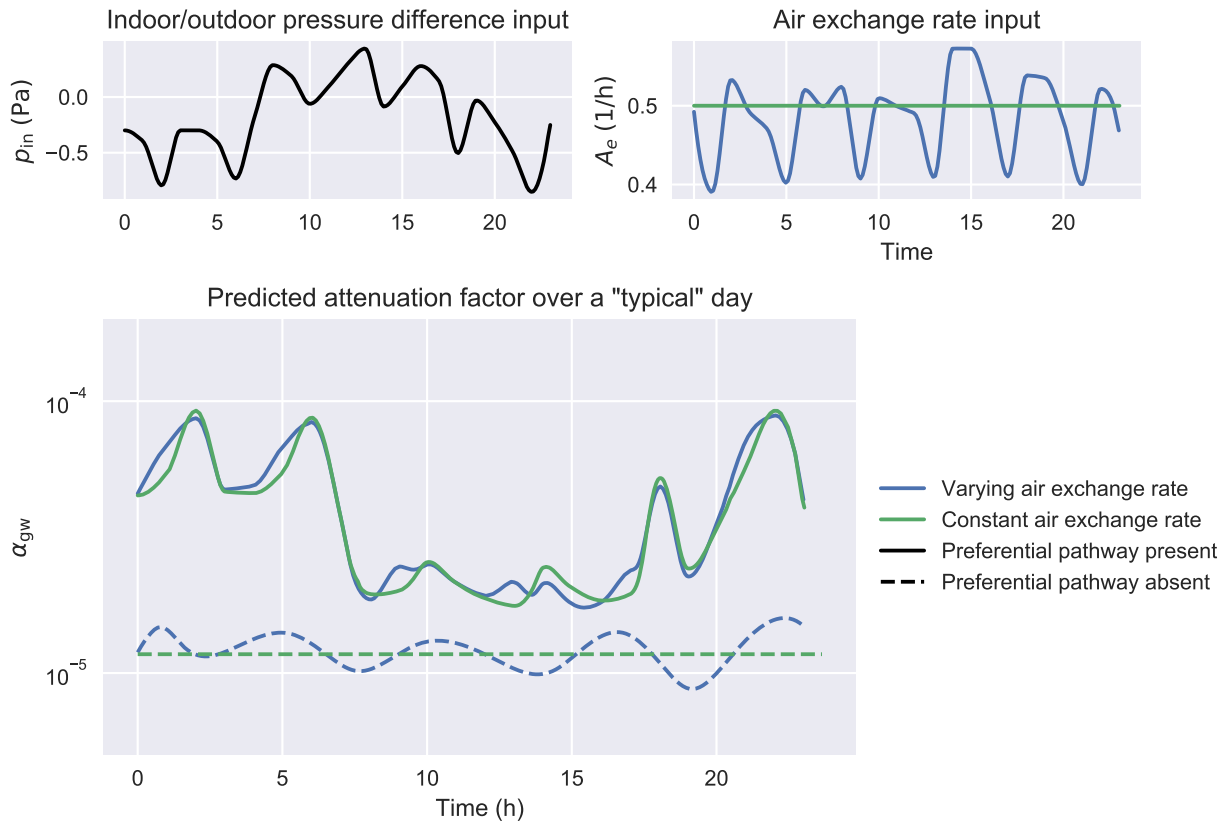


Figure 3.14: Modeled indoor contaminant concentration (as attenuation from groundwater) over a "typical" day. Here the hourly median indoor/outdoor pressure difference and air exchange rates recorded at the ASU house, as well as a comparison case where a constant air exchange rate of  $0.5 \text{ h}^{-1}$  is assumed, are used as model input parameters. For these we consider two models cases; one where a preferential pathway is present, and another in which it is absent respectively.

pathway was open, but were quite close when it was closed.

This indicates that for sites that are characterized by diffusive transport, much of the observed variability of indoor contaminant concentrations are driven by fluctuations in air exchange rate. For sites dominated by advective transport, fluctuations in building pressurization, and consequently contaminant entry, are more important drivers for temporal variability of  $\alpha_{gw}$ .

## 3.5 Soil-Gas Spatial Variability And Preferential Pathways

Preferential pathways can have a significant impact on spatial variability of contaminant vapors at a site. This can manifest inside a house itself, as large concentration differences between rooms, as was the case due to a leaky bathroom plumbing fixture in the work by Pennell et al.[21]; contaminant concentration was significantly higher in the upstairs bathroom than the basement, where higher concentrations are usually expected. This was an example of yet a different preferential pathway effect than those modeled here, because it was associated with the failure of a trap on a sewer line. Spatial variability in contaminant concentration can also manifest in the subsurface, which can be caused by a contaminant source[73], the building itself[16], or as we will explore here - a subsurface preferential pathway.

### 3.5.1 ASU House

Guo et al.[23] explored the role that the ASU house land drain preferential pathway had on the spatial variability of contaminant vapors in the subsurface, and in particular in the gravel sub-base. They used Kriging interpolation (discussed further below) to visualize the distribution of subsurface contaminant vapors using their collected subsurface contaminant vapor samples. One snapshot of this work can be seen in Figure 3.15 where it clearly visible how the preferential pathway dramatically increased the contaminant vapor concentration in one half of the gravel sub-base layer - the half where the land drain preferential pathway exit was located.

While this demonstrates the influence of a preferential pathway on subsurface spatial variability, it can be quantitatively explored just how significant it can be. To do this, we

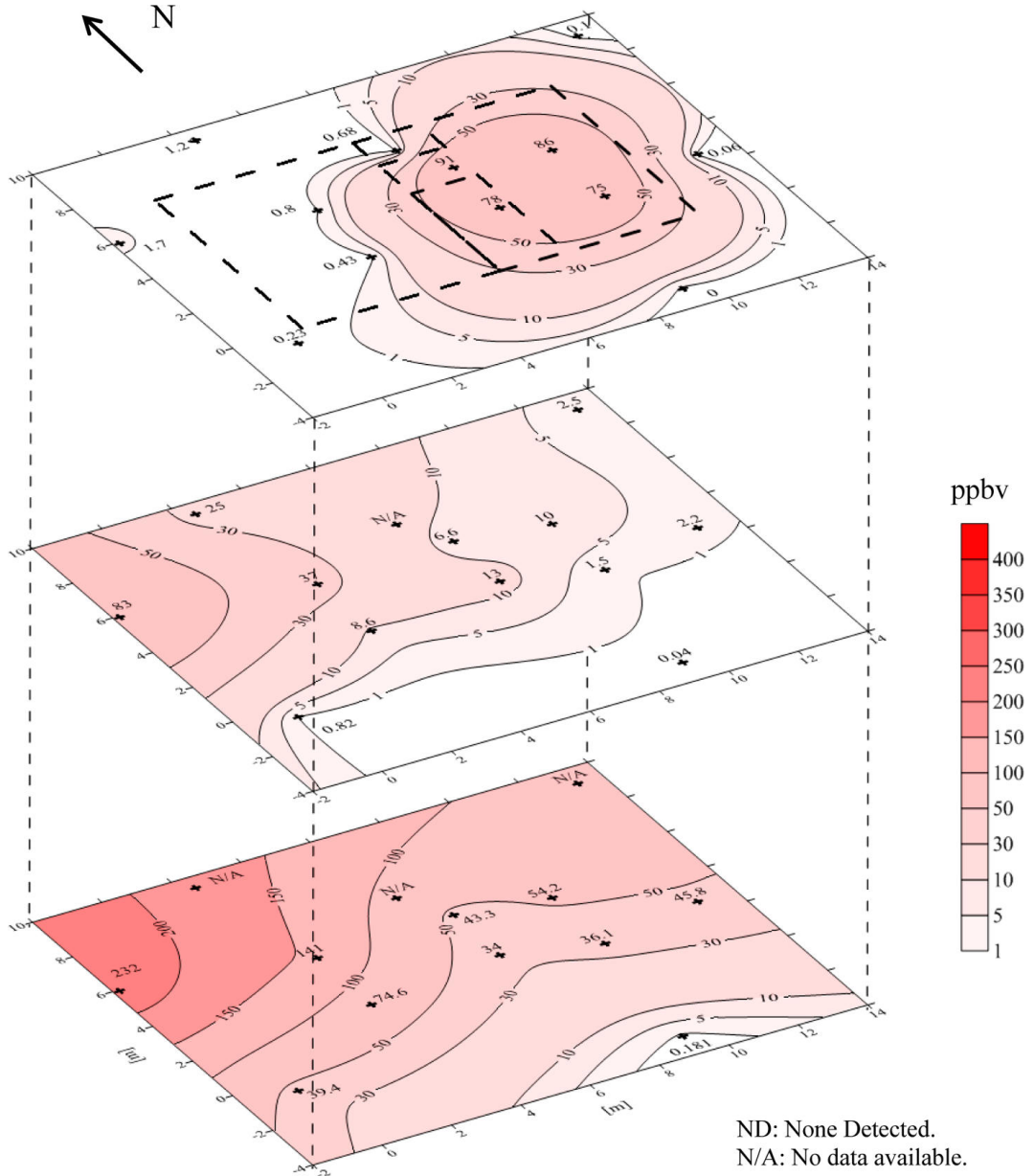


Figure 3.15: Distribution of TCE contaminant vapors in the subsurface underneath the ASU house. The top layer is right beneath the foundation, with the two subsequent at 0.9 m and 1.8 m below the foundation slab. Snapshot from the period when the CPM system was active. Figure from Guo et al.[23].

consider the attenuation from the sub-slab region to the indoor environment

$$\alpha_{\text{subslab}} = \frac{c_{\text{in}}}{c_{\text{subslab},5}} \quad (3.3)$$

using sub-slab vapor contaminant concentration data from location 5 of the ASU house (see

Figure 3.2b). This was the sample location closest to exit of the land drain preferential pathway. These data are visualized in a boxplot in Figure 3.16 where we consider the effects of CPM and the land drain preferential pathway on  $\alpha_{\text{subslab}}$ .

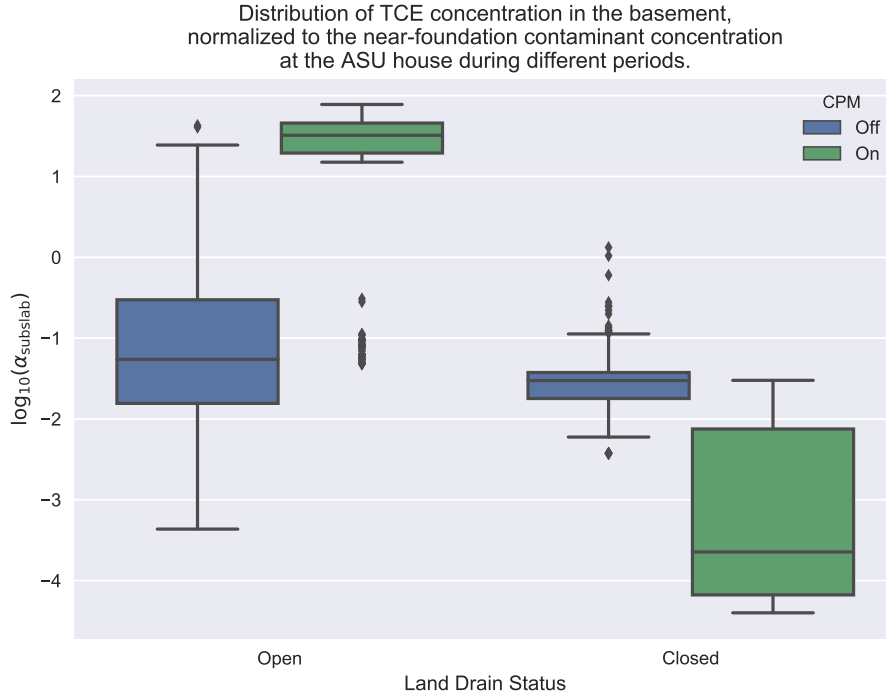


Figure 3.16: Boxplot showing the distribution of  $\alpha_{\text{subslab}}$  considering the effects of CPM and the ASU house land drain preferential pathway. Here  $\alpha_{\text{subslab}}$  is the attenuation from sub-slab sampling location 5 to the indoor environment. The box signifies the interquartile range (IQR) of values, with the central line representing the median value, and the top and bottom of the box are the 25th and 75th percentiles. The whiskers extend to 1.5 times the IQR. Markers indicate outlier data points that fall outside the whiskers.

Here we observe that when the preferential pathway was open and the CPM system active,  $\alpha_{\text{subslab}}$  usually exceeded unity by at least an order of magnitude, a situation that seemingly violates the expected concentration gradient from outside to indoors; we can likewise see that this is an observed occurrence when the preferential pathway was open but the CPM system inactive. Normally, one would not expect  $\alpha_{\text{subslab}}$  to be even of the order of unity. Examining the  $\alpha_{\text{subslab}}$  data from the period after the preferential pathway was closed, as well as  $\alpha_{\text{subslab}}$  data collected by the EPA in their VI database,  $\alpha_{\text{subslab}}$  would be expected to range from  $1 \times 10^{-3}$  to  $1 \times 10^{-1}$  with  $3 \times 10^{-2}$  a commonly encountered value[7]. In other words, the

process of transport from subslab to indoor involves a substantial concentration gradient. When  $\alpha_{\text{subslab}} \geq 1$  this can be an indicator that even though location 5 is only 2 m away from the land drain preferential pathway exit, samples taken here may fail to capture the highest sub-slab contaminant concentrations; the highest contaminant vapor concentration in the subslab during the preferential pathway open period could have been order of magnitude higher than recorded. The complexity of the predicted  $\alpha_{\text{subslab}}$  that concentrations profiles in Figure 3.16 suggest that use of any single collected concentration value to characterize the whole subslab is very dangerous.

This highlights the large impact that a preferential pathway can have on subsurface spatial contaminant concentrations. However, another possibility for explaining such high  $\alpha_{\text{subslab}}$  values is that they may indicate that there are some indoor contaminant sources present. It was noted above that under certain circumstances, the flow of contaminant may reverse, and be in the direction from the house into the subslab. This was not however the situation at the ASU house. Nonetheless, this is another aspect of VI that investigators should be cognizant of high  $\alpha_{\text{subslab}}$  values (particularly those that are greater than unity) could indicate existence of an indoor source. This is why during an actual in-house VI investigation, there is always a great effort made to identify any possible indoor sources of the contaminant of concern, and often these are found in consumer products which are removed before VI sampling takes place.

### 3.5.2 EPA Duplex

The spatial variability of the soil-gas contaminant concentration at the EPA duplex is investigated by interpolating the recorded data using the kriging technique. Kriging is a commonly used technique in geostatistics where sparse spatial data can be interpolated over a larger spatial grid. This interpolation is performed by calculating the spatial covariance between the known data points, making assumptions of spatial data distribution model - defining a kernel, and then fitting parameters to these kernels[74].

Here, the interest is in the situation at the EPA duplex, for which such analysis has not yet been performed. The question to be answered is whether this analysis can shed more light on the temporal variability at that site- was a leaky preferential pathway injecting contaminant vapors into the soil adjacent the building? Soil-gas contaminant concentration data were collected at multiple locations and at multiple depths around the duplex. In Figure 3.5b we can see a number of ports labeled as SSP and SGP - these are the locations where soil-gas concentration data were collected. Using the length scale in Figure 3.5b, approximate  $x$  and  $y$  coordinates for the location of each sampling port were extracted from the figure, and the bottom left corner of the figure is defined as  $(x, y) = (0, 0)$ . In the publicly available EPA duplex database[69], the concentration of various contaminant at 5 different depths across time were recorded. These together form a large dataset containing soil-gas contaminant concentration, their spatial coordinates in three dimensions as a function of time.

Kriging generally works best if the input data are normally distributed, which soil-gas contaminant concentration data generally not. However, after a  $\log_{10}$  transformation of the concentration data they generally normally distributed. The kriging here was performed using the SciKit-learn Python package[75]. This requires input data, the data coordinates, a grid onto which data is to be interpolated onto, and a kernel.

A radial-basis function kernel, multiplied by a constant was chosen here, as it closely resembles the solution to the infinite domain diffusion equation.

$$k(\vec{x}_i, \vec{x}_j) = C \exp\left(-\frac{1}{2}d\left(\frac{\vec{x}_i}{l}, \frac{\vec{x}_j}{l}\right)\right) \quad (3.4)$$

$k$  is the kernel output value that determines the interpolated soil-gas concentration;  $\vec{x}_i, \vec{x}_j$  are the coordinates for some points  $i$  and  $j$ ;  $C$  is a constant that is determined by the software;  $d\left(\frac{\vec{x}_i}{l}, \frac{\vec{x}_j}{l}\right)$  is the distance between  $\vec{x}_i$  and  $\vec{x}_j$ , scaled by a length parameters  $l$ , which is determined by the software.

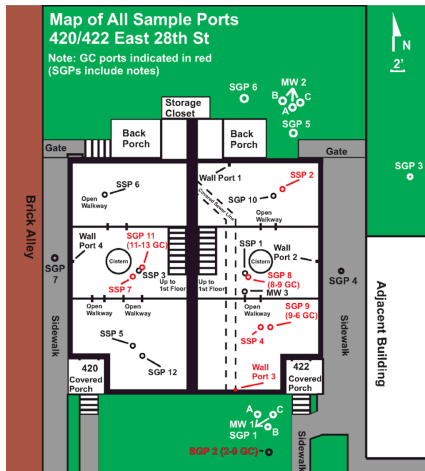
The results of the kriging process are plotted using Plotly[76] in Figure 3.17. It should

be noted that these are soil-gas contaminant concentrations each from a period that is (by inspection) determined to be relatively "representative" of the overall temporally separated dataset. In reality soil-gas contaminant concentrations fluctuate spatially in time, but there are some general trends that the analysis provides.

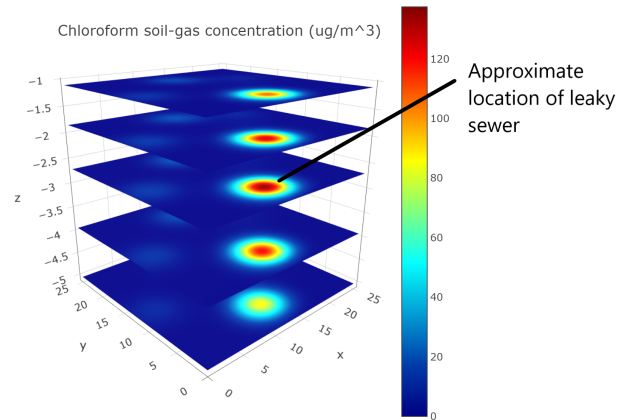
Figure 3.17 show how varied the soil-gas spatial variability for different contaminants can be. In particular, we see that trichloroethene (TCE) here exhibit relatively minor spatial variability compared to chloroform or tetrachloroethene (PCE). A likely explanation for this disparity is the role that the sewer played at this site.

In a later study of the EPA duplex, McHugh et al.[22] found that PCE and chloroform could be found throughout the sewer network in the neighborhood; this was not true of TCE. Looking again at PCE and chloroform in Figure 3.17, we see that there is often a "hot spot" in the middle slice, approximately at a depth of  $-2.75\text{ m}$ , roughly in the middle of the front lawn area. This is approximately the spot where the sewer line servicing the EPA duplex was located, which suggest that there was a leak in that vicinity. The leak in that particular area, and thus the sewer preferential pathway at the site, is likely what significantly contributes to much the soil-gas contaminant concentration spatial variability. This shows another way that a preferential pathways can the play a significant role at a VI site, and the importance of screening for them during a VI site investigation.

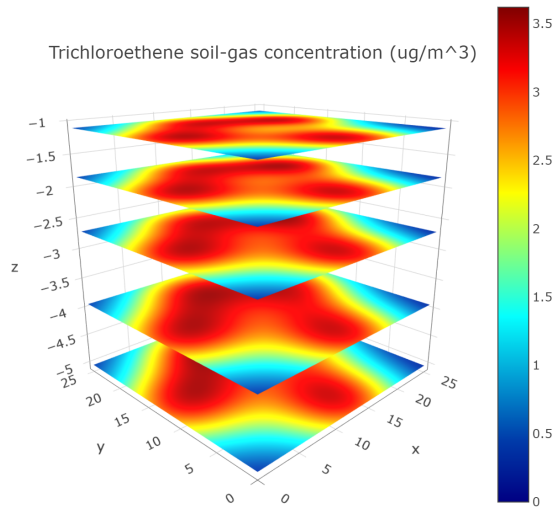
Unfortunately, at this site, there were no data taken that would reveal the temporal variability of the PCE and chloroform concentrations in the sewer. The kriging analysis merely gives some time-averaged pictures of the soil gas profiles adjacent to the house. The study by McHugh et al.[22] moreover offered a complicated picture of transport of these species in the sewer. Thus, unlike the situation at the ASU House, it would be difficult to build a reliable model of the influence of this particular preferential pathway on the indoor air concentrations. But what is clear is that in the presence of such a near-foundation source of contaminant vapors, the ordinary models of vapor transport from a groundwater source will also not apply.



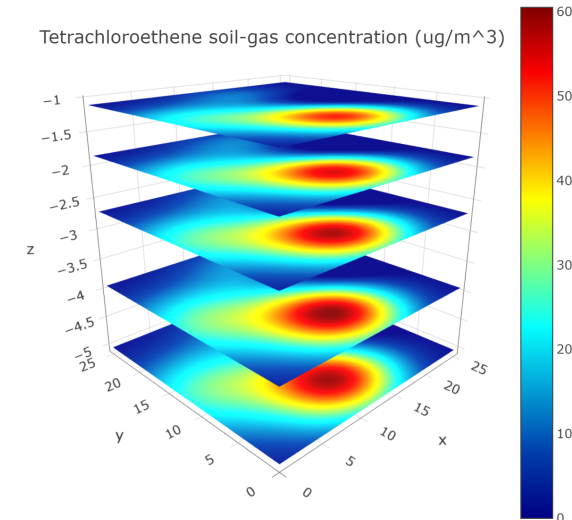
(a) Floorplan of the EPA duplex. The soil-gas figures  $x$  &  $y$  coordinates are relative to the bottom left corner.



(b) Soil-gas concentration of chloroform.



(c) Soil-gas concentration of TCE.



(d) Soil-gas concentration of PCE.

Figure 3.17: Interpolated soil-gas contaminant concentrations for select contaminant underneath the EPA duplex. Soil-gas concentrations profiles reveal a potential leak in the sewer line roughly underneath the EPA duplex front lawn.

# **Chapter 4**

## **The Significance of Foundation Entry Mechanism on Vapor Intrusion**

### **4.1 Summary**

This chapter explores the importance of dominant transport mechanism for contaminant vapors entry into a building. There are two commonly accepted mechanisms by which contaminants enter a building from the soil beneath it – advection and diffusion. In the case of advection, contaminant is carried into a building as a constituent of soil gas, which is swept into the building by a pressure gradient from soil to building interior. Such gradients need not be large and a few Pa can drive such a flow. On the other hand, if the interior of the structure is pressurized relative to the sub-foundation soil, then the advective flow will be out of the building. Regardless of the existence or direction of a pressure gradient, there generally exists a contaminant concentration gradient from soil into the structure, which means that there will always be a driving force for diffusive entry of the contaminant into the building. Only if the outward advective flow is high enough can this diffusive entry be overcome, and contaminant entry prevented. Advective transport is likely to only be dominant at VI site with some feature or pathway that allows facile delivery of air (soil-gas)

the entry point in the foundation. This is because there is generally a large resistance to transport of soil gas through the surrounding soil, bearing in mind that the pressure gradients available to drive any flows are normally quite small. It has been shown in previous modeling studies that for quite comparable levels of contaminant vapor beneath the foundation slab, very different indoor air contaminant concentrations may be encountered, depending upon the ability of the surrounding soil to allow significant advective flow[58, 35]. This fact emphasizes the importance in vapor intrusion investigations of identifying features that will allow significant advective flow from soil to the building interior. When advective entry is the dominant mode of contaminant entry into a building, use of building pressurization (in a controlled pressure method, (CPM) study) as an investigative tool is likely to offer more definitive results than when diffusive entry is dominant. The existence of an advective entry dominated scenario also may enable using weather (e.g., barometric pressure or wind) and temperature as predictors of building pressurization and from that, contaminant entry rates. Historically, the most widely held view of vapor intrusion has been that it is advective entry dominated, and indeed at many sites that is the case. But where this assumption does not hold can lead to confusion when interpreting results.

## 4.2 Advection Entry: Role of Soil and Foundation

The modeling in Chapter 3 help to explain why building pressurization influenced indoor air contaminant concentrations much more before the closing off of the sub-slab preferential pathway than after the closure. The existence of the preferential pathway allowed advective transport to be the dominant transport mechanism for entry of contaminant vapors through the foundation breach. This finding has wider implications for our understanding of the entry mechanics of VI.

It is commonly assumed that advective transport dominates in the near-foundation region and through breaches in the foundation itself, but our modeling of the situation at the ASU

house showed that this was mainly possible because:

1. The preferential pathway represented a source from where air could readily be drawn drawn into the subslab region.
2. The permeable gravel sub-base acted as a communication medium between the preferential air source and the building.

In other words, for advective transport to dominate through foundation cracks, some site-specific features were required. We showed that absent the preferential pathway, the soil surrounding the house itself presented too much resistance to air flow for this to be possible.

Only one soil type was explored in the modeling work in Chapter 3 - sandy clay. This kind of soil is a relatively impermeable soil, and other soil type are now considered. Furthermore, our modeled house featured a basement, and in such a scenario, the atmosphere is relatively far removed from the foundation breach, and thus it makes sense to also consider a slab-on-grade type of foundation.

The effect of different soil and foundation types is investigated using the model already introduced in Chapter 2. We consider 12 of the soil types defined by the EPA (see Table B.1) and for each of these we consider a basement and a slab-on-grade case respectively. The basement and slab-on-grade cases are defined by the bottom of a foundation slab located at 1 m and 15 cm bgs respectively. The building is assumed to be depressurized at  $p_{in} = -15 \text{ Pa}$ , a value somewhat greater than "normal", in order to enhance the advective entry potential. The analysis in Chapter 3 already showed that for the case of existence of a gravel sub-base layer, absent an air source supplied by a preferential pathway, results were was virtually indistinguishable from the cases where there was no gravel sub-base layer. I.e. a gravel sub-base will not be included in the model.

The results of the calculations will be shown in terms of the Péclet number for the modeled contaminant entry pathway. This Péclet number is defined as already shown before

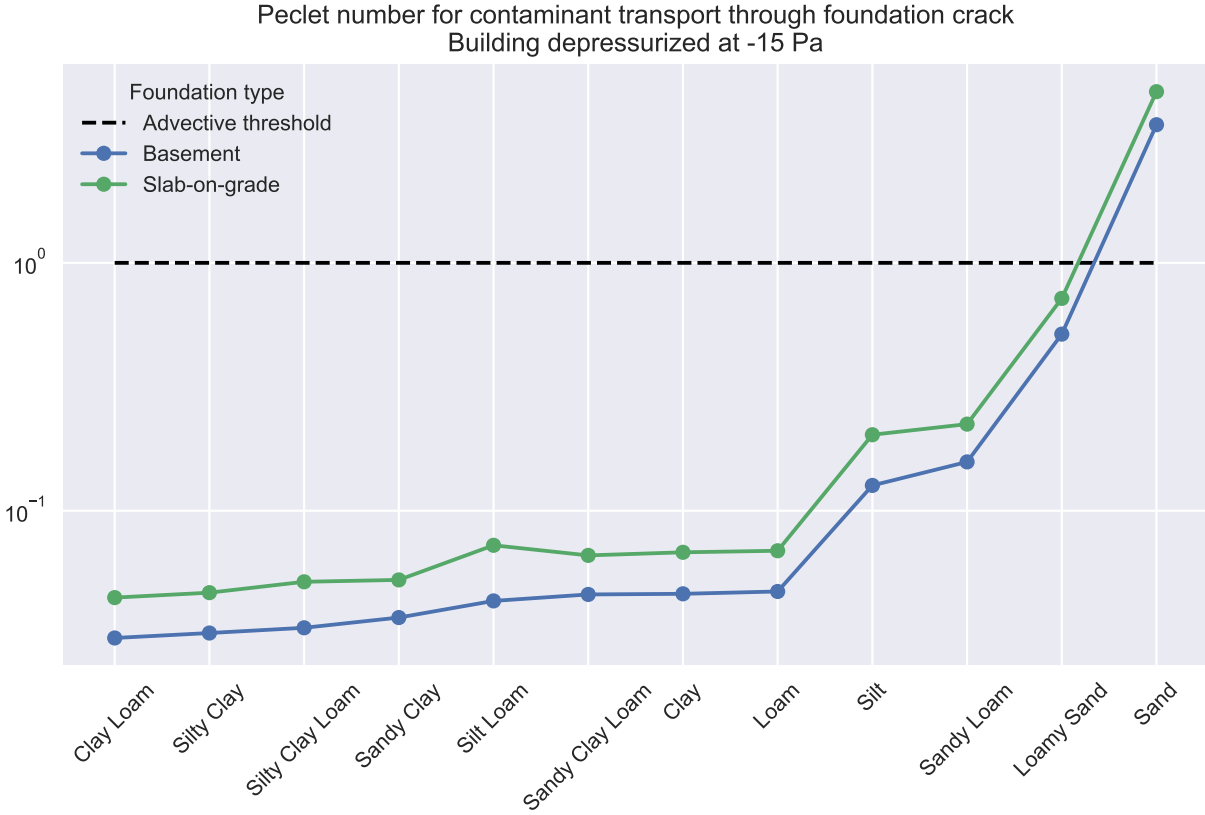


Figure 4.1: Predicted effect of soil and foundation type on the Péclet number of transport through the foundation crack. We consider the 12 different soils studied by the EPA (see Table), and for each of these we consider a house featuring a basement and a slab-on-grade house. The foundation slab is assumed to be 15 cm thick. In the basement case, the bottom of the foundation slab is assumed to be 1 m bgs and in the slab-on-grade case 15 cm bgs. The modeled building is assumed to be depressurized at  $-15 \text{ Pa}$ . The threshold where advective contaminant entry begins to overtake diffusive entry, i.e  $\text{Pe} = 1$ , is marked by the dashed line.

in equation (3.1) as:

$$\text{Pe} = \frac{\text{advection}}{\text{diffusion}} = \frac{u_{ck} L_{\text{slab}}}{D_g} \quad (4.1)$$

here  $u_{ck}$  [ $\text{m s}^{-1}$ ] is the airflow velocity across (through) the crack  $L_{\text{slab}} = 15 \text{ cm}$  is the thickness of the foundation slab, i.e. the characteristic length for transport; and  $D_g = 6.87 \times 10^{-6} \text{ m}^2 \text{s}^{-1}$  is the diffusivity of TCE in air.

The result of these model calculations are shown in Figure 4.1. These results shows that for most soil types, irrespective of whether a building has a basement or a slab-on-grade

foundation, the Péclet number across the foundation slab is actually not sufficiently high for advection to be the dominant entry mechanism; most soils are too impermeable for sufficient airflow to be pulled into the building by the small pressure gradient that exists between the building interior and the subsurface. Sites characterized by sandy soil are an exception to this, as they are permeable enough to sustain such airflows.

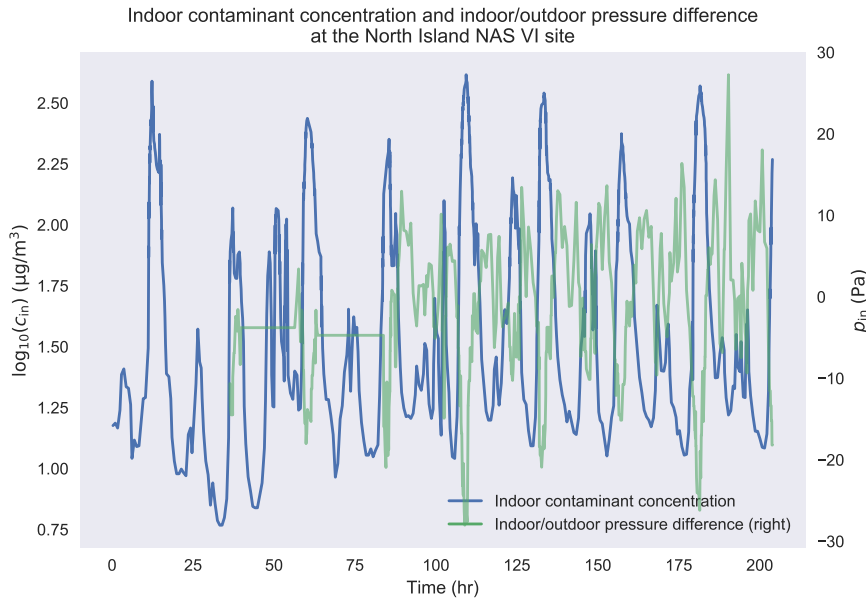
An example of such a site is a site at North Island Naval Air Station (NAS) in San Diego, California, characterized by sandy soil. There the indoor contaminant concentration and building pressurization were highly correlated[25]. Figure 4.2 demonstrate this correlation by showing the fluctuating indoor contaminant concentration and building pressurization at North Island NAS over time. Figure 4.2 also includes a kernel density estimation (KDE) plot of the building pressurization and indoor contaminant concentration. The KDE plot and calculated Pearson's r values show that indoor contaminant concentration and building pressurization was even more strongly associated at North Island NAS than the ASU house when the preferential pathway was open. This strong correlation can partly be attributed to the sandy soil at the site, but also to the significant building pressurization fluctuations at the site (compared to the ASU house).

In contrast, Hers et al.[77] studied a VI site in North Battleford, Saskatchewan, Canada, where they continuously monitored oxygen, pressure differentials, soil temperature, soil moisture, and weather conditions. The recorded data was used together with a reactive transport model (MIN3P-DUSTY) to simulate biodegradation and transport at the site. Together with analysis of the site data, they concluded that contaminant transport was dominated by diffusion, and little association between building pressurization and contaminant entry existed.

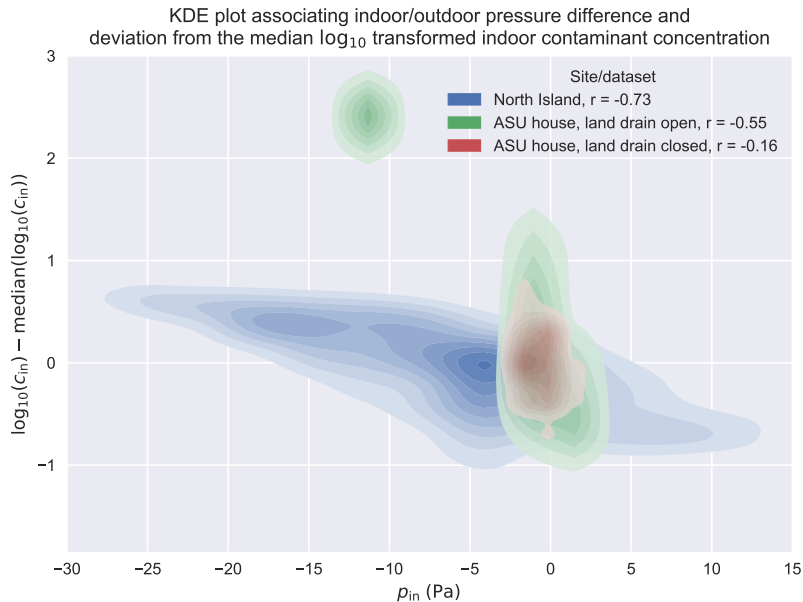
This indicates that for many sites characterized by other soil types, significant advective transport of contaminant vapors into the building is likely to be possible in the presence of some preferential air source. It is important to note however, that preferential pathways can be of many types, not just the one case that we have considered in Chapter 3. For example, having a layer of loose, unconsolidated soil adjacent foundation walls might in some cases

provide a low resistance pathway to flow of air to the subslab region.

The consequences of this analysis are important when considering the application or interpretation of certain types of vapor intrusion investigation strategies.



(a) Time series of the indoor contaminant concentration and indoor/outdoor pressure difference at the North Island NAS VI site. A negative pressurization value here indicate that there is a net flow of air into the building.



(b) Kernel density estimation (KDE) plot of indoor contaminant concentration  $c_{in}$  and indoor/outdoor pressure difference  $p_{in}$  at North Island NAS and the ASU house (considering the periods when the land drain was open and closed respectively). Indoor contaminant concentrations are  $\log_{10}$  transformed and normalized to their respective median values to allow comparison of how building pressurization contributed to indoor contaminant concentration variability. A deeper color indicates that the two variables are more closely associated. Pearson's  $r$  values of  $\log_{10}(c_{in})$  and  $p_{in}$  for each dataset were also calculated.

Figure 4.2: Building pressurization and indoor contaminant concentration were highly correlated at the North Island Naval Air Station (NAS) VI site.

## 4.3 Applying Transport Classification Concept

Contaminant entry from the subsurface into the a building may be dominated by advection or diffusion and which it is dramatically changes how a structure is expected to respond to change in building pressurization. For diffusion dominated sites, contaminant entry rates will be relatively decoupled from building pressurization, except in the limit where the building is sufficiently pressurized relative to the subsurface that the diffusion pathway is effectively cut off. This has implications for a wide variety of VI investigation strategies, but is perhaps most relevant for attempting to use CPM and choosing the relevant ITS parameters for study.

### 4.3.1 The Controlled Pressure Method

The idea of CPM is to control internal building pressurization, e.g. by using some fans or blowers to induce a higher or lower than ambient pressure in the structure. The normal expectation is that this will in turn control the contaminant entry rate. The underlying assumption in application of this method is that contaminant entry into a building is largely advective in nature. Because the effect of minor pressure fluctuations on diffusion coefficients is negligible, the only effect that such a building pressure variation can have is in adjusting the advective flow that either promotes or impedes the diffusive flux. But as the preceding Péclet number analysis has already shown, most cases are quite far towards the limit of diffusion control, and so small changes in advective entry rates will have minor effects on diffusive entry rates. Thus at "diffusion-controlled sites" the CPM method will not be as effective.

Figure 4.3 further illustrates this point. Reconsidering the case of the ASU house analysis already discussed in Chapter 3, during the period when the land drain preferential pathway was open, CPM dramatically increased indoor contaminant concentrations compared to the when the CPM system was inactive. However, after the closing of the land drain preferential

pathway, CPM did not have any significant effect on measured indoor contaminant concentrations. From the modeling of this situation, it was deduced that the presence of the land drain preferential pathway made advection the dominant entry mechanism of contaminant vapors into the building. Once that pathway was closed, the influence of a significant depressurization of the building was rather muted, because the basic diffusive entry pathway was largely unaffected.

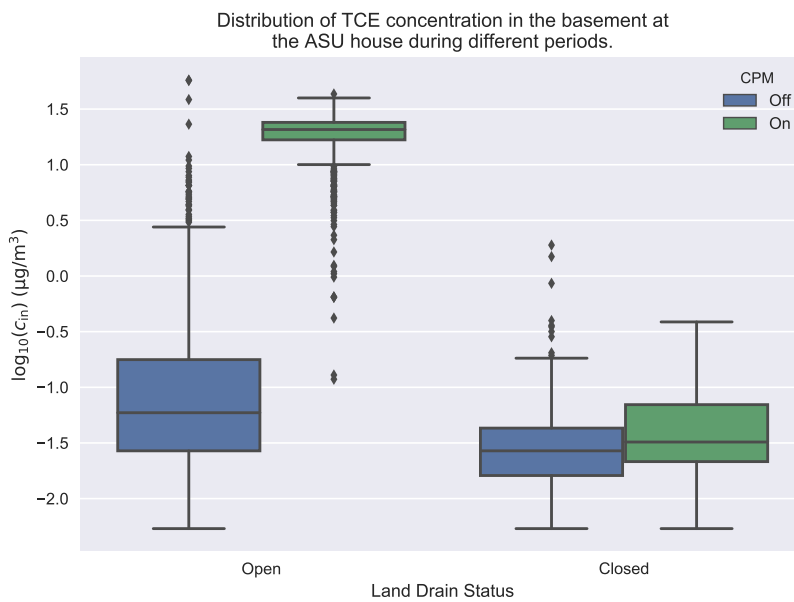


Figure 4.3: Boxplot showing the log-10 transformed TCE concentrations measured at the ASU house as a function of whether the preferential pathway was open or closed. The measured contaminant concentrations obtained during the reduced pressure CPM and "natural" vapor intrusion periods are considered separately. The box signifies the interquartile range (IQR) of values, with the central line representing the median value, and the top and bottom of the box are the 25th and 75th percentiles. The whiskers extend to 1.5 times the IQR. Markers indicate outlier data points that fall outside the whiskers.

The above results warn that depressurization of a structure using CPM might not lead to the expected result of a significant increase in entry rate of contaminant. Proponents of the technique argue that the method can offer a "worst possible case" result for a particular building, because the employed depressurization will be greater than anything that would naturally be encountered in the structure. This thinking is clearly influenced by a conceptual model that views advective entry as a dominant entry mode. The logic that such depre-

surization will offer a "worst possible case" result is actually not flawed, because enhancing contaminant entry rate is a real consequence of the depressurization. What will not be as apparent in the results from a diffusive entry limited case is that there is any relationship between the degree of depressurization and entry rate (and thus, indoor air concentration); there is a good chance that any small increase in concentration would be lost in the normal "noise" of such concentration measurements. The true value of the CPM can come in cases in which there is an obvious and large increase in entry rate with the degree of depressurization; in those cases, there will be a clear indication of either a permeable soil or the existence of a preferential pathway that can support advective entry as the dominant mode of contaminant entry.

There is an additional consideration that should not be overlooked when conducting a CPM investigation of VI. CPM not only affects the contaminant vapor entry rate into a building, but can also have an impact on air exchange rates within the building being tested. Figure 4.4 shows the effect that CPM had on air exchange rates at the ASU house, where they increased significantly during the testing period. The effect of this is that contaminant expulsion from the house is increased during the testing period, which decreases the indoor contaminant concentration for a given contaminant entry rate. This is a concern voiced in [29][29] an evaluation of the CPM results at the ASU house, and suggested that a tracer-gas test to measure air exchange rate should be conducted during CPM. This is used to introduce a correction term to account for the elevation of air exchange rate above its "natural" values. Since CPM is used to determine the worst-case scenario, this correction term should be used to calculate the indoor contaminant concentration with worst-case entry rates, but "natural" air exchange rate values, i.e.  $\approx 0.5 \text{ h}^{-1}$  instead of the elevated values. In this case, it is apparent that the measured values of indoor air concentration might have been a factor of 5 or 6 lower than would otherwise have been obtained for the given change in entry rate. This means that the results in Figure 4.3 might have understated the effect of the entry rate change.

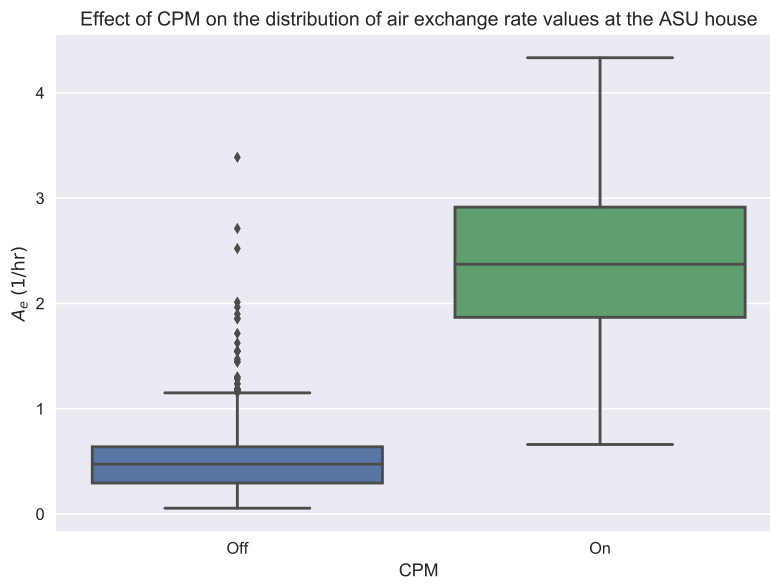


Figure 4.4: Boxplot showing the distribution of air exchange rate values at the ASU house, considering the effect of CPM.

This highlights an issue with CPM at VI sites characterized by diffusive transport. If the increased depressurization doesn't yield higher contaminant entry rates into the building, but elevates air exchange rate, then indoor contaminant concentration may be artificially lowered, and actually underestimate the VI risk. This further shows the advisability of using tracer-gas monitoring to measure air exchange rates when using CPM.

### 4.3.2 Indicators, Tracers, And Surrogates

As has been discussed throughout this work, VI can be characterized by great temporal variability in indoor air contaminant concentrations. These variations can occur on a variety of time-scales, from days to longer seasonal trends, which can require collection of significant amounts of data to fully characterize. To reduce the resources expended on these efforts, and increase the likelihood of determining the relevant VI risk, it is desirable to employ indicators, tracers, and surrogates (ITS) that can be used to readily predict the periods and conditions when the highest indoor contaminant concentration at a site are likely to manifest.

Which specific ITS are most appropriate for this task, and under which circumstances they are reliably employed has, has yet to be determined.

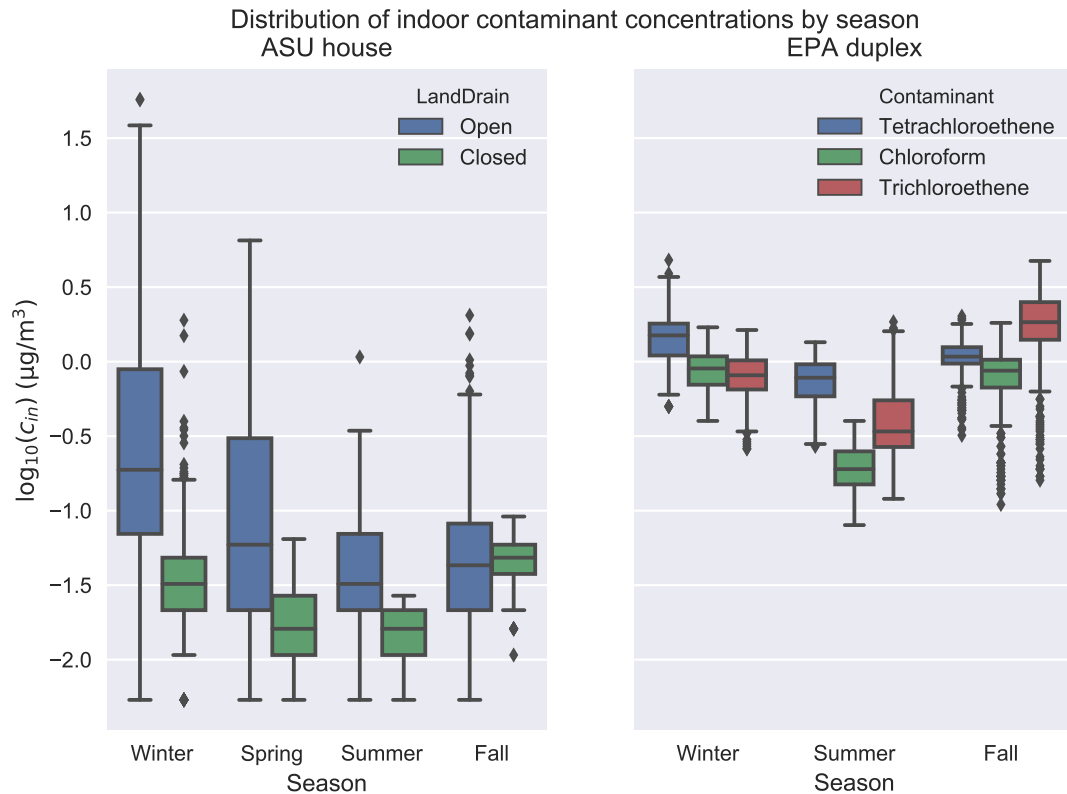


Figure 4.5: Seasonal distribution of indoor contaminant concentration at the ASU house and EPA duplex. At the ASU house, the effect of the land drain preferential pathway is considered. At the EPA duplex, the differences in distribution for three different contaminants are considered. Here "winter" includes December to February, with each subsequent season being defined by the subsequent three months.

Seasonal trends have been observed to be common at many VI sites, with winter often cited as the period most likely to lead to measurements of elevated indoor contaminant concentrations[78, 77, 79, 8, 26]. This is a trend that partly occurred at the ASU house as well (see Figure 4.5); indoor contaminant concentrations were indeed highest during winter when the land drain preferential pathway was open. However, this seasonal trend was non-existent after the closing of the land drain. At the EPA duplex, indoor contaminant concentrations were slightly higher during winter and fall than summer, but only marginally so.

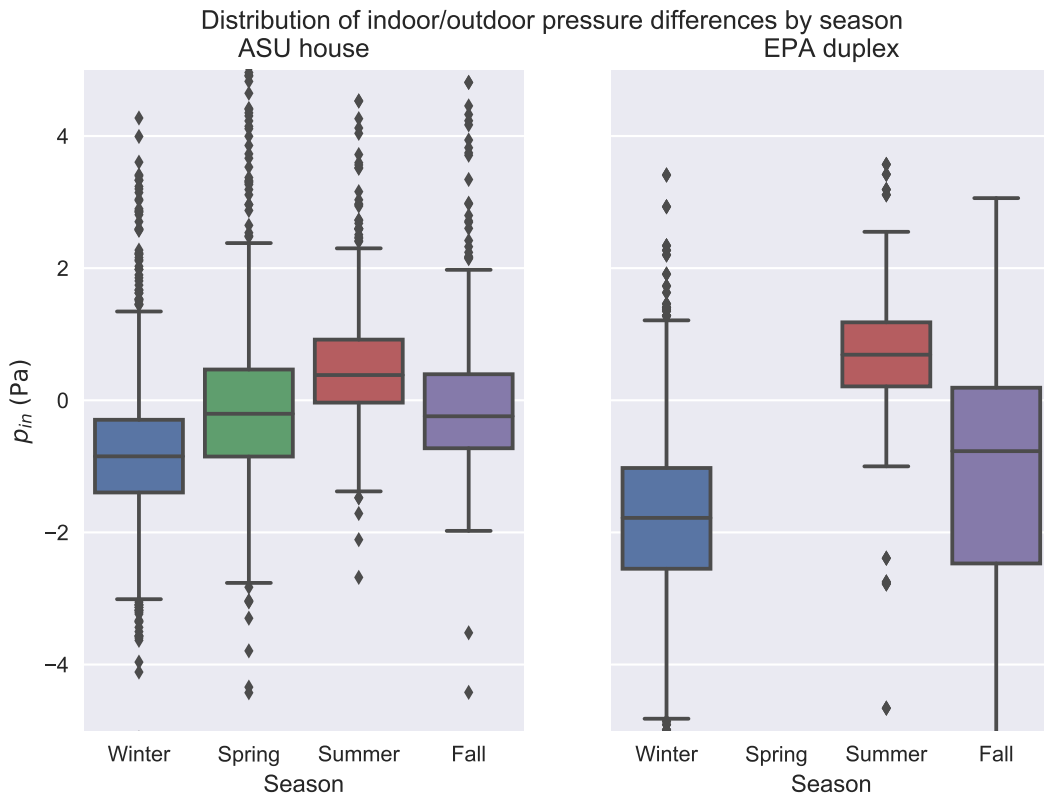


Figure 4.6: Seasonal distribution of indoor contaminant concentration at the ASU house. A negative value indicates that the building is depressurized relative to ambient.

The observed seasonal trend at the ASU house when the preferential pathway was open, can be understood by examining the seasonal distribution of indoor/outdoor pressure difference, displayed in Figure 4.6. Here we see that building depressurization was greatest during winter, and that the house was slightly less depressurized during the shoulder seasons, and it was usually overpressurized during summer. Considering this together the fact that with advective entry dominated during the period when the preferential pathway was open, explains why indoor contaminant concentrations are higher during the colder seasons. The significant degree of depressurization in winter contributed significantly to what was an advectively determined entry rate during that period of time. The opposite would have been true during summer, when it is likely that the use of air conditioning slightly overpressurized the building. Conversely, when the preferential pathway was closed off, the entry of

contaminant shifted to being diffusion rate controlled, and the variations in internal building pressure had little effect on the entry rate.

The EPA duplex exhibited a trend in building pressurization by season that is similar to that observed at the ASU house, i.e. it is more depressurized during colder seasons. This can help explain why indoor contaminant concentrations were likewise slightly higher during colder seasons. While the nature of the contaminant entry into the EPA duplex is not as well understood as that at the ASU house, it was shown in Chapter 3 that the association between building pressurization and indoor contaminant concentrations were somewhere between that of the ASU house before and after the closing of the preferential pathway (compare Figures 3.4 and 3.7). The situation regarding likely entry pathways at the EPA duplex is far more complicated and less well understood than that at the ASU house.

All that can be said at the moment is that while advective contaminant entry may not be dominant at the EPA duplex, it certainly isn't insignificant.

These data and analysis demonstrate that for advection entry controlled sites, building pressurization can probably be used as an effective ITS, whereas at a diffusion entry site, it may not be reliable. The advection entry controlled sites are those built on very permeable soils, or which are influenced by some preferential pathway, which allows advective entry to be the dominant entry pathway. This by itself may be challenging to determine in advance. Even if this could be established, to use building pressurization effectively as an ITS, building pressurization values would need to be known, and instrumenting a house to obtain such values is not generally feasible in VI screening studies. Instead, it would be useful to be able to predict the likely levels of indoor-outdoor pressure difference based on some easier to measure parameters - such as weather conditions.

## 4.4 Predicting the Extent of Building Pressurization

Building pressurization may be usable as an effective ITS under the right circumstances. However, determining this requires a measurement device to be installed, and moreover this device needs to record values over some length of time to establish trends. Thus, it would be desirable to use some more readily available metric, such as weather data, to predict the degree of building depressurization (since depressurization is of most concern in an advective entry scenario).

A variety of factors can contribute to determining overall building pressurization. Some of these are building occupant controlled and induced, such as forced convection associated with heating, ventilation, and air conditioning (HVAC) systems. Patterns associated with these can be difficult to use to for predictive purposes, unless the nature of building operation is regular and predictable. Such HVAC associated effects can at some sites be the dominant factors controlling building pressurization.

Weather primarily contributes to building pressurization through two effects. The temperature difference between the interior of the building produces a density and resultant pressure gradient on either side of a building wall - this is part of what is commonly called the *stack effect* (another part being associated with the withdrawal of combustion air in internally-located heating equipment). Wind striking a building can also produce a pressure effect within the building, the magnitude of which is dependent on wind speed. However, whether some portion of a building is pressurized or depressurized by wind, is complicated and generally depends on the wind direction and building characteristics; wind blowing on a leaky window causes a very different effect compared to wind striking a featureless wall. Equations for predicting building pressurization as a function of weather are available in The American Society of Heating, Refrigerating and Air-Conditioning Engineers (ASHRAE) 2017 Handbook[80] which is used as the primary source in this section.

Weather phenomena can likewise affect air exchange rates, and this has been a significant focus in the VI modeling work by Shirazi and Pennell[38]. As their work shows, predicting

air exchange rates can be challenging, as accurate characterization generally require detailed knowledge of the interior of a building. This will not be a focus in this work.

The study of the EPA duplex involved continuous monitoring of the indoor and outdoor temperature the wind speed as well as its direction using an on-site weather station mounted on the roof of the building. These data when combined with the recorded indoor/outdoor pressure differences offers an opportunity to establish how well building pressurization can be predicted using weather.

#### 4.4.1 Wind Effects

To truly capture the impact that wind can have on a building and its pressurization, it is usually necessary to conduct wind tunnel tests of scale models of the building, or detailed computational fluid dynamics (CFD) simulations. This is especially true for buildings of even modestly complex geometric shapes, where it is impossible to predict the wind pressure field without these tools. However, it is possible to derive some simple equations to account for wind effects on simple rectangular block-type buildings.

Even with assumptions, the inherent turbulent nature of wind means that it is truly never at steady-state. Thus wind striking a wall generates a distribution of pressures across the surface, that can vary widely in a short period of time; resolving this with a high degree of accuracy requires significant computational effort. However, by considering a time-averaged wind induced pressure field over some period, it is possible to develop simple equations for predicting wind induced pressurization on a rectangular building. The drawback of this approach is that large pressure fluctuations may not be captured.

As the wind strikes the wall of a house, the air velocity in the direction of the wall falls to zero, and the change in momentum in this direction normal to the wall is directly proportional to the pressure on the wall:

$$\Delta p_w = \frac{1}{2} \rho u_{\text{wind}}^2 \quad (4.2)$$

where  $\Delta p_w = p_{\text{wall}} - p_{\text{wind}}$  [Pa] is the pressure at the building wall relative to the wind free-stream pressure;  $\rho_{\text{air}}$  [ $\text{kg m}^{-3}$ ] is the air density; and  $u_{\text{wind}}$  [ $\text{m s}^{-1}$ ] is the free-stream wind speed, here assumed to be the wind speed measured at some place where it is unaffected by terrain or buildings.

However, (4.2) neglects wind striking the wall at an angle or various obstacles. These can be accounted for by introducing a drag or pressure coefficient  $C_p$  into (4.2) giving (4.3).

$$\Delta p_w = C_p \frac{1}{2} \rho u_{\text{wind}}^2 \quad (4.3)$$

$C_p$  is a dimensionless number, varying between -1 and 1, and is a function of wind direction, the building itself, and immediate surrounding area.

Air density  $\rho$  changes with temperature and barometric pressure, which can be accounted for via the ideal gas law.

$$\rho = \frac{p_{\text{bar}}}{R_{\text{spec}} T} \quad (4.4)$$

here  $p_{\text{bar}}$  [Pa] is the barometric pressure;  $R_{\text{spec}} = 287.058 \text{ J kg}^{-1} \text{ K}^{-1}$  is the specific gas constant for dry air; and  $T$  [K] is the ambient outside temperature.

To use (4.3) for predicting pressurization at the EPA duplex, we need to choose some  $C_p$  value; ideally, a CFD simulation of the structure would be used to determine  $C_p$  as a function of the wind direction between 0 and 360 degrees. There are some  $C_p$  values available for some generic structures in the American Society of Civil Engineers book for building codes and standards[81]. However, none of these seem applicable to a duplex, nor seem to deal with the building located on the eastern side of the EPA duplex. Instead we assume a generic  $C_p = 0.35$ , as values in this range are common.

Another factor to consider is that a building will be pressurized or depressurized by wind depending how leaky the wall it strikes is. Generally, walls featuring doors, windows, or other opening will cause a depressurization, while a simple flat wall will cause a overpressurization

effect<sup>1</sup>. By inspection of the EPA duplex, we see that all walls feature windows, but since we're only concerned with the pressurization of the heated side of the duplex (422, the right-hand side half in Figure (3.5a)), we will assume that westerly wind overpressurizes the 422 side.

Wind direction was recorded in degrees relative to northerly wind at the EPA duplex, however, for simplicity we will divide these degrees up into eight cardinal directions (north, north-east, etc) and assign signs to indicate pressurization or depressurization respectively to each direction (see Soil type 4.1).

Cardinal direction	Wind direction [°]	Pressurization sign
N	$0 \pm 22.5$	1
NE	$45 \pm 22.5$	1
E	$90 \pm 22.5$	1
SE	$135 \pm 22.5$	1
S	$180 \pm 22.5$	1
SW	$225 \pm 22.5$	1
W	$270 \pm 22.5$	-1
NW	$315 \pm 22.5$	1

Table 4.1: Division of wind direction into discrete cardinal directions with associated pressurization or depressurization of the heated "right hand side" of the EPA duplex. Here all walls feature windows or doors, except for the western side, which features the other half of the duplex, and hence wind striking from this direction will likely depressurize the heated side.

#### 4.4.2 Temperature Effects

The pressure of any fluid under the influence of gravity varies with elevation and the density of the fluid determines the magnitude of the pressure exerted by a column of fluid. If two columns of air at different temperatures are separated by a wall at , a pressure difference will exist across the wall. Again, this is part of the origin of the *stack effect* in a building.

The pressure of air  $p$  as a function of height above some reference plane at height  $z_0$  is

---

<sup>1</sup>It should be noted that this relationship is not always true, and will depend on the indoor/outdoor temperature difference, as well as the magnitude of the wind speed, as shown by Shirazi and Pennell[38].

given by

$$p = p_0 - \rho g z \quad (4.5)$$

here  $p_0$  [Pa] is air pressure at reference plane  $z_0$  [m];  $\rho$  [ $\text{kg m}^{-3}$ ] is the density of air;  $g = 9.82 \text{ m s}^{-2}$  is the acceleration due to gravity; and  $z$  [m] is the elevation above  $z_0$ .

Since we are concerned with predicting the pressure effect for a relatively short building, we can neglect vertical air density gradients giving the horizontal pressure difference as:

$$\Delta p_s = (\rho_{out} - \rho_{in})g(z - z_0) = \rho_{out} \frac{T_{in} - T_{out}}{T_{in}} g(z - z_0) \quad (4.6)$$

$\Delta p_s$  [Pa] is the portion of the stack effect induced by a horizontal pressure difference;  $T$  [K] is the absolute temperature; and the subscripts *in* and *out* are in reference to the indoor and outdoor values respectively. Like in the wind effect section, air density is calculated as function of the barometric pressure and outside temperature.

As a reference height difference  $\Delta z = z - z_0$ , we use  $\Delta z \approx -3 \text{ m}$ . This based on the estimated height difference between the EPA duplex basement and some midpoint of the exterior of the building. The recorded indoor/outdoor pressure difference at the EPA duplex is here defined as the pressure difference between wall-port 1 (WP-1), which was on the outside of the house, and the duplex basement.

#### 4.4.3 Air Exchange Rate

It is possible to predict air exchange rate of a building using a similar approach to the one needed for pressure. However, this approach requires detailed knowledge of the leakiness of a building and how different house compartments communicate, and thus is beyond the scope of this work. Even if possible, air exchange rates were not continuously monitored at the EPA duplex, so evaluation of this approaches efficacy using the recorded weather data is difficult. Predicting air exchange rate of a building by modelling was done in the VI modeling of Shirazi and Pennell[38], where they were able to determine building pressurization and

air exchange rates of a building with high accuracy.

#### 4.4.4 Predicting Pressurization At The EPA Duplex

The indoor/outdoor pressure difference  $p_{in}$  is assumed to be the sum of the stack effect ( $\Delta p_s$ ) and wind contribution ( $\Delta p_w$ ), here given simply by  $p_s$  and  $p_w$  respectively.

$$p_{in} = p_s + p_w \quad (4.7)$$

Figure 4.7 shows the recorded indoor/outdoor temperature difference and wind speed, how these two contribute individually to  $p_{in}$ , and how they contribute together to  $p_{in}$  across the EPA duplex study period.

Figure 4.7 shows that with this relatively simple approach, the general trend of  $p_{in}$  is captured. Major errors seem to be mostly due to either a failure to capture large changes in  $p_{in}$ , or overpredict changes in  $p_{in}$ . Both of these seem to stem from a relatively poor characterization of the wind influence, which seems strongly correlated with large changes in  $p_{in}$  in general.

The differences and individual contributions of the temperature and wind effects can be further examined in Figure 4.8 and Table 4.2. These show that this approach reasonably predicts most of the  $p_{in}$  distribution, specifically the mean pressurization and standard deviation are captured, but fails to capture the important outliers where the building is significantly depressurized. This is perhaps due to poor accounting for the wind effect, and with more advanced modeling of the influence of wind, such in the work by Shirazi and Pennell[38], this is likely to be better captured.

Regardless, this approach shows that using temperature, wind, barometric pressure, and some simple assumptions about a building, it is possible to reasonably accurately characterize how building pressurization may change in the long-term and short-term. This is particularly useful for planning when to conduct testing at sites that can be identified as more advection

	Data	Predictions	
		$p_s$	$p_s + p_w$
Mean	-1.33	-1.50	-1.31
Std.	2.15	1.12	1.96

Table 4.2: Mean and standard deviation of recorded and predicted building pressurization. Here considering the temperature induced stack effect pressure difference  $p_s$  alone, and the combined contribution of wind induced pressure difference  $p_w$  and  $p_s$ .

entry dominated; at such a site samples should logically be collected when the building is most continuously depressurized, i.e. when  $\Delta T > 5^\circ\text{C}$  and when there is little wind so as to reduce uncertainty from its influence. As Figure 4.8 emphasizes, the main contribution to the depressurization is the stack effect, which is most severe in winter. Thus, these results point in the direction of supporting the rule of thumb that sampling should be done in the cold months, in order to get the most conservative values. As noted before, this really applies mostly to sites at which advective contaminant entry dominates.

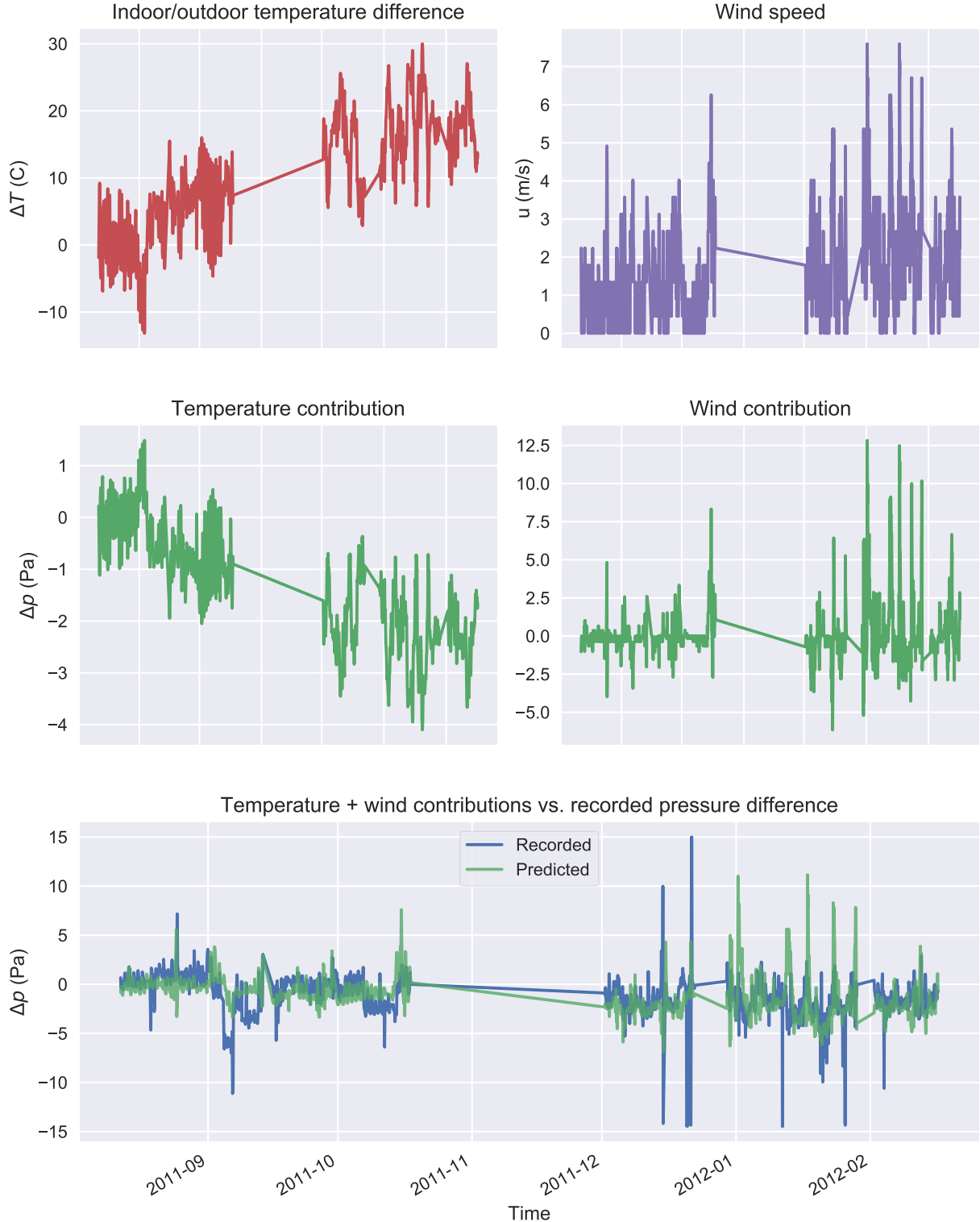


Figure 4.7: How indoor/outdoor temperature difference  $\Delta T$  and wind contributes to building pressurization at the EPA duplex. The top left panel shows  $\Delta T = T_{in} - T_{out}$ , i.e. a positive value indicates that it is warmer indoors than outdoors. The top right shows the wind speed  $u_{wind}$ . The middle panels shows the contributions of  $\Delta T$  and  $u_{wind}$  to  $p_{in}$  respectively. The bottom panel shows the combined contribution of  $\Delta T$  and  $u_{wind}$  to  $p_{in}$ , and compared to the recorded  $p_{in}$  values.  $p_{in} < 0$  indicates that the building is depressurized.

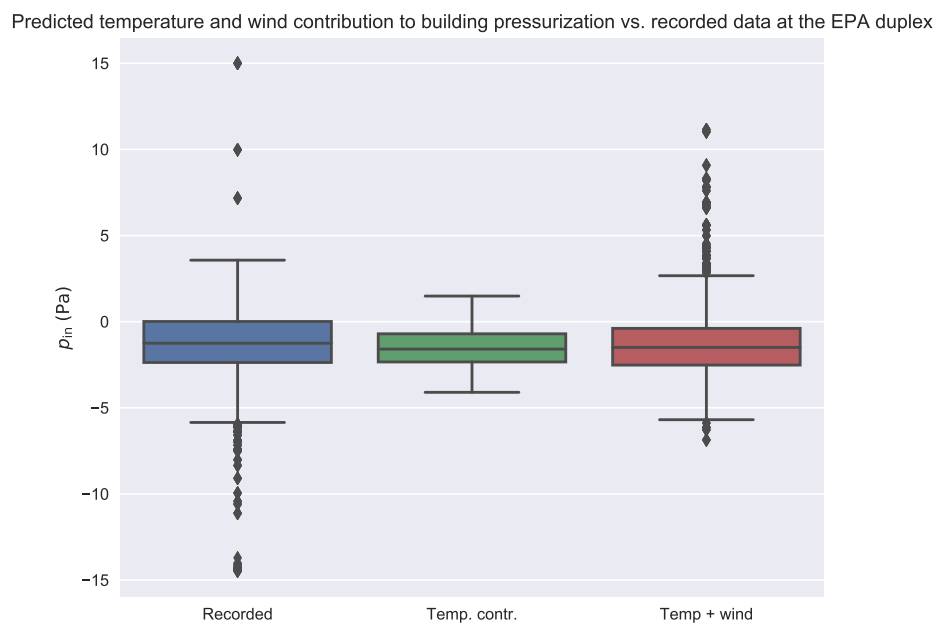


Figure 4.8: Boxplot comparing the predicted  $p_{in}$  to the recorded values, and how the temperature and wind components contributes to the distribution of values.



# Chapter 5

## Sorption Phenomena in Transient Vapor Intrusion Scenarios

### 5.1 Summary

Many vapor intrusion (VI) contaminants have the capacity to sorb onto a variety of materials commonly found in buildings as well as soils, yet the role and effect of sorption in VI is largely unstudied. To bridge this gap we measure the sorptive capacities of trichloroethylene (TCE) on some materials at VI relevant concentrations; finding that material sorptive capacities vary orders of magnitudes, with cinderblock having a capacity to hold up to almost 41,000 times more contaminant than a comparable TCE contaminated air volume. Using these experimentally derived data together with a three-dimensional numerical model of VI, we then explore the retarding effect that sorption has on contaminant transport in soils and indoor environments. We also applied the model to investigate how the contaminant desorption from these materials, following the implementation of a successful VI mitigation scheme, affect contaminant expulsion. We find that desorption may cause significant delay: in some cases taking months longer than if there were no sorbed contaminants.

## 5.2 Introduction

Most vapor intrusion (VI) contaminants have the capacity to sorb onto soil and various common indoor materials, but the role and more importantly, the consequences of these sorption processes in VI are poorly understood[14, 15, 82]. The migration of contaminant vapors from their source into the VI impacted building and potential indoor sources is usually the prime concern in VI investigations. Rarely are the sorbed contaminant vapors in the soil or indoor considered in an investigation. These may potentially act as a capacitance, storing and releasing contaminant vapors in response to a change in contaminant concentration. Consequently, contaminant vapors may be more persistent than expected at a site that has undergone remediation, potentially reducing the effectiveness of mitigation in the short term, or leading to misleading results regarding mitigation efficacy.

It is well recognized that building materials have the capacity to sorb pollutants. The sorptive capacity of various volatile organic compounds (VOCs) of concern in VI has been examined on a variety of building materials, such as particle density board[83], gypsum wallboard[84], and plywood and carpets[85]. However, most of these studies used relative high contaminant concentrations, usually around mg/m<sup>3</sup>[83] or even higher. This is several orders of magnitude higher than the concentrations relevant in VI and due to the non-linear nature of sorption with respect to concentration, sorption studies at lower concentration are needed.

Many VOC sorption studies have also focused on the interaction between building materials and formaldehyde[84], toluene, and decane[85]. However, one of the contaminants of greatest concern in VI - trichloroethylene (TCE), has not received attention. This is despite the fact that sorption of TCE (and other comparable VOCs) on activated carbon is extensively used to treat indoor air contamination and their sorption on passive tube samplers is widely employed for analysis of these compounds[7].

Over the years many VI sites have been investigated. Two well-known examples of these are the studies of a house in Layton, Utah and one in Indianapolis, Indiana. Both of

these sites were outfitted with a wide variety of instrumentation to measure various metrics such as contaminant concentration in interior, soil, and groundwater, as well as pressure, temperature, or weather. These studies yielded some of the richest VI datasets available and gave invaluable insights into the VI process, including into the application of CPM[29] and sub-slab depressurization (SSD) mitigation systems[86, 65]. However, neither of these studies considered the role that sorption may have had at these sites.

The potential impact of sorption could perhaps be most significant in situations in which contaminant entry rates vary widely with time, such as in the application of the controlled pressure method (CPM) and various mitigation schemes. The controlled pressure method involves the forced over- and depressurization of a building to maximize or minimize the contaminant entry rate into the building. This can help the investigator ascertain the worst-case VI scenario and help identify potential indoor contaminant sources[28, 29]. However, if the building indoor materials have a large sorptive capacities, then desorption and sorption processes may significantly affect the indoor air contaminant concentration. Likewise, a significant amount of sorbed contaminant may be released from interior materials over an unknown period of time after mitigating the contaminant intrusion at a site[14, 15].

In the past, VI models have been used to gain further insight into VI processes[33, 87, 38]. Previous examples of VI modeling studies include one on the role of rainfall in VI[88], or drivers of temporal variability in some of the aforementioned sites[89]. However, while many VI models are presented including a sorption term in the governing equation for contaminant transport in soils, none have really explored the role of sorption in VI in a transient simulation. The reason for this is two-fold. First, there has been a general lack of interest in sorption related to VI thus far. Secondly, the vast majority of VI modeling efforts and studies have focused on steady-state analyses of VI, and sorption only affects soil contaminant transport in time-dependent scenarios.

To bridge this knowledge gap we will explore the role of sorption in VI by considering the significance of newly obtained contaminant sorption data in the context of VI models.

Sorption data of TCE on various materials, including cinderblock, drywall, wood, paper, carpet, and Appling soil have been measured in a fixed bed sorption experiment. These sorption data are used to generate sorption parameters to be used in a three-dimensional finite element VI model. For this purpose we will consider a prototypical VI scenario where a free-standing house, with a basement, is overlying a homogenously contaminated ground-water source. Using this model we investigate how contaminant transport is affected by sorption, how indoor sorptive materials affect indoor air concentration as the building's pressurization fluctuates and how indoor air concentration are affected by indoor materials following successful mitigation of the structure.

## 5.3 Methods

### 5.3.1 Experimental Setup

The details of the experiments used in obtaining the sorption input data will be discussed in a separate paper being prepared on this topic. Here, we only briefly summarize the experiments. To study the dynamic sorption of TCE onto the selected building materials, the two-step process shown in Figure 5.1 was used.

A 7.5 cm by 1.27 cm stainless steel column was filled with a ground sample of the material to be tested. We use 2 g of drywall, and 1 g of all the other materials to pack the tube. Samples were held in by glass wool plugs. Using flow controllers, TCE was diluted in nitrogen gas to 1.12 ppb<sub>v</sub> and flowed through the column at a rate of 60 ml min<sup>-1</sup>, for a pre-selected time period. After the material had been exposed for the selected time, the column was detached and attached to the desorption system.

In the desorption system, the sample-containing column was heated to 100 °C and pure nitrogen gas was flowed through the previously outlet side of the column - carrying the desorbed contaminant with it. The gas was then passed through a long tube, allowing the gas to cool to room temperature, from which it flowed into a carbon-filled stainless steel

sorption column which trapped all of the TCE for analysis. The sorption column was then desorbed into a gas-chromatograph fitted with a electron capture detector.

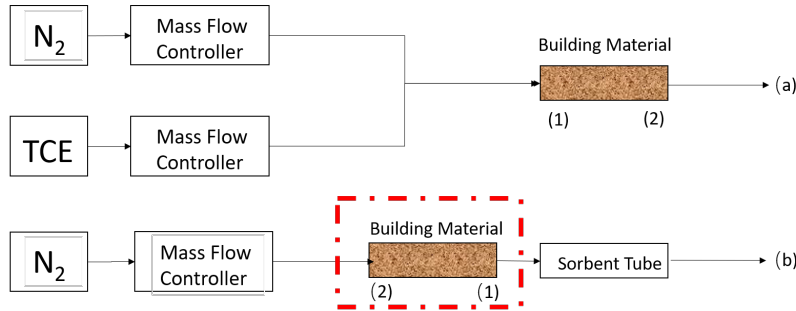


Figure 5.1: Schematic of experimental setup.

### 5.3.2 Numerical Model

To investigate the role of sorption in VI, we developed a three-dimensional numerical model of a building overlying a TCE contaminated groundwater source in the commercial finite-element solver COMSOL. The building is assumed to have a 10 m by 10 m footprint, with a 3 m ceiling height, and its foundation is located 1 m below ground surface (bgs). The contaminated groundwater is 4 m bgs, and is assumed to be homogenously contaminated with TCE. The building is surrounded by homogenous "sandy loam" soil, that extends 10 m from its walls. Along the perimeter of the foundation, there is a 1 cm wide crack through which contaminant vapors enter the building and expulsion of contaminant vapors from the indoor occurs through air exchange with the outside.

Contaminant vapors are transported from the contaminated groundwater through the soil matrix via advection and diffusion and is described in section 2.5.4. The presence of the groundwater variably saturates the soil matrix with water, which has a significant effects on the contaminant transport and is modeled using van Genuchten's retention model[47] and explained in greater detail in section 5.3.2. The water in the soil matrix is assumed to be stationary, thus advective transport only occurs through the vapor phase, while diffusion occurs through both the water and the vapor phases. The contaminant vapors are also

assumed to be able to sorb onto the soil particles, and is modeled using a linear sorption model, and the interaction between the water and vapor phases are determined by Henry's Law.

The building is assumed to be pressurized relative to the outside, which gives an air flow in and out of the building (depending on if it is depressurized or overpressurized). This air flow causes the advective contaminant transport through the soil and the foundation crack. Darcy's Law is used to model the flow of air and is described in detail in section 5.3.2. A key assumption here is that the contaminant is so diluted in the air, that it is assumed to not affect the transport properties of air.

In our implementation, only the soil surrounding the building is explicitly modeled (as a three-dimensional geometry), and the interior of the basement is implicitly modeled as a continuously stirred tank reactor as described in section 2.5.1. These two are coupled via the foundation crack, from which the contaminant entry into the basement is calculated, and contaminant expulsion is determined by the air exchange rate. In this work we consider the role of sorption on materials in the interior, which is done as a equilibrium reaction.

An overview of this modeling approach may be seen in Figure 5.2.

### Vadose Zone Moisture Content

Since the contaminant transport occurs through the three-phase vadose zone, it is important that we correctly account for soil moisture content and its effect on advective and diffusive transport. In this modeled scenario, we assume that the soil moisture is at steady-state, and thus the soil moisture content is given by the retention model developed by van Genuchten[47].

The van Genuchten retention model gives the soil water saturation as a function of elevation above groundwater. This in turn gives the water and gas filled porosities in the

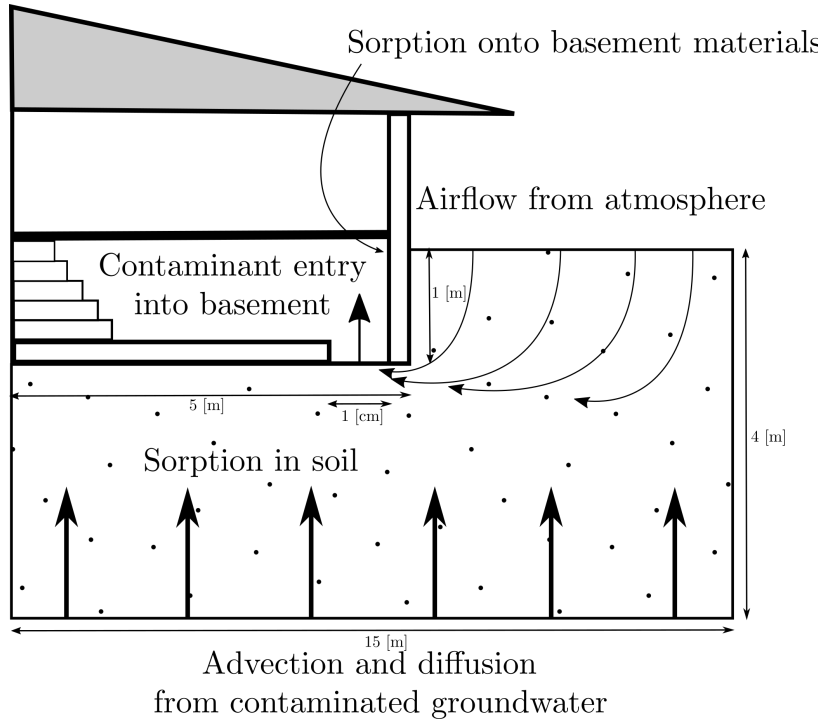


Figure 5.2: Schematic of the modeled vapor intrusion scenario.

soil, and the relative permeability of the soil matrix.

$$Se = \begin{cases} \frac{1}{(1+\alpha z^n)^m} & z < 0 \\ 1 & z \geq 0 \end{cases} \quad (5.1)$$

$$\theta_w = \begin{cases} \theta_r + Se(\theta_s - \theta_r) & z < 0 \\ \theta_s & z \geq 0 \end{cases} \quad (5.2)$$

$$k_r = \begin{cases} (1 - Se)^l (1 - Se^{\frac{1}{m}})^{2m} & z < 0 \\ 0 & z \geq 0 \end{cases} \quad (5.3)$$

$Se$  is the saturation, and ranges from 0 to 1, which represent completely unsaturated to fully saturated;  $z$  is a height relative to groundwater in meters, with  $z = 0$  the groundwater surface and  $z < 0$  into the vadose zone;  $\theta_r$ ,  $\theta_s$ ,  $\theta_w$ , and  $\theta_g$  are the dimensionless porosity parameters reflecting the residual moisture content, saturated porosity (or just porosity),

and water and air filled porosities respectively;  $k_r$  is the relative permeability for air. The soil is assumed to be sandy loam and van Genuchten properties can be seen in Table B.1 in the appendix.

## Gas Flow In The Vadose Zone

The gas flow in the vadose zone is governed by a modified version of Darcy's Law. Originally, Darcy's Law was developed to describe flow in saturated porous media; but flow in unsaturated media requires some modification[c.w.fetter contaminant 1993]. An effective permeability that depends on the relative permeability given by the van Genuchten equations is introduced to allow for correct permeability in unsaturated porous media.

The vapor flow continuity governing equation is given by

$$\frac{\partial}{\partial t}(\rho\theta_s) + \nabla \cdot \rho \left( -\frac{k_r\kappa}{\mu} \nabla p \right) = 0 \quad (5.4)$$

Here  $\rho$  is the density of air;  $\rho = 1.225 \text{ kg m}^{-3}$  is the density of air;  $\mu = 18.5 \times 10^{-6} \text{ Pa s}$  is the dynamic viscosity of air; and  $p$  is the fluid pressure. We assume that the contaminant vapors are so dilute that the gas flow properties can be taken to be those of air, specifically at 20 °C. All the transport properties may be found in Table B.1.

**Boundary Conditions** To solve (5.4) we assign the atmosphere boundary (see Figure 5.2) to be the reference pressure, i.e. zero pressure. The foundation crack boundary is assigned to be at the indoor-outdoor pressure difference value. Remaining boundaries are no-flow boundary conditions.

$$\text{Atmosphere} \quad p = 0 \text{ (Pa)} \quad (5.5)$$

$$\text{Foundation crack} \quad p = p_{\text{in}} - p_{\text{out}} = p_{\text{in}} \text{ (Pa)} \quad (5.6)$$

$$\text{All other} \quad -\vec{n} \cdot \rho \vec{u} = 0 \text{ (kg/(m}^2 \cdot \text{s})) \quad (5.7)$$

Here  $\vec{n}$  and  $\vec{u}$  are the boundary normal and gas velocity vectors.

**Initial Conditions** For steady-state problems, the initial conditions do not influence the solution. Transient simulations however, require initial conditions and these are assumed to be given by the steady-state solution.

### Mass Transport In The Vadose Zone

Contaminants in the vadose zone exist in three phases - gaseous, dissolved in water, and sorbed onto soil particles. While there are three distinct phase concentrations, the water and gas phases are related via Henry's Law (5.8).

$$c_g = K_H c_w \quad (5.8)$$

Where  $c_g$  and  $c_w$  are the gas and water phase concentrations respectively in mol/m<sup>3</sup>;  $K_H = 0.402$  is the dimensionless Henry's Law constant of TCE at 20 °C.

In this work, we consider sorption equilibrium between the soil and vapor phases, to be governed by the water contaminant concentration (5.9).

$$c_s = K_{\text{ads}} \rho_b c_g = K_{\text{ads}} \frac{\rho}{1 - \theta_s} K_H c_w \quad (5.9)$$

Here the  $c_s$  is the solid phase concentration in mol/kg;  $\rho_b$  is the bulk density of the soil kg/m<sup>3</sup>, which is given by the density  $\rho$  and the total soil porosity  $\theta_s$ ;  $K_{\text{ads}}$  is the vapor-solid sorption partition coefficient in m<sup>3</sup>/kg.

Mass transport in the vadose zone is governed by diffusion and advection and is given by (5.10). It is important to note that this governing equation is written in terms of the water phase contaminant concentration  $c_w$ , but via Henry's Law and the vapor-solid sorption partition coefficient, it does in fact describe the contaminant concentration and transport in

all three phases.

$$R \frac{\partial c_w}{\partial t} = \nabla \cdot [D_{\text{eff}} \nabla c_w] - K_H \vec{u} \cdot \nabla c_w \quad (5.10)$$

The first term in (5.10) gives the change in contaminant water concentration with respect to time, modified by the *retardation factor*,  $R$ , which is discussed below; The second is the effective diffusive flux which is modified by the effective diffusion coefficient  $D_{\text{eff}}$  which is also discussed below. The third is the advective flux where  $\vec{u}$  is the soil-gas velocity from Darcy's Law, which when multiplied with  $K_H$  gives the gas phase concentration advective flux, e.g. advective transport only occurs in the vapor phase and not the liquid phase (the water in the soil matrix is assumed to be at steady-state). The soil is assumed to be sandy loam and its properties can be seen in Table B.1.

**Contaminant entry into the building** The contaminant enters the building through a combination of advection and diffusive fluxes and is given by (5.11).

$$j_{ck} = \begin{cases} u_{ck} c_g - \frac{D_{\text{air}}}{L_{\text{slab}}} (c_{in} - c_g) & u_{ck} \geq 0 \\ u_{ck} c_{in} - \frac{D_{\text{air}}}{L_{\text{slab}}} (c_{in} - c_g) & u_{ck} < 0 \end{cases} \quad (5.11)$$

Here the  $j_{ck}$  is the molar contaminant flux into the building in  $\text{mol}/(\text{m}^2 \cdot \text{s})$ ;  $D_{\text{air}}$  is the contaminant diffusion coefficient in pure air in  $\text{m}^2/\text{s}$ ;  $L_{\text{slab}}$  is the thickness of the foundation slab in m. The flux expression changes if there is a bulk flow into the building, i.e.  $u_{ck} \geq 0$ , or out of the building.

**Retardation factor** As the contaminants are transported through the vadose zone, the partitioning between the various phases increases the contaminant residency time, retarding the transport of contaminants. This effect is represented by  $R$  which is the retardation factor (5.12).

$$R = \theta_w + \theta_g K_H + \rho_b K_H K_{\text{ads}} \quad (5.12)$$

Here  $\theta_w$ ,  $\theta_g$  are the water and gas filled soil porosities;  $K_{\text{ads}}$  is the vapor-solid partition coefficient in  $\text{m}^3/\text{kg}$ .

**Effective diffusivity** The effective diffusivity in the vadose zone varies with the soil moisture content, from being close to that in water when fully saturated and close to that in air when soil moisture is low. Millington-Quirk developed (5.13) which describes the effective diffusivity in variably saturated porous media.

$$D_{\text{eff}} = D_{\text{water}} \frac{\theta_w^{\frac{7}{3}}}{\theta_s^2} + \frac{D_{\text{air}} \theta_g^{\frac{7}{3}}}{K_H \theta_s^2} \quad (5.13)$$

Where the porosity terms reflect the water and gas phase tortuosity;  $D_{\text{air}} = 6.87 \times 10^{-6} \text{ m}^2 \text{ s}^{-1}$  and  $D_{\text{water}} = 1.02 \times 10^{-9} \text{ m}^2 \text{ s}^{-1}$  are the contaminant diffusion coefficient in air and water respectively in  $\text{m}^2/\text{s}$ ; The Henry's Law constant  $K_H$  appears here to reflect that all the contaminant transport is a function of the contaminant water concentration.

**Boundary Conditions** In this model, the sole contaminant source is assumed to be the homogenously contaminated groundwater, which we assume to have a fixed concentration. The atmosphere acts as a contaminant sink and thus this is simply a zero concentration boundary condition. Contaminants leave the soil domain and enter the building through a combination of advective and diffusive gas phase transport. The boundary condition applied to all other boundaries is a no-flow boundary.

$$\text{Atmosphere} \quad c_w = 0 \text{ (mol/m}^3\text{)} \quad (5.14)$$

$$\text{Groundwater} \quad c_w = c_{gw} \text{ (mol/m}^3\text{)} \quad (5.15)$$

$$\text{Foundation crack} \quad -\vec{n} \cdot \vec{N} = -j_{ck} \text{ (mol/(m}^2 \cdot \text{s})) \quad (5.16)$$

$$\text{All other} \quad -\vec{n} \cdot \vec{N} = 0 \text{ (mol/(m}^2 \cdot \text{s})) \quad (5.17)$$

$\vec{n} \cdot \vec{N}$  is the dot product between the boundary normal vector and the contaminant flux;  $j_{ck}$  is the contaminant vapor flux into the building. We assume that only contaminants in the gas phase enter the building, and dividing  $j_{ck}$  by  $K_H$  we get proper accounting in terms of the water phase concentration accounting in the main transport equation 5.10.

**Initial Conditions** For transient simulations in this work, the steady-state solution to a corresponding case is always used as an initial condition.

## Indoor Environment

The indoor air space is modeled as a continuously stirred tank reactor (CSTR) given by (5.29). Contaminants are assumed to only enter through the foundation crack, represented by  $n_{ck}$ , which is calculated by integrating the contaminant flux over the foundation crack boundary. The product of air exchange rate, (which governs how many house volumes are exchanged with the outside per time unit,) and indoor air contaminant concentration gives the contaminant exit rate from the house. The sorption of contaminant on indoor materials is given by the sorption term in (5.31) and the sorbed contaminant concentration on all interior surfaces is given by (5.30).

$$V_{\text{bldg}} \frac{\partial c_{\text{in}}}{\partial t} = n_{ck} - A_e c_{\text{in}} V_{\text{bldg}} - r_{\text{sorb}} V_{\text{mat}} \quad (5.18)$$

$$V_{\text{mat}} \frac{\partial c_{\text{sorb}}}{\partial t} = r_{\text{sorb}} V_{\text{mat}} \quad (5.19)$$

$$r_{\text{sorb}} = k_1 c_{\text{in}} - k_2 c_{\text{sorb}} \quad (5.20)$$

$$n_{ck} = \int_{A_{ck}} j_{ck} dA \quad (5.21)$$

Here  $V_{\text{bldg}} = 300 \text{ m}^3$  and  $V_{\text{mat}}$  are the indoor control volume and volume of indoor material in  $\text{m}^3$ ;  $A_e = 0.5 \text{ h}^{-1}$  is the air exchange rate;  $c_{\text{in}}$  and  $c_{\text{sorb}}$  are the indoor and sorbed (onto the indoor material) contaminant concentrations in  $\text{mol}/\text{m}^3$ ;  $n_{ck}$  is the contaminant entry rate in

mol/s, which is calculated by integrating the contaminant flux  $j_{ck}$  over the foundation crack area  $A_{ck}$  [ $\text{m}^2$ ];  $r_{\text{sorb}}$  sorption rate in  $\text{mol}/(\text{m}^3 \cdot \text{s})$ ;  $k_1$  and  $k_2$  are the sorption and desorption rate constants in  $1/\text{s}$ .

**Fitting Kinetic Parameters** These values of  $k_1$  and  $k_2$  are found by applying (5.31) numerically to the experimental data via least square fitting. We use Runge-Kutta method of order 5(4) as the numerical solve, which is implemented together with the least square method in the SciPy python package[90].

## 5.4 Results & Discussion

### 5.4.1 Fitting Sorption Parameters

Figure 5.3 shows the result of fitting the sorption data for three select materials - wood, Appling soil, and cinderblock concrete. The  $k_1$  and  $k_2$  represent the rates at which TCE sorbs and desorbs respectively onto/from the material of interest. The equilibrium partition constant, using the formulation in (5.31), is given by

$$K = \frac{k_1}{k_2} \quad (5.22)$$

and defines the sorption isotherm. Here a larger  $K$  indicates that there is a greater propensity for contaminant sorption.

To apply a soil sorption isotherm in (5.10)  $K$  needs to be converted to  $\text{m}^3/\text{kg}$ . This is done by multiplying  $K$  isotherm with inverse of the soil bulk density  $\rho_b$ , which is taken to be  $1460 \text{ kg/m}^3$ [91].

$$K_{\text{ads}} = \frac{K}{\rho_b} = 5.28 \text{ (m}^3/\text{kg}) \quad (5.23)$$

Table 5.1 shows the fitted parameters for the tested materials. Based on this these results we can see that cinderblock and soil have orders of magnitude larger sorption capacities than

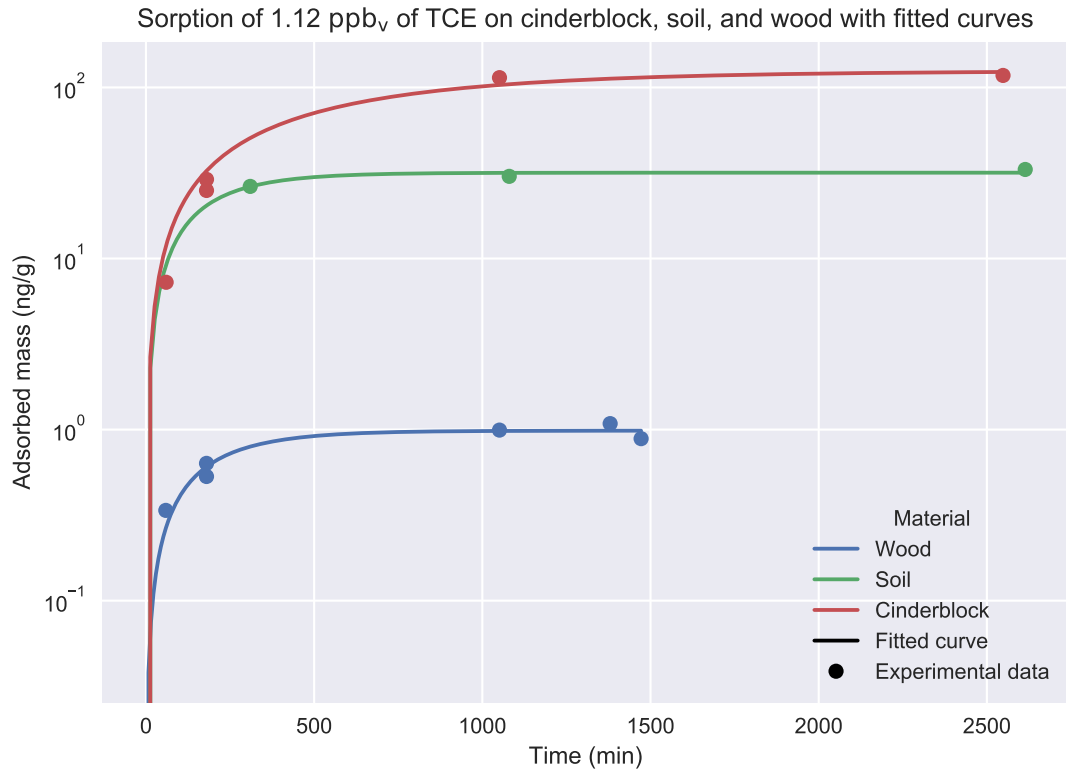


Figure 5.3: Experimental data of sorption of TCE onto three select materials as well as fitted sorption rates based on the kinetic model (5.31).

wood or drywall does. We can also see by that soil and cinderblock sorb quickly, much faster than a material with similar sorptive capacity such as paper.

Material	$k_1$ (1/hr)	$k_2$ (1/hr)	$K$
Wood	44.90	0.32	140.90
Drywall	87.94	0.41	214.87
Carpet	58.74	0.26	226.21
Paper	88.37	0.04	2195.69
Soil	2636.57	0.34	7702.94
Cinderblock	4175.16	0.10	41501.26

Table 5.1: Fitted kinetic sorption parameters based on sorption experiment data. Six different types of materials are considered.  $k_1$  and  $k_2$  are the sorption and desorption constants respectively, and  $K$  is the sorption equilibrium constant.

### 5.4.2 Soil Sorption's Retarding Effect

The effect of building pressurization is a key factor in VI that influences the advective contaminant transport into or out of the building. The magnitude of indoor contaminant concentration change in response to a pressurization change is significantly influenced by a variety of factors, such as soil permeability, foundation depth, soil moisture, and sorption. To investigate the effect that soil sorption has on contaminant soil mass transport in the VI context, we have run two types transient simulation where initially the modeled structure is depressurized at a steady -5 Pa to establish a steady-state baseline. At the start of the simulation, the building building is further depressurized to -15 Pa (5.24), or overpressurized to 15 Pa (5.25), and the simulation is allowed to run for 72 hours.

$$\text{Depressurization : } p_{\text{in}} = \begin{cases} -5, & t = 0 \text{ (hr)} \\ -15, & 0 < t \leq 72 \text{ (hr)} \end{cases} \quad (5.24)$$

$$\text{Overpressurzation : } p_{\text{in}} = \begin{cases} -5, & t = 0 \text{ (hr)} \\ 15, & 0 < t \leq 72 \text{ (hr)} \end{cases} \quad (5.25)$$

For each of these cases, the simulation is run using two different soil types - sand and sandy loam. Sand is assumed here to not sorb any TCE, while for sandy loam a range of sorption isotherms are used. These range from no sorption ( $K_{\text{ads}} = 0 \text{ (m}^3/\text{kg})$ ) to the experimentally determined sorption isotherm for Appling soil ( $K_{\text{ads}} = 5.28 \text{ (m}^3/\text{kg})$ ). With the experimentally determined isotherm, we see that the ratio between sorbed concentration and soil-gas phase concentration is 7708, i.e. there is a much larger amount of contaminant sorbed to the soil than present in the vapor phase of the vadose zone. When  $K_{\text{ads}} = 5.28 \cdot 10^{-4} \text{ (m}^3/\text{kg})$  this ratio is roughly unity (0.77).

The top panel of Figure 5.4 shows the indoor air contaminant concentration as the simulated building is undergoing the depressurization as represented by the equation (5.24) case.

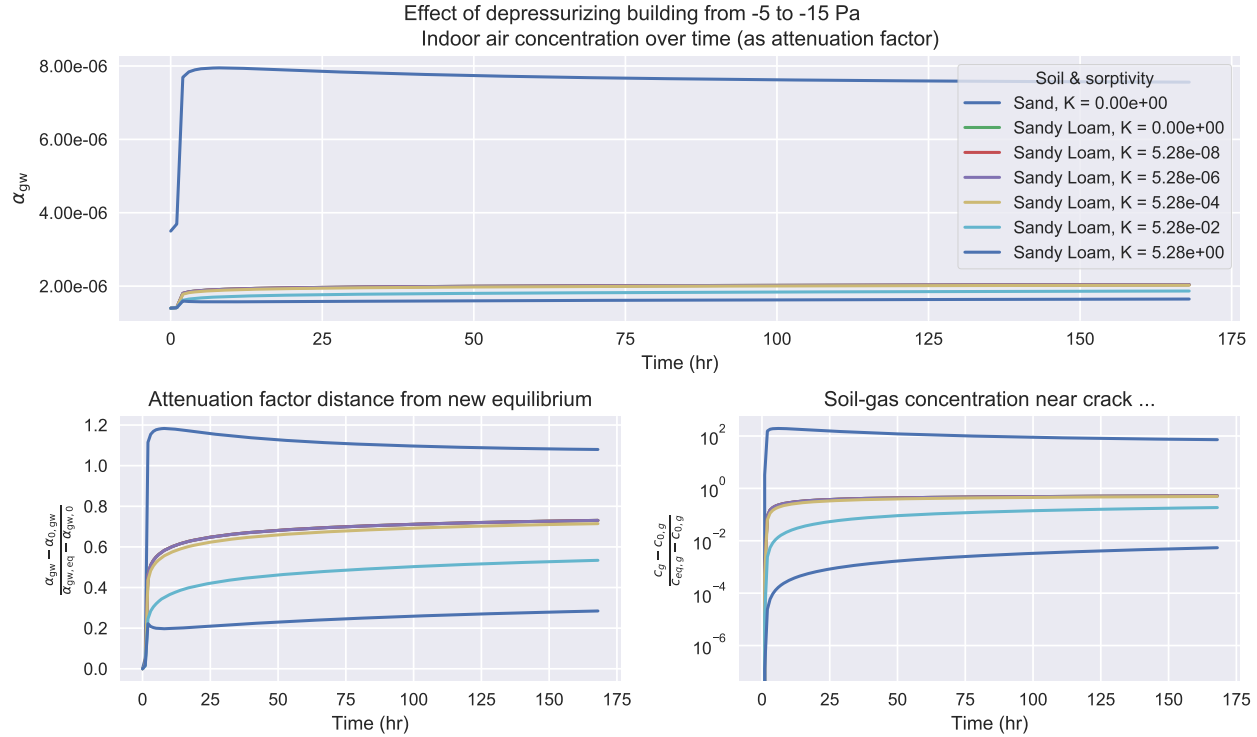


Figure 5.4: The influence of contaminant sorption in soil. The top panel shows the effect of a step change in depressurization on attenuation factor relative to groundwater, as a function of sorption coefficient. The lower left panel shows the corresponding changes in attenuation factor with time, shown as a degree of approach to new equilibrium. The lower right panel shows the corresponding change in absolute contaminant concentration immediately adjacent to the building foundation breach.

results are plotted as attenuation of contaminant relative to the groundwater source, i.e.

$$\alpha_{gw} = \frac{c_{in}}{c_{gw} K_H} \quad (5.26)$$

Here we can see that when the surrounding soil consists of sand, the indoor concentration increases rapidly as the building is depressurized. The increase is significantly smaller for the sandy loam cases, and becomes smaller as the sorbed mass increases ( $K_{ads}$  increases).

The bottom left panel shows the time for reaching the new equilibrium. At the start of the simulation, the building starts at an attenuation of  $\alpha_{gw,0}$ , which is the steady-state concentration when the building is depressurized to -5 Pa. As the building is further depressurized to -15 Pa, the indoor air concentration will approach a new equilibrium state  $\alpha_{gw,eq}$

(the result of which is obtained from a steady-state simulation at that depressurization). By plotting  $\frac{|\alpha_{\text{gw}} - \alpha_{\text{gw},0}|}{|\alpha_{\text{gw,eq}} - \alpha_{\text{gw},0}|}$  we can see how far away we are from the new equilibrium state, and a value of 0 represents that we are at the initial concentration, i.e.  $\alpha_{\text{gw}} = \alpha_{\text{gw},0}$ , and a value of 1 represents  $\alpha_{\text{gw}} = \alpha_{\text{gw,eq}}$ , i.e. that the new equilibrium has been reached. This demonstrates that times of hundreds of hours may be needed to attain a near steady-state

The results of the same calculations are shown in the bottom right panel as well, but instead of plotting the indoor air concentration, we consider the average soil-gas concentration in a 5 cm diameter cylinder that envelops the entire perimeter crack. The choice of 5 cm is arbitrary, but helps illustrate what happens in the near-foundation-crack region. Examining these changes allow us to better understand how the contaminant is transported into the building from the soil. Consistent with the long timescales for the indoor air to "adjust" to a new condition, the soil which is a significant source/sink for the contaminant share a similar slow adjustment.

Before discussing the role of sorption, we can first compare the non-sorbing sand and sandy loam cases. Due to its higher permeability and lower moisture content, sand is significantly more permeable to gas flow than sandy loam (see Table B.1 for permeability values). Consequently the advective transport through the foundation crack is much more significant in the sand case than the sandy loam case. This may be characterized by a Péclet number for transport through the foundation crack, where

$$\text{Pe} = \frac{\text{advection}}{\text{diffusion}} = \frac{u_{\text{ck}} L_{\text{slab}}}{D_{\text{air}}} \quad (5.27)$$

and the Péclet number is around 4 versus 0.2 at a -15 Pa depressurization for sand and sandy loam respectively. A Péclet greater than one indicate that advective transport dominates and vice versa.

Due to the advection dominated transport mechanism in the sand case, the indoor air concentrations are temporarily elevated above the final equilibrium concentration at -15 Pa.

(Note that the absolute distance from equilibrium is plotted in Figure 5.4 which is why the concentration is two order of magnitude displaced.) This phenomena occurs because initially more contaminants are drawn into the building from the near crack area than can be resupplied, temporarily depleting the local soil-gas contaminant concentration.

One can notice that many of the sandy loam lines overlap, and start diverging from each other when  $K_{\text{ads}} = 5.28 \cdot 10^{-4}$  (m<sup>3</sup>/kg), at the point where the ratio of sorbed and soil-gas concentration are roughly equal. Since the indoor air concentration depend on the soil-gas concentration, this is the origin of the difference.

The reason for this is that it is at this threshold the that sorptive contribution to the retardation factor (5.12) starts to becomes larger than the other terms.

$$\rho_b K_H K_{\text{ads}} > \theta_w + \theta_g K_H \quad (5.28)$$

Thus it is at this point that the contaminant transport, i.e. replenishment from the source in the soil starts to become retarded by sorption. The partitioning between the various phases controls residence time as the contaminant is transported. Under VI conditions, the values of  $\theta_w + \theta_g K_H$  are relatively small values, while  $K_{\text{ads}}$  can vary by orders of magnitude, making sorption potentially a very significant retarder for soil transport.

We can also note that the retarding effect of sorption also somewhat depends on the contaminants Henry's Law constant  $K_H$ , bulk density  $\rho_b$  and the moisture content  $\theta_w$ . For instance if the local temperature is higher, then contaminant  $K_H$  is likewise larger, and the retardation factor is greater. Generalizing this is difficult however, as  $K_{\text{ads}}$  decreases with temperature, and the interplay between these may be complicated. Nevertheless this hints that there may be a climate/weather component to how significantly sorption induced retardation is.

Figure 5.5 shows the same sort of analysis as in Figure 5.4 but with the building pressurization as described by (5.25). As the building is overpressurized, the indoor contaminant is

pushed back out into the soil. Since the indoor air concentration is lower than the soil-gas concentration, a drop in local soil-gas concentration is observed along with a decrease in indoor air contaminant concentration.

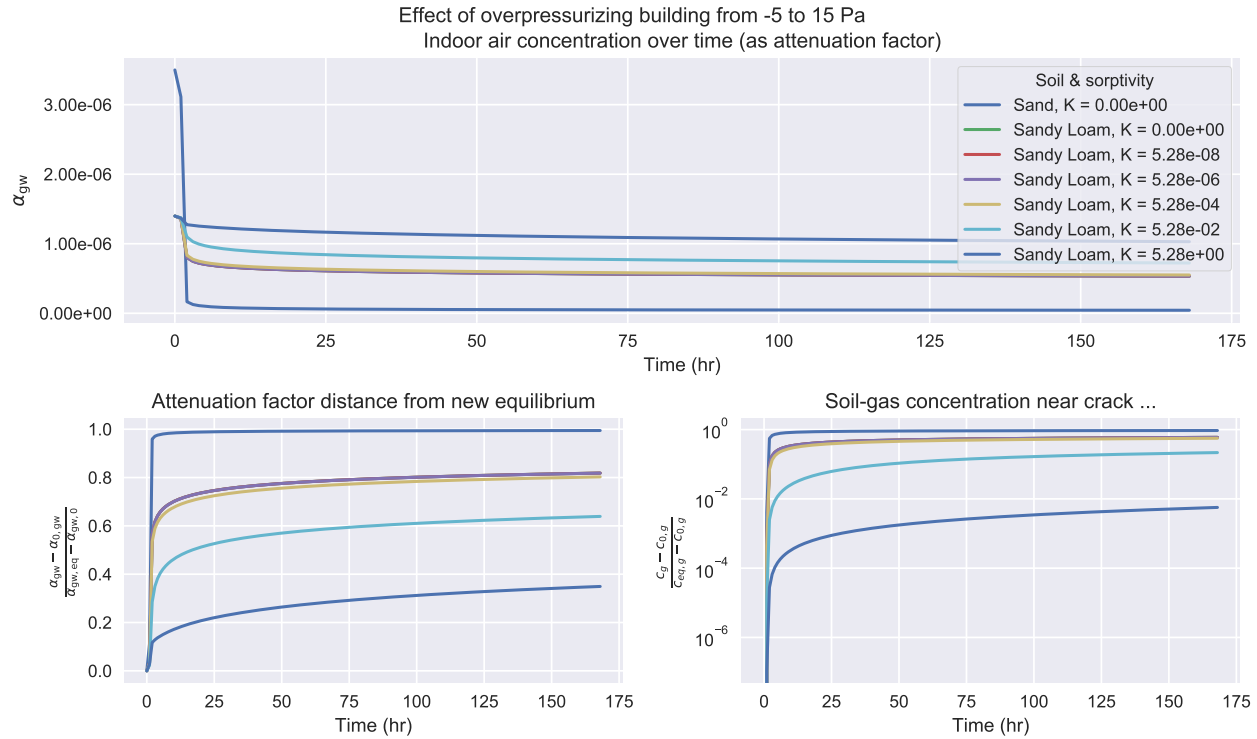


Figure 5.5: The influence of contaminant sorption in soil. The top panel shows the effect of a step change from building depressurization to pressurization on attenuation factor relative to groundwater, as a function of sorption coefficient. The lower left panel shows the corresponding changes in attenuation factor with time, shown as a degree of approach to new equilibrium. The lower right panel shows the corresponding change in absolute contaminant concentration immediately adjacent to the building foundation breach.

### 5.4.3 Effects of Indoor Material Sorption

For these simulations we assume that there is no soil sorption. We consider the basement (the indoor air space) and assume that the inside surfaces are entirely made up of one of the materials we presented in 5.4.1. We also assume that the material covering the indoor surfaces has a certain thickness or depth that the contaminants can penetrate - providing a certain volume or mass of sorbing material in the indoor environment. Table 5.2 shows the

surface area, penetration depth, and volume of each material studied. While the assumptions regarding coverage of different portions of the space are arbitrary, they are of the right order of magnitude and they do present some limiting cases of the potential effect of sorption onto/from these materials.

Material	$d_p$ (mm)	$V_{\text{mat}}$ ( $\text{m}^3$ )
Cinderblock	5	1.6
Wood	1	0.32
Drywall	10	3.2
Carpet	10	3.2
Paper	0.1	0.032

Table 5.2: The assumed contaminant penetration depth and subsequent volume of the sorbing indoor materials. The material surface area is assumed to be the same, and each material completely cover the surfaces of a 10x10x3 meter room.

The modeled building then undergoes a pressurization cycle, in which at start of the simulation it has been depressurized at -5 Pa at steady-state. The building is then sequentially depressurized to -15 Pa, then pressurized to 15 Pa, and finally again depressurized to -5 Pa. For each sequence, the new pressurization is maintained for 24 hours. This pressurization cycle may be seen in the top left panel of 5.6. The choice of pressurization cycle is somewhat arbitrary, but can be used to represent limiting cases of natural pressurization variation, or artificially induced pressurization. Figure 5.6 shows the result of these simulations.

The change in indoor air contaminant concentration over this pressurization cycle is shown in the bottom panel of Figure 5.6. First we consider the reference case - where there is no sorbing indoor materials present. (The blue line is the reference case, which may be difficult to see as the wood and carpet lines overlap.) Here we see that as the building is depressurized, the indoor air contaminant concentration increases quickly in response to the depressurization change, and is approaching a new equilibrium.

The presence of the various studied building materials in the indoor environment have very different effects on the change in indoor air contaminant concentration. The presence of wood and carpet has little effect on the indoor air concentration, whereas cinderblock has

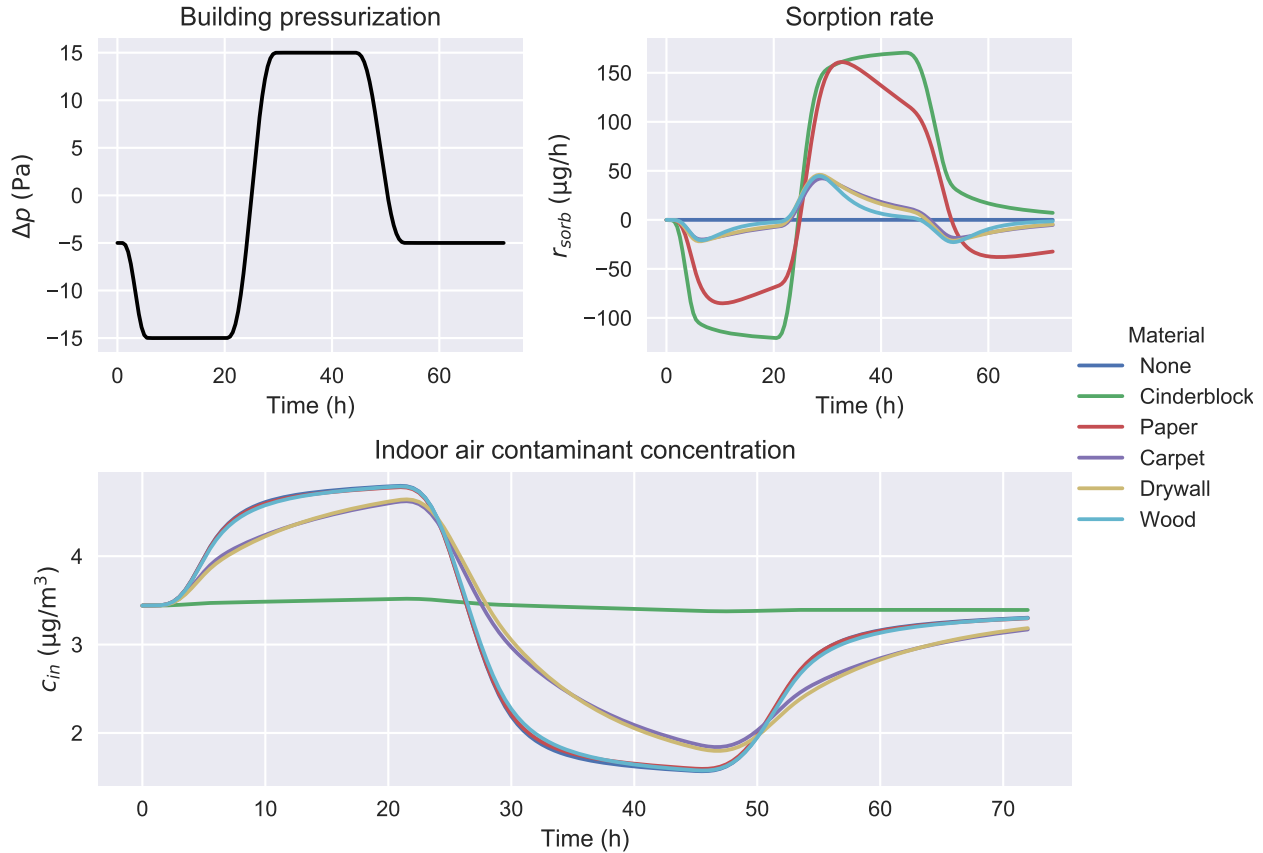


Figure 5.6: Comparison of how sorption onto/from various indoor materials affect the indoor air contaminant concentration (bottom) of a building that undergoes a pressurization cycle (top left). The rate of de- and sorption for each considered material during the cycle are also shown (top right) and is governed by (5.31). A positive value means that contaminant vapors are being sorbed onto/into the material and a negative means the material is desorbing into the indoor air space.

a very significant effect, dampening out almost any change in indoor concentration. Drywall and carpet significantly delay the rate of change in the indoor concentration, but for each 24 hour cycle, roughly the same indoor concentration is reached as in the no sorbing material reference case.

The disparity in these results is explained by the top right panel of Figure 5.6. Here the de- and sorption rates in  $\mu\text{g}/\text{hr}$  for each indoor material is shown. A positive and negative value here indicate that contaminant is desorbed from or sorbed to the material respectively. To understand this figure, it is useful to refer back to Table 5.1 which shows the sorption and desorption rate constant  $k_1$  and  $k_2$  respectively, and the sorption equilibrium constant

$K$  (a larger value indicate a larger sorptive capacity).

First we consider to the depressurization part of the cycle (1-25 hours). As in the indoor concentration panel, we see that the wood, drywall, and carpet cases overlap. These materials have similar sorptive capacities ( $K$ ) and sorptive rates ( $k_2$ ). Paper, by contrast, has a similar shape to the previous three but its magnitude is significantly larger. This is because the  $K$  value for paper is one order of magnitude larger, indicating that wood, drywall, and carpet saturate with contaminant vapors over the time period, while paper does not. Cinderblock has a further order of magnitude larger  $K$  value, thus is even further away from being saturated, which is consistent with its even faster sorption rate.

Next we consider the overpressurization period (25-49 hours). Again we see here that wood, drywall, and carpet behave the similarly. This means that these reach the new contaminant saturation equilibrium at roughly the same time.

Here it is important to note that due to diffusion dominated transport through the foundation crack, even though the building is overpressurized, there is still substantial contaminant entry. And because the sole contaminant source is contaminated groundwater, the sorbed equilibrium is determined by this entry rate.

Paper and cinderblock initially behave very similarly during the overpressurization period and desorb contaminants quickly. However, paper reaches its saturation limit after a relatively short time, while cinderblock has not even at the end of the overpressurization cycle. Since the desorption rate constants  $k_2$  are relatively similar for the materials, this disparity is primarily due to the different sorption equilibrium constants  $K$ .

Lastly, we consider the final period where the pressurization goes back to its initial state (49-72 hrs). Here we see that the reference case does not quite return to the initial indoor concentration. Thus the contaminant entry rate has not equilibrated yet, because the soil contaminant concentration has not done so either. As in the previous analysis we again see that the wood, drywall, and carpet cases don't differ from the reference. Paper is slightly different, for the same reasons that have already been discussed. Cinderblock is unique here,

as it is releasing contaminants, due to the previous change in contaminant concentration. In other words, it is acting as a significant capacitance in the system.

From this simulation work the varied the effects of sorbing indoor materials are apparent. Most of the tested materials only have a moderate effect on the indoor air contaminant concentration dynamics, with the notable exception of cinderblock, which effectively maintains as pseudo-steady-state. However we also see from the analysis of the sorption dynamics that the desorption and sorption rate constants  $k_1$  and  $k_2$  are less important than the overall sorptive capacity  $K$  of the material.

#### 5.4.4 Indoor Material Sorption And Mitigation

The work done by us and others has shown the large sorptive capacities of various common materials. The desorption of the sorbed contaminants may have significant impact on the apparent efficacy of various mitigation systems. To investigate this we consider a scenario where initially the modeled building is depressurized at -5 Pa and at the start of the simulation some perfect mitigation scheme is implemented and the contaminant entry  $n_{\text{entry}}$  in (5.29) goes to zero. We also assume that for each case, the indoor environment contains the same amount of indoor material as described in section 5.4.3. The air exchange rate is assumed to remain a constant 0.5 per hour for the entire simulation time.

Hence, we can drop  $n_{\text{ck}}$  in (5.29) and the equations used to model the indoor concentration becomes:

$$V_{\text{bldg}} \frac{\partial c_{\text{in}}}{\partial t} = A_e c_{\text{in}} V_{\text{bldg}} - r_{\text{sorb}} V_{\text{mat}} \quad (5.29)$$

$$V_{\text{mat}} \frac{\partial c_{\text{sorb}}}{\partial t} = r_{\text{sorb}} V_{\text{mat}} \quad (5.30)$$

$$r_{\text{sorb}} = k_1 c_{\text{in}} - k_2 c_{\text{sorb}} \quad (5.31)$$

This system of ordinary differential equations can be solved analytically. A solution to this

is

$$\begin{bmatrix} c_{\text{in}} \\ c_{\text{sorb}} \end{bmatrix} = A \exp(\lambda_1 t) \vec{v}_1 + B \exp(\lambda_2 t) \vec{v}_2 \quad (5.32)$$

and finding the eigenvalues ( $\lambda_1, \lambda_2$ ) and eigenvectors ( $\vec{v}_1, \vec{v}_2$ ) of the system above, allows us to calculate the indoor and sorbed contaminants concentrations through time.  $A$  and  $B$  are constants found using the initial conditions

$$c_{\text{in}}(t = 0) = c_{\text{in},0} \rightarrow A \quad (5.33)$$

$$c_{\text{sorb}}(t = 0) = c_{\text{sorb},0} K \rightarrow B \quad (5.34)$$

where we assume that  $c_{\text{in},0} = 2 \text{ } (\mu\text{g}/\text{m}^3)$ .

The decrease in indoor air concentration (as attenuation factor  $\alpha_{\text{gw}}$ ) for each case is seen in the top panel of Figure 5.7. As expected, when there is no sorbing indoor materials, i.e. our reference case, the indoor concentration decreases log-linearly. We can also see that contaminant desorption from materials maintains a higher indoor air concentration relative to reference, with cinderblock again shown to have the great impact.

Clearly, the contaminant desorption from indoor materials can significantly delay the time that a certain reduction in indoor air concentration after a successful mitigation system has been implemented. In the bottom panel of Figure 5.7 we quantified the number of hours for a fifty percent, a one, and two orders of magnitude reduction in indoor air concentration to occur, both absent sorbing indoor materials (the reference case) and in the presence of the ones presented earlier in this work. On the x-axis the indoor air concentration reduction factor is shown, and on the y-axis the number of hours for the specified reduction occur is displayed, for each material. The number of hours for each case are also shown at the top of each bar.

From this, we see that it takes 1.4 hours for the a 50% reduction in indoor air concentration to occur for the reference, paper, and wood cases, while this time increases up to

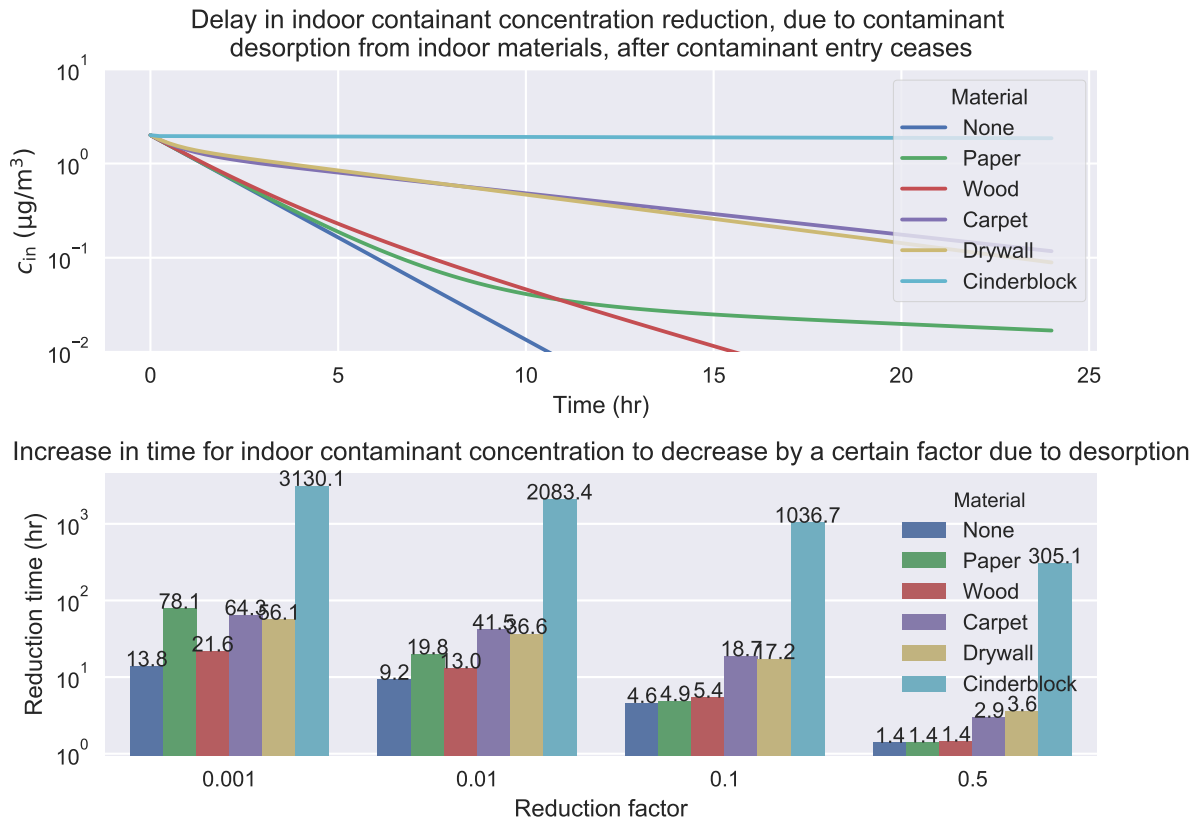


Figure 5.7: Contaminant desorption from indoor materials delay the decrease in indoor contaminant concentration after a mitigation system has been implemented. The top panel shows the indoor air concentration after system implementation, considering desorption from different materials. The bottom panel quantifies how long it takes for the indoor concentration to decrease by a certain factor, considering the different cases.

305 hours in the cinderblock case. This indicates the significant effect that sorption of TCE onto cinderblock can potentially have on the efficacy on a VI mitigation scheme, with the remaining materials having a relatively minor or moderate effect; a trend we have seen in other parts of this work.

## 5.5 Conclusions

The work presented here offers new insights into how sorption effect may influence VI; exploring how sorption affects VI fundamentally and in some applications. Based on what has been presented here, we can draw some conclusions.

- The sorption and desorption kinetics, while they vary quite a bit, do not seem to make a significant difference in most VI applications or cases, at least not the ones considered here. But, what has been apparent is that it is the sorption capacities of the particular material that matters, although these seem to have to be on the same scale as cinderblock to truly be significant.
- The sorptive capacities of materials vary significantly and it may not be obvious which ones have large sorptive capacities and which do not. More materials, in combination with other contaminants, need to be tested to gain a more comprehensive understanding of which materials are of particular concern in VI.
- Sorption fundamentally retards contaminant transport in soils, effectively increasing the residence time of the contaminant in the soil. However, sorption will only start to retard transport if the sorption partition coefficient is large enough to exceed the "naturally" induced residence by the soil moisture content. Sorption on materials in the indoor environment functions in a similar way, and like a capacitance, inhibits changes in indoor concentration. These particular phenomena may be relevant to consider if one wants to try to influence the contaminant transport and entry rate into the building via forceful pressurization of the building, e.g. the controlled pressure method, as these attempts may be less effective than expected due to sorption.
- Contaminant desorption from indoor materials may also have a significant effect of mitigation systems, potentially delaying effective mitigation from taking place from a matter of hours to several days or weeks, depending on the amount and kind of indoor materials present.

# Chapter 6

## Conclusions and Future Work

### 6.1 Summary of Results

Throughout this thesis, actual field investigation results have been presented from vapor intrusion impacted buildings. The results shown here were among the most carefully collected and analyzed results in the vapor intrusion field. And yet, those results still left those who collected them puzzling about what they meant, and how they could be generalized to other VI sites where the expenditure of such detailed characterization efforts is out of the question. This is what led to the conclusion that application of advanced numerical modeling is necessary, in order to begin to make sense out of what otherwise looks difficult to explain or even chaotic. This was the starting point for this effort.

As summarized in this thesis, this is by no means the first effort at numerical modeling of vapor intrusion. But the reality in the field has been that most numerical models have been designed to study the steady state, which as shown with the field data, is almost invariably not the case. So we have built in the capacity to model transient VI phenomena, something that has not been emphasized before. But beyond that, we have been able to use the numerical modeling to begin to develop a better sense of what parameters are key to determining the results seen at different sites. It was only through such modeling that the

concepts of "advection" vs. "diffusive" entry were identified, and begin to suggest how to categorize sites which will respond very differently to the different kinds of field tests that are being performed.

In this work a framework for creating numerical models of vapor intrusion (VI) scenarios has been presented. These models are able to simulate contaminant transport from a source into a building through soils, while taking site specific characteristics, soil moisture, and heterogenous soils into account. Sorption effects, biodegradation, and other phenomena, at both steady state and in time dependent simulations can also be taken into consideration.

These models have been used to explore the temporal and spatial variability that has been observed at VI sites, and in particular the variability associated with preferential pathways like that at the ASU house site. It was demonstrated that preferential pathways may contribute significantly to temporal variation of indoor contaminant concentration, and VI in general, by greatly enhancing the role of advective contaminant transport into a building. This in turn required that three conditions to be satisfied:

1. A ready source of air must be supplied.
2. Likewise, a preferential source of contaminant vapors must be supplied.
3. A permeable zone, e.g. a gravel layer, between the preferential pathway and indoors must exist to facilitate transport.

With the revelation that significant temporal variability of indoor contaminant concentration being associated with advective transport of vapors into a building, we explored the potential for various soils to support sufficient airflow rates such that advection dominate entry. Twelve different soil types were considered, and compared for a house featuring a basement, and on that had a slab-on-grade type foundation. Regardless of foundation type, only sandy type soils can be expected to be permeable enough to support airflow for advective transport to dominate. Thus, various site specific characteristics, such as preferential

pathways (but not necessarily limited to these) are needed for the elevated airflow rates required for advection to dominate.

It is important to consider if advective or diffusive transport dominates at a site, as the association between building pressurization and contaminant entry are very different for each. For sites characterized by advection, this association is likely to be strong, and it is weak at diffusion dominated sites. Consequently, the application of VI investigation techniques like the controlled pressure method are likely to only be effective at advection dominated sites.

Another consequence is that for advection dominated sites, building pressurization can be used as an effective metric for determining when indoor contaminant concentrations are likely to be the highest. We also showed that building pressurization in turn can be predicted relatively easily based on indoor/outdoor temperature differences and wind effects. As the indoor/outdoor temperature differences increases, i.e. it is warmer inside than outside, a building is increasingly depressurized; which is likely why for many sites indoor contaminant concentration are higher during winter.

The trichloroethylene (TCE) sorption capacity of a variety of common materials was measured at relevant contaminant concentration, showing that some of these materials can contain significant amounts of TCE; cinderblock was able hold up to almost 41,000 times more contaminant than a comparable TCE contaminated air volume. These sorptive data were then used to explore the role of sorption in some modeled VI scenarios. The modeling showed the significant retarding effect on contaminant transport, due to the increased residence time in the soil pores, that soil sorption can have.

It was also shown that significant amounts of contaminants can be sorbed in the indoor environment, and in some cases maintain a pseudo steady-state, where contaminant vapors are sorbed or desorbed with changing indoor contaminant concentrations. In a situation where a VI site has been effectively mitigated, i.e. contaminant entry into the building completely stopped, the contaminant desorption from indoor materials can maintain signif-

icant indoor contaminant concentrations even weeks after the mitigation system has been implemented.

The work herein presented shows the value of this type of advanced numerical modeling in a field that is otherwise characterized by field studies of VI sites. The nature and heterogeneity of these sites renders it difficult to control for any given condition or variable, which is a hindrance for developing generalizable conclusions. The type of modeling used here shows that even with relatively simple models based on VI sites, it is possible to capture much of the observed physical behavior. This allows us to use these same models as an effective complimentary tool for investigating various VI related phenomena, and determining how sensitive VI is to site specific conditions and other variables.

Recently, the use of models have somewhat fallen out of favor in the VI community. One reason for this is that they have simply been inadequate in addressing and explaining the observed VI phenomena at VI sites. This has been particularly true for characterizing temporal and spatial variability. However, it is important to remember that VI models used by investigators and regulators are of the analytical variety. While many of these offer good insights, they are limited as they simply cannot be modified beyond their underlying conceptual site model (CSM) and assumptions. For instance, the popular Johnson and Ettinger model cannot capture the behavior of a land drain, such as we could in this work, simply because one is not assumed to exist, and the user can do little to address this.

The advanced numerical model used in this thesis, while relatively simple and often borrow many aspects of the CSMs that underpin analytical models, can be extended to include site features or conditions that are impossible for analytical models. There is nothing technically preventing numerical models from simulating a VI site in great details, and characterizing not only the specific building, but can also include a full accounting of soil heterogeneity, e.g. by including clay layers, larger rock formations, or other subsurface features, which have a significant impact on VI. Numerical models are necessary if one wishes to model a site in any specific way.

Numerical modeling should play a much larger role in VI investigations as they can be used to develop more advanced and realistic CSMs. For instance, an investigator can go to a site, develop a CSM based on initial observations, construct a model and gain some predictions of how the site may be expected to behave. If there is some disparity between the model and reality, this may indicate that there is something missing from the CSM, e.g. does the indoor contaminant concentration temporal variability suggest that there is a preferential pathway? Different cases that aim to explain the disparity can then be constructed as a means to guide the site investigation. Ultimately, the use of numerical models of VI sites are a great tool that can greatly shorten the time required to determine human VI risk and at the same time reduce the uncertainty of determining this.

## 6.2 Suggestions for Future Research

### 6.2.1 Advection Transport and Specific Site Characteristics

It has been shown that most soils are not permeable enough to provide enough airflow for advective transport of contaminant vapor from the subsurface into building to dominate, and such conditions are most likely to arise as a result of some site specific characteristic, such as existence of a preferential pathway. However, more of these site specific characteristics needs to be explored to gain a more holistic view of which one's are likely to be important during a VI site investigation. Some examples of cases in which significant additional air flow may be possible include those in which there are:

- Gravel backfills around a building
- French drains (or similar)
- Disturbed or unpacked soil around the building
- Air pulled through a permeable layer that connects two adjacent buildings, i.e. can one building use another as a preferential air source?

### 6.2.2 Preferential Pathways

More types of sewer connected preferential pathways should be considered. For instance, at the EPA duplex, it is likely that the sewer line there leaked a few meters away from the edge of the duplex, and existence of a leaky preferential pathway should be considered.

### 6.2.3 Sorption and Vapor Intrusion

Sorption is a relatively unexplored phenomena in VI, but has been shown to potentially have significant consequences, in particular with regards to mitigation of VI at a building. More work is needed to collect sorptive capacities of more materials, considering a greater variety of VI contaminant (at relevant vapor concentrations).

### 6.2.4 Modeling and Design of Mitigation Systems

Mitigating VI at a site is obviously an important task, but it is not always clear what type of mitigation system design is most appropriate for a given site. Modeling may here offer insights on optimizing a mitigation system design. A mitigation system was installed at the EPA duplex during the latter of that study, and its rich dataset offers an excellent opportunity to examine the efficacy of various designs using modeling.

### 6.2.5 Model Effects of Weather and Seasons on Vapor Intrusion

In this work, we considered how temperature and wind pressurizes a building relative to ambient, which help explain some of the seasonal trends observed at some VI sites. This work should be expanded to consider other weather phenomena, such as rainfall, snow coverage, or other, to gain a more holistic view of how VI and weather are related.

# Bibliography

- [1] Neil E Klepeis et al. “The National Human Activity Pattern Survey (NHAPS): A Resource for Assessing Exposure to Environmental Pollutants”. en. In: *Journal of Exposure Science & Environmental Epidemiology* 11.3 (July 2001). 02256, pp. 231–252. ISSN: 1559-0631, 1559-064X. DOI: 10.1038/sj.jea.7500165.
- [2] Craig D. Hollowell et al. *COMBUSTION- 'GENERATED INDOOR AIR POLLUTION I. FIELD MEASUREMENTS 8/75- 10/75*. Tech. rep. W-7405-ENG-48. 00040. U. S. Energy Research and Development Administration, Jan. 1976.
- [3] World Health Organisation, ed. *WHO Guidelines for Indoor Air Quality: Household Fuel Combustion*. en. 00000 OCLC: 932123287. 2014. ISBN: 978-92-4-154887-8 978-92-4-154888-5.
- [4] World Health Organisation, ed. *WHO Guidelines for Indoor Air Quality: Dampness and Mould*. en. 00000 OCLC: 699067228. Copenhagen: World Health Organization, Regional Office for Europe, 2009. ISBN: 978-92-890-4168-3.
- [5] *Health Hazards Associated with Elevated Levels of Indoor Radon – Pennsylvania*. <https://www.cdc.gov> 00004.
- [6] Gaskin Janet et al. “Global Estimate of Lung Cancer Mortality Attributable to Residential Radon”. In: *Environmental Health Perspectives* 126.5 (). 00019, p. 057009. DOI: 10.1289/EHP2503.

- [7] U.S. Environmental Protection Agency. *OSWER Technical Guide for Assessing and Mitigating the Vapor Intrusion Pathway From Subsurface Vapor Sources To Indoor Air*. 00012. 2015.
- [8] B. Schumacher et al. *Fluctuation of Indoor Radon and VOC Concentrations Due to Seasonal Variations*. 00002. July 2012.
- [9] Lilian D. V. Abreu and Paul C. Johnson. "Simulating the Effect of Aerobic Biodegradation on Soil Vapor Intrusion into Buildings: Influence of Degradation Rate, Source Concentration, and Depth". In: *Environmental Science & Technology* 40.7 (Apr. 2006). 00103, pp. 2304–2315. ISSN: 0013-936X. DOI: 10/czwj8v.
- [10] OLEM US EPA. *Current NPL Updates: New Proposed NPL Sites and New NPL Sites*. en. <https://www.epa.gov/superfund/current-npl-updates-new-proposed-npl-sites-and-new-npl-sites>. Policies and Guidance. 00000. Aug. 2015.
- [11] OLEM US EPA. *What Is Vapor Intrusion?* en. <https://www.epa.gov/vaporintrusion/what-vapor-intrusion>. Overviews and Factsheets. 00000 Library Catalog: www.epa.gov. Sept. 2015.
- [12] Susan L. Makris et al. "A Systematic Evaluation of the Potential Effects of Trichloroethylene Exposure on Cardiac Development". In: *Reproductive Toxicology* 65 (2016). 00013, pp. 321–358. ISSN: 08906238. DOI: 10/f8879q.
- [13] Jonathan D. Urban et al. "Systematic Evaluation of Mechanistic Data in Assessing in Utero Exposures to Trichloroethylene and Development of Congenital Heart Defects". en. In: *Toxicology* 436 (Apr. 2020). 00000, p. 152427. ISSN: 0300-483X. DOI: 10.1016/j.tox.2020.152427.
- [14] R. Meininghaus, L. Gunnarsen, and H. N. Knudsen. "Diffusion and Sorption of Volatile Organic Compounds in Building Materials-Impact on Indoor Air Quality". In: *Environmental Science & Technology* 34.15 (Aug. 2000). 00129, pp. 3101–3108. ISSN: 0013-936X. DOI: 10.1021/es991291i.

- [15] R. Meininghaus and E. Uhde. “Diffusion Studies of VOC Mixtures in a Building Material”. en. In: *Indoor Air* 12.4 (Dec. 2002). 00057, pp. 215–222. ISSN: 0905-6947, 1600-0668. DOI: 10.1034/j.1600-0668.2002.01131.x.
- [16] Chase Holton et al. “Creation of a Sub-Slab Soil Gas Cloud by an Indoor Air Source and Its Dissipation Following Source Removal”. en. In: *Environmental Science & Technology* 52.18 (Aug. 2018). 00000, pp. 10637–10646. ISSN: 0013-936X, 1520-5851. DOI: 10/gd569z.
- [17] David Folkes et al. “Observed Spatial and Temporal Distributions of CVOCs at Colorado and New York Vapor Intrusion Sites”. en. In: *Ground Water Monitoring & Remediation* 29.1 (Jan. 2009). 00050, pp. 70–80. ISSN: 1745-6592. DOI: 10/fw6kxz.
- [18] Yijun Yao et al. “Examination of the Influence of Environmental Factors on Contaminant Vapor Concentration Attenuation Factors Using the U.S. EPA’s Vapor Intrusion Database”. In: *Environmental Science & Technology* 47.2 (Jan. 2013). ZSCC: 0000032, pp. 906–913. ISSN: 0013-936X. DOI: 10/f4jb29.
- [19] Hong Luo et al. “Spatial Variability of Soil-Gas Concentrations near and beneath a Building Overlying Shallow Petroleum Hydrocarbon-Impacted Soils”. en. In: *Ground Water Monitoring & Remediation* 29.1 (Jan. 2009). 00000, pp. 81–91. ISSN: 1745-6592. DOI: 10/bkjstw.
- [20] Dawit N. Bekele, Ravi Naidu, and Sreenivasulu Chadalavada. “Influence of Spatial and Temporal Variability of Subsurface Soil Moisture and Temperature on Vapour Intrusion”. In: *Atmospheric Environment* 88 (May 2014). 00009, pp. 14–22. DOI: 10/f52sht.
- [21] Kelly G. Pennell et al. “Sewer Gas: An Indoor Air Source of PCE to Consider During Vapor Intrusion Investigations”. en. In: *Groundwater Monitoring & Remediation* 33.3 (Aug. 2013). 00022, pp. 119–126. ISSN: 1745-6592. DOI: 10/gd6dd9.

- [22] Thomas McHugh et al. "Evidence of a Sewer Vapor Transport Pathway at the USEPA Vapor Intrusion Research Duplex". In: *Science of The Total Environment* 598 (Nov. 2017). 00009, pp. 772–779. ISSN: 0048-9697. DOI: 10/gd6dfz.
- [23] Yuanming Guo et al. "Identification of Alternative Vapor Intrusion Pathways Using Controlled Pressure Testing, Soil Gas Monitoring, and Screening Model Calculations". In: *Environmental Science & Technology* 49.22 (Nov. 2015). 00024, pp. 13472–13482. ISSN: 0013-936X. DOI: 10/f72b6n.
- [24] Chase Holton et al. "Temporal Variability of Indoor Air Concentrations under Natural Conditions in a House Overlying a Dilute Chlorinated Solvent Groundwater Plume". In: *Environmental Science & Technology* 47.23 (Dec. 2013). 00030, pp. 13347–13354. ISSN: 0013-936X. DOI: 10/gd6dfd.
- [25] Vitthal Hosangadi et al. "High-Frequency Continuous Monitoring to Track Vapor Intrusion Resulting From Naturally Occurring Pressure Dynamics". en. In: *Remediation Journal* 27.2 (Mar. 2017). 00002, pp. 9–25. ISSN: 1520-6831. DOI: 10/gd6df5.
- [26] D J Steck et al. "Indoor Radon Exposure Uncertainties Caused by Temporal Variation". en. In: (2004). 00017, p. 7.
- [27] Kelly G. Pennell et al. "Field Data and Numerical Modeling: A Multiple Lines of Evidence Approach for Assessing Vapor Intrusion Exposure Risks". In: *Science of The Total Environment* 556 (June 2016). 00008, pp. 291–301. ISSN: 0048-9697. DOI: 10/gd6dft.
- [28] Thomas McHugh, Per Loll, and Bart Eklund. "Recent Advances in Vapor Intrusion Site Investigations". In: *Journal of Environmental Management*. Global Trends in the Environmental Remediation Industry 204 (Dec. 2017). 00006, pp. 783–792. ISSN: 0301-4797. DOI: 10/gd6dgk.

- [29] Chase Holton et al. “Long-Term Evaluation of the Controlled Pressure Method for Assessment of the Vapor Intrusion Pathway”. In: *Environmental Science & Technology* 49.4 (Feb. 2015). 00011, pp. 2091–2098. ISSN: 0013-936X. DOI: 10/f64j45.
- [30] Thomas E. McHugh et al. “Evaluation of Vapor Intrusion Using Controlled Building Pressure”. In: *Environmental Science & Technology* 46.9 (May 2012). 00042, pp. 4792–4799. ISSN: 0013-936X. DOI: 10/f3xdtm.
- [31] Henry J. Schuver et al. “Chlorinated Vapor Intrusion Indicators, Tracers, and Surrogates (ITS): Supplemental Measurements for Minimizing the Number of Chemical Indoor Air Samples-Part 1: Vapor Intrusion Driving Forces and Related Environmental Factors”. en. In: *Remediation Journal* 28.3 (June 2018). 00000, pp. 7–31. ISSN: 10515658. DOI: 10/gfj55h.
- [32] W. W. Nazaroff. “Predicting the Rate of 222Rn Entry from Soil into the Basement of a Dwelling Due to Pressure-Driven Air Flow”. en. In: *Radiation Protection Dosimetry* 24.1-4 (Aug. 1988). 00064, pp. 199–202. ISSN: 0144-8420. DOI: 10.1093/oxfordjournals.rpd.a080269.
- [33] Paul C. Johnson and Robert A. Ettinger. “Heuristic Model for Predicting the Intrusion Rate of Contaminant Vapors into Buildings”. In: *Environmental Science & Technology* 25.8 (Aug. 1991), pp. 1445–1452. ISSN: 0013-936X. DOI: 10/d9cbhd.
- [34] Lilian D V Abreu and Paul C Johnson. “Effect of Vapor Source-Building Separation and Building Construction on Soil Vapor Intrusion as Studied with a Three-Dimensional Numerical Model”. In: *Environmental Science & Technology* 39.12 (2005). 00129, pp. 4550–4561. DOI: 10/fg6nx5.
- [35] Kelly G. Pennell, Ozgur Bozkurt, and Eric M. Suuberg. “Development and Application of a Three-Dimensional Finite Element Vapor Intrusion Model”. In: *Journal of the Air & Waste Management Association* 59.4 (2009). 00061, pp. 447–460. DOI: 10/fb9p72.

- [36] Rui Shen, Kelly G. Pennell, and Eric M. Suuberg. "Influence of Soil Moisture on Soil Gas Vapor Concentration for Vapor Intrusion". English. In: *Environmental Engineering Science* 30.10 (Oct. 2013). 00017 WOS:000325689400005, pp. 628–637. ISSN: 1092-8758. DOI: 10/gd6dfc.
- [37] Yijun Yao, Kelly G. Pennell, and Eric M. Suuberg. "Simulating the Effect of Slab Features on Vapor Intrusion of Crack Entry". In: *Building and Environment* 59 (Jan. 2013). ZSCC: 0000024, pp. 417–425. ISSN: 0360-1323. DOI: 10/f4ngrf.
- [38] Elham Shirazi and Kelly G. Pennell. "Three-Dimensional Vapor Intrusion Modeling Approach That Combines Wind and Stack Effects on Indoor, Atmospheric, and Sub-surface Domains". en. In: *Environmental Science: Processes & Impacts* 19.12 (Dec. 2017). 00000, pp. 1594–1607. ISSN: 2050-7895. DOI: 10/gd6df3.
- [39] Mats G. Larson and Fredrik Bengzon. *The Finite Element Method: Theory, Implementation and Applications*. 00157. Springer, 2010.
- [40] *Detailed Explanation of the Finite Element Method (FEM)*. <https://www.comsol.com/multiphysics/finite-element-method>. 00000.
- [41] C. W. Fetter. *Contaminant Hydrogeology*. 02621. New York : Toronto : New York: Macmillan Pub. Co. ; Maxwell Macmillan Canada ; Maxwell Macmillan International, 1993. ISBN: 978-0-02-337135-6.
- [42] Jacob Bear. *Dynamics of Fluids in Porous Media*. Environmental Science Series. 20692. New York: American Elsevier Pub. Co, 1972. ISBN: 978-0-444-00114-6.
- [43] COMSOL. *COMSOL Multiphysics Reference Manual v5.3a*. 00000.
- [44] COMSOL. *Subsurface Flow Module User's Guide v5.3a*. 00000.
- [45] Brian L. Murphy and Wanyu R. Chan. "A Multi-Compartment Mass Transfer Model Applied to Building Vapor Intrusion". In: *Atmospheric Environment* 45.37 (Dec. 2011). 00000, pp. 6650–6657. ISSN: 1352-2310. DOI: 10/dg3gqt.

- [46] R. H. Brooks and A. T. Corey. "Properties of Porous Media Affecting Fluid Flow". In: *Journal of the Irrigation and Drainage Division* 72.2 (1966). 02205, p. 61.
- [47] M. Th. van Genuchten. "A Closed-Form Equation for Predicting the Hydraulic Conductivity of Unsaturated Soils". In: *Soil Science Society of American* 44.5 (1980). 00008, pp. 892–898. doi: 10/fdc8mc.
- [48] S Fan and K M Scow. "Biodegradation of Trichloroethylene and Toluene by Indigenous Microbial Populations in Soil." In: *Applied and Environmental Microbiology* 59.6 (June 1993). 00000, pp. 1911–1918. ISSN: 0099-2240.
- [49] C. Deane Little et al. "Trichloroethylene Biodegradation by a Methane-Oxidizing Bacterium". In: *Applied and Environmental Microbiology* 54.4 (Apr. 1988). 00000, pp. 951–956. ISSN: 0099-2240.
- [50] Gorm Heron, Thomas H. Christensen, and Carl G. Enfield. "Henry's Law Constant for Trichloroethylene between 10 and 95 °C". en. In: *Environmental Science & Technology* 32.10 (May 1998). 00110, pp. 1433–1437. ISSN: 0013-936X, 1520-5851. doi: 10.1021/es9707015.
- [51] R. J. Millington and J. P. Quirk. "Permeability of Porous Solids". In: *Transactions of the Faraday Society* 57.0 (Jan. 1961). 01814, p. 1200. doi: 10/btx653.
- [52] Jeroen Provoost et al. "Accuracy of Seven Vapour Intrusion Algorithms for VOC in Groundwater". en. In: *Journal of Soils and Sediments* 9.1 (Feb. 2009). 00045, pp. 62–73. ISSN: 1439-0108, 1614-7480. doi: 10/dbp9fv.
- [53] W. W. Nazaroff et al. "Radon Transport into a Detached One-Story House with a Basement". In: *Atmospheric Environment (1967)* 19.1 (Jan. 1985). 00138, pp. 31–46. ISSN: 0004-6981. doi: 10.1016/0004-6981(85)90134-9.
- [54] van den Berg R. *Human Exposure to Soil Contamination: A Qualitative and Quantitative Analysis towards Proposals for Human Toxicological Intervention Values*. Tech.

- rep. 725201011. 00000. Bilthoven, Netherlands: National Institute of Public Health and Environmental Protection, Jan. 1994.
- [55] R. S. Anderssen, F. R. de Hoog, and B. R. Markey. “Modelling the Volatilization of Organic Soil Contaminants: Extension of the Jury, Spencer and Farmer Behaviour Assessment Model and Solution”. en. In: *Applied Mathematics Letters* 10.1 (Jan. 1997). 00014, pp. 31–34. ISSN: 0893-9659. DOI: [10.1016/S0893-9659\(96\)00106-1](https://doi.org/10.1016/S0893-9659(96)00106-1).
- [56] Ian Hers et al. “Evaluation of Vadose Zone Biodegradation of BTX Vapours”. en. In: *Journal of Contaminant Hydrology* 46.3 (Dec. 2000). 00114, pp. 233–264. ISSN: 0169-7722. DOI: [10.1016/S0169-7722\(00\)00135-2](https://doi.org/10.1016/S0169-7722(00)00135-2).
- [57] Yijun Yao et al. “A Review of Vapor Intrusion Models”. In: *Environmental Science & Technology* 47.6 (Mar. 2013). ZSCC: 0000055, pp. 2457–2470. ISSN: 0013-936X. DOI: [10/f4q3xr](https://doi.org/10/f4q3xr).
- [58] Ozgur Bozkurt, Kelly G Pennell, and Eric M Suuberg. “Simulation of the Vapor Intrusion Process for Nonhomogeneous Soils Using a Three-Dimensional Numerical Model”. In: *Ground Water Monitoring & Remediation* 29.1 (2009). 00068, pp. 92–104. ISSN: 1745-6592. DOI: [10/chswfm](https://doi.org/10/chswfm).
- [59] Yijun Yao, Kelly G. Pennell, and Eric Suuberg. “Vapor Intrusion in Urban Settings: Effect of Foundation Features and Source Location”. In: *Procedia Environmental Sciences*. Urban Environmental Pollution 2010 4 (Jan. 2011). 00000, pp. 245–250. ISSN: 1878-0296. DOI: [10/dhmt5h](https://doi.org/10/dhmt5h).
- [60] Yijun Yao et al. “Examination of the U.S. EPA’s Vapor Intrusion Database Based on Models”. In: *Environmental Science & Technology* 47.3 (Feb. 2013). ZSCC: 0000021, pp. 1425–1433. ISSN: 0013-936X. DOI: [10/gd6dd8](https://doi.org/10/gd6dd8).
- [61] Yijun Yao et al. “Estimation of Contaminant Subslab Concentration in Petroleum Vapor Intrusion”. In: *Journal of Hazardous Materials* 279 (Aug. 2014). 00017, pp. 336–347. ISSN: 0304-3894. DOI: [10/f6mf6v](https://doi.org/10/f6mf6v).

- [62] Rui Shen and Eric M. Suuberg. "Impacts of Changes of Indoor Air Pressure and Air Exchange Rate in Vapor Intrusion Scenarios". In: *Building and Environment* 96 (Feb. 2016). 00000, pp. 178–187. ISSN: 0360-1323. DOI: 10/f78xqf.
- [63] Iason Verginelli, Yijun Yao, and Eric M. Suuberg. "An Excel®-Based Visualization Tool of Two-Dimensional Soil Gas Concentration Profiles in Petroleum Vapor Intrusion". en. In: *Groundwater Monitoring & Remediation* 36.2 (May 2016). 00003, pp. 94–100. ISSN: 1745-6592. DOI: 10/gd6dfr.
- [64] Jill E. Johnston and Jacqueline MacDonald Gibson. "Spatiotemporal Variability of Tetrachloroethylene in Residential Indoor Air Due to Vapor Intrusion: A Longitudinal, Community-Based Study". En. In: *Journal of Exposure Science and Environmental Epidemiology* 24.6 (Nov. 2014). 00020, p. 564. ISSN: 1559-064X. DOI: 10/f6m5wc.
- [65] U.S. Environmental Protection Agency. *Assessment of Mitigation Systems on Vapor Intrusion: Temporal Trends, Attenuation Factors, and Contaminant Migration Routes under Mitigated And Non-Mitigated Conditions*. en. 00000. 2015.
- [66] Lynn Marie Hubbard and Nils Hagberg. "Time-Variation of the Soil Gas Radon Concentration under and near a Swedish House". In: *Environment International*. The Natural Radiation Environment VI 22 (Jan. 1996). 00026, pp. 477–482. ISSN: 0160-4120. DOI: 10.1016/S0160-4120(96)00148-1.
- [67] Paul C. Johnson et al. *Integrated Field-Scale, Lab-Scale, and Modeling Studies for Improving Our Ability to Assess the Groundwater to Indoor Air Pathway at Chlorinated Solvent-Impacted Groundwater Sites*. en. 00004. 2016.
- [68] Karin Birn Nielsen and Boerge Hvidberg. "Remediation Techniques for Mitigating Vapor Intrusion from Sewer Systems to Indoor Air". en. In: *Remediation Journal* 27.3 (June 2017). 00002, pp. 67–73. ISSN: 1520-6831. DOI: 10/gd6ddz.
- [69] *Indianapolis Research Duplex Total Database - Data.Gov*. <https://catalog.data.gov/dataset/indianapolis-research-duplex-total-database>. 00000.

- [70] Yuanming Guo. "Vapor Intrusion at a Site with an Alternative Pathway and a Fluctuating Groundwater Table". 00002. PhD Thesis. Arizona State University, 2015.
- [71] U.S. EPA. *Exposure Factors Handbook 2011 Edition*. en. Tech. rep. 00016. U.S. Environmental Protection Agency, 2011, p. 1436.
- [72] M. D. Koontz and H. E. Rector. *Estimation of Distributions for Residential Air Exchange Rates*. Tech. rep. 00027. U.S. Environmental Protection Agency, Mar. 1995.
- [73] Judith Chow et al. "Concentration of Tetrachloroethylene in Indoor Air at a Former Dry Cleaner Facility as a Function of Subsurface Contamination: A Case Study". In: *Journal of the Air & Waste Management Association* 57.6 (June 2007). 00000, pp. 753–760. ISSN: 1047-3289. DOI: 10/c6n8x9.
- [74] C. K. I. Williams. "Prediction with Gaussian Processes: From Linear Regression to Linear Prediction and Beyond". en. In: *Learning in Graphical Models*. Ed. by Michael I. Jordan. NATO ASI Series. 00679. Dordrecht: Springer Netherlands, 1998, pp. 599–621. ISBN: 978-94-011-5014-9. DOI: 10.1007/978-94-011-5014-9\_23.
- [75] Fabian Pedregosa et al. "Scikit-Learn: Machine Learning in Python". In: *Journal of Machine Learning Research* 12 (Oct. 2011). 24984, pp. 2825–2830. ISSN: 1533-7928.
- [76] Plotly Technologies Inc. *Collaborative Data Science*. 00000.
- [77] Ian Hers et al. "Evaluation of Seasonal Factors on Petroleum Hydrocarbon Vapor Biodegradation and Intrusion Potential in a Cold Climate". en. In: *Groundwater Monitoring & Remediation* 34.4 (Nov. 2014). 00017, pp. 60–78. ISSN: 1745-6592. DOI: 10/gd6dfg.
- [78] Órlaith Burke et al. "Estimation of Seasonal Correction Factors through Fourier Decomposition Analysis—a New Model for Indoor Radon Levels in Irish Homes". en. In: *Journal of Radiological Protection* 30.3 (Sept. 2010). 00019, pp. 433–443. ISSN: 0952-4746, 1361-6498. DOI: 10.1088/0952-4746/30/3/002.

- [79] J. Miles. "Temporal Variation of Radon Levels in Houses and Implications for Radon Measurement Strategies". en. In: *Radiation Protection Dosimetry* 93.4 (Feb. 2001). 00109, pp. 369–375. ISSN: 0144-8420. DOI: 10.1093/oxfordjournals.rpd.a006449.
- [80] Refrigerating and Air-Conditioning Engineers American Society of Heating Inc. "2017 ASHRAE® Handbook - Fundamentals (I-P Edition)". In: (). 00000. ISSN: 978-1-939200-57-0.
- [81] Emil Simiu. "Design of Buildings for Wind - A Guide for ASCE 7-10 Standard Users and Designers of Special Structures (2nd Edition)". In: (). 00000. ISSN: 978-0-470-46492-2.
- [82] Fred D Tillman and James W Weaver. "Review of Recent Research on Vapor Intrusion". en. In: (Sept. 2005). 00028, p. 47.
- [83] Xinké Wang, Yinpíng Zhang, and Jianyin Xiong. "Correlation between the Solid/Air Partition Coefficient and Liquid Molar Volume for VOCs in Building Materials". In: *Atmospheric Environment* 42.33 (Oct. 2008). 00013, pp. 7768–7774. ISSN: 1352-2310. DOI: 10.1016/j.atmosenv.2008.05.030.
- [84] Jing Xu et al. "Determination of Partition and Diffusion Coefficients of Formaldehyde in Selected Building Materials and Impact of Relative Humidity". In: *Journal of the Air & Waste Management Association* 62.6 (June 2012). 00017, pp. 671–679. ISSN: 1096-2247. DOI: 10.1080/10962247.2012.665812.
- [85] A. Bodalal, J. S. Zhang, and E. G. Plett. "A Method for Measuring Internal Diffusion and Equilibrium Partition Coefficients of Volatile Organic Compounds for Building Materials". In: *Building and Environment* 35.2 (Feb. 2000). 00136, pp. 101–110. ISSN: 0360-1323. DOI: 10.1016/S0360-1323(99)00005-0.
- [86] Christopher C. Lutes et al. "Comparing Vapor Intrusion Mitigation System Performance for VOCs and Radon". en. In: *Remediation Journal* 25.4 (Sept. 2015). 00002, pp. 7–26. ISSN: 1520-6831. DOI: 10/gd6dfn.

- [87] John C. Little, Joan M. Daisey, and William W. Nazaroff. “Transport of Subsurface Contaminants into Buildings”. In: *Environmental Science & Technology* 26.11 (Nov. 1992). 00118, pp. 2058–2066. ISSN: 0013-936X. DOI: 10/dfg5dc.
- [88] Rui Shen, Kelly G. Pennell, and Eric M. Suuberg. “A Numerical Investigation of Vapor Intrusion — The Dynamic Response of Contaminant Vapors to Rainfall Events”. In: *Science of The Total Environment* 437 (Oct. 2012). 00026, pp. 110–120. ISSN: 0048-9697. DOI: 10/f4fp9s.
- [89] Jonathan G. V. Ström et al. “Factors Affecting Temporal Variations in Vapor Intrusion-Induced Indoor Air Contaminant Concentrations”. In: *Building and Environment* 161 (Aug. 2019). 00000, p. 106196. ISSN: 0360-1323. DOI: 10.1016/j.buildenv.2019.106196.
- [90] Eric Jones, Travis Oliphant, and Pearu Peterson. *SciPy: Open Source Scientific Tools for Python*. 03367. 2011.
- [91] U.S. Environmental Protection Agency. *Users's Guide For Evaluating Subsurface Vapor Intrusion Into Buildings*. 00000. 2004.
- [92] Lilian D V Abreu and Henry Schuver. *Conceptual Model Scenarios for the Vapor Intrusion Pathway*. en. 00018. 2012.
- [93] Han-Cheng Dan et al. “Capillary Effect on Flow in the Drainage Layer of Highway Pavement”. In: *Canadian Journal of Civil Engineering* 39.6 (June 2012). 00008, pp. 654–666. ISSN: 0315-1468. DOI: 10/f3236b.

# Appendix A

## Geometry Generation

To create our quarter geometry, only a few simple geometric objects and Boolean operations are required: two cuboids, two rectangles, one Boolean difference operation, and one Boolean join operation. Figure 2.5 shows the resulting geometry. Note that  $z = 0\text{ m}$  is the groundwater/soil interface and the plane of symmetry is around the  $(x, y) = (0\text{ m}, 0\text{ m})$  axis

To create the soil surrounding the building using the COMSOL geometry generator:

1. Create a 15 m by 15 m by 4 m block with its base at  $(x, y, z) = (0\text{ m}, 0\text{ m}, 0\text{ m})$ . This is the entire soil domain.
2. Create a 5 m by 5 m by 1 m block with its base at  $(x, y, z) = (0\text{ m}, 0\text{ m}, 3\text{ m})$ . This will represent the volume that the house take up in the soil, i.e. the underground portion of the basement.
3. Perform a difference operation, removing the "basement" block from the "soil" block.

At this point you will see that a quarter soil domain has been created, with an empty space that represents a house with a foundation slab located 1 m bgs.

The foundation crack will be modeled by joining two 1 cm wide strip that spans the perimeter of the surface that represents the house foundation. This strip is created by joining two rectangles on foundation surface:

1. Define a work plane 3 m above zero. This allows us to place two-dimensional objects on the surface of or inside a three-dimensional object.
2. On the work plane create a 5 m by 1 cm rectangle with its base at  $(x, y) = (0 \text{ m}, 5 \text{ m} - 1 \text{ cm})$ . This represents one side of the perimeter crack.
3. Copy the rectangle and rotate it  $90^\circ$  around the corner of the foundation, i.e.  $(x, y) = (5 \text{ m} - 0.5 \text{ cm}, 5 \text{ m} - 0.5 \text{ cm})$ .
4. Join the two rectangles to create a unified perimeter foundation crack.

Now the geometry of this VI scenario is complete.

## **Appendix B**

### **Soil Properties**

Table B.1: Properties and van Genuchten parameters of select soil types[92].

Soil type	Permeability $\kappa$ (m <sup>2</sup> )	Density $\rho$ (kg/m <sup>3</sup> )	Porosity $\theta_t$	Residual moisture $\theta_r$	van Genuchten $\alpha$	van Genuchten parameters $m$
Sand	$9.9 \times 10^{-12}$	1430	0.38	$5.3 \times 10^{-2}$	3.5	3.2
Loamy sand	$1.6 \times 10^{-12}$	1430	0.39	$4.9 \times 10^{-2}$	3.5	1.7
Sandy loam	$5.9 \times 10^{-13}$	1460	0.39	$3.9 \times 10^{-2}$	2.7	1.4
Sandy clay loam	$2.0 \times 10^{-13}$	1430	0.38	$6.3 \times 10^{-2}$	2.1	1.3
Loam	$1.9 \times 10^{-13}$	1380	0.40	$6.1 \times 10^{-2}$	1.5	1.5
Silt loam	$2.8 \times 10^{-13}$	1380	0.44	$6.5 \times 10^{-2}$	0.51	1.7
Clay loam	$1.3 \times 10^{-13}$	1500	0.44	$7.9 \times 10^{-2}$	1.6	1.4
Silty clay loam	$1.7 \times 10^{-13}$	1390	0.48	$9.0 \times 10^{-2}$	0.84	1.5
Silty clay	$1.5 \times 10^{-13}$	1300	0.48	$1.1 \times 10^{-1}$	1.6	1.3
Silt	$6.7 \times 10^{-13}$	1260	0.49	$5.0 \times 10^{-2}$	0.66	1.7
Sandy clay	$1.7 \times 10^{-13}$	1470	0.39	$1.2 \times 10^{-1}$	3.3	1.2
Clay	$2.3 \times 10^{-13}$	1330	0.46	$9.8 \times 10^{-2}$	1.3	1.3
Gravel[93]	$1.3 \times 10^{-9}$	1430	0.42	$5.0 \times 10^{-3}$	100	2.19